Study on Development of Retrieval Procedure of Atmospheric HFC-23 with Ground-based Fourier Transform Infrared Spectrometers

博 士 学 位 論 文

Doctoral Dissertation

Study on Development of Retrieval Procedure

of Atmospheric HFC-23 with Ground-based

Fourier Transform Infrared Spectrometers

(地上設置型フーリエ変換赤外分光計を用いた大気中

HFC-23 のリトリーバル手法の開発に関する研究)

東北大学大学院環境科学研究科

Graduate School of Environmental Studies, Tohoku University

専攻 major／コース course	
環境科学専攻 / 地球システム・エネルギー学コース	

氏 名 Name	武田　真憲

指　導　教　員 Supervisor at Tohoku Univ.	中島　英彰　客員教授
研 究 指 導 教 員 Research Advisor at Tohoku Univ.	
審　査　委　員 （○印は主査） Dissertation Committee Members Name marked with "○" is the Chief Examiner	○　中島 英彰　客員教授 1　土屋 範芳　教授　　2　町田 敏暢　客員教授 3　村田 功　准教授　　4 5　　6

Doctoral Dissertation

Study on Development of Retrieval Procedure of Atmospheric HFC-23 with Ground-based Fourier Transform Infrared Spectrometers

Masanori Takeda

July 2021

Abstract

Trifluoromethane (CHF_3, HFC-23) is a powerful greenhouse gas whose emissions are contributing to climate change. HFC-23 is generated from the production of chlorodifluoromethane ($CHClF_2$, HCFC-22) as a by-product. This thesis aims to investigate the retrieval method of atmospheric amounts of HFC-23 and HCFC-22.

Firstly, a procedure for retrieving atmospheric abundances of HFC-23 (CHF_3) with a ground-based Fourier transform infrared spectrometer (FTIR) has been developed for the first time, and the first HFC-23 total column abundances were retrieved from solar mid-infrared spectroscopic measurements at Rikubetsu, Japan (43.5°N, 143.8°E), and at Syowa Station, Antarctica (69.0°S, 39.6°E). The FTIR retrievals were carried out with the SFIT4 retrieval program, and the two spectral windows of 1138.5–1148.0 cm^{-1} and 1154.0–1160.0 cm^{-1} in the overlapping ν_2 and ν_5 vibrational-rotational transition bands of HFC-23 were used to avoid strong H_2O absorption features. Vertical profiles of H_2O, HDO, and CH_4 are preliminarily retrieved with other independent spectral windows because these profiles may induce large uncertainties in the HFC-23 retrieval. Each HFC-23 retrieval has only one piece of vertical information with sensitivity to HFC-23 in the troposphere and the lower stratosphere. Retrieval errors mainly arise from the systematic uncertainties of the spectroscopic parameters used to obtain the HFC-23, H_2O, HDO, and CH_4 abundances.

Secondly, atmospheric abundances of HCFC-22 were retrieved from the solar mid-infrared spectra measured at Rikubetsu and Syowa Station, with SFIT4 program and the

spectral interval of 828.75–829.40 cm^{-1} which was used in previous study at Jungfraujoch, Switzerland. The HCFC-22 retrieval provided only one piece of vertical information having a sensitivity to the troposphere and the lower stratosphere. Errors in HCFC-22 retrieval mainly came from measurement noise and the systematic uncertainty of the HCFC-22 spectroscopic parameter.

Then, the column-averaged dry-air mole fraction data were derived from the FTIR-retrieved HFC-23 and HCFC-22 total columns at Rikubetsu and Syowa Station, and these data were used for comparison with surface dry-air mole fractions provided by AGAGE (Advanced Global Atmospheric Gases Experiment). The FTIR-retrieved HFC-23 dry-air column-averaged mole fractions ($X_{\mathrm{HFC-23}}$) at Rikubetsu and Syowa Station have negative biases coming from the spectroscopic parameters compared to AGAGE datasets. Also, the time-series of the FTIR-retrieved $X_{\mathrm{HFC-23}}$ at Rikubetsu has a seasonal pattern with a maximum peak in summer, which is probably caused by atmospheric transport of the regional pollutant from Asia. The annual change rates of the FTIR-retrieved $X_{\mathrm{HFC-23}}$ at Rikubetsu and Syowa Station, which were calculated except for the data affected by the regional pollution, are basically in good agreement with those derived from the AGAGE datasets. On the other hand, the HCFC-22 dry-air column-averaged mole fractions ($X_{\mathrm{HCFC-22}}$) at Rikubetsu and Syowa Station have no significant bias. The FTIR-retrieved $X_{\mathrm{HCFC-22}}$ at Rikubetsu shows a seasonal cycle as the same of the FTIR-retrieved HFC-23. The annual change rates of the FTIR-retrieved $X_{\mathrm{HCFC-22}}$ at both FTIR observation sites, which were derived from the observations except for the data

influenced by the regional pollution, are consistent with AGAGE datasets.

Lastly, backward trajectory analysis was carried out to examine the origins and transport pathways of air masses arriving at Rikubetsu. The enhancement ratios of HFC-23 and HCFC-22 for each year were calculated from the FTIR measurement data for the air masses passed through China, and the attempt was made to estimate Chinese annual HFC-23 emissions. In this study, the HFC-23 emission from China in 2000 was only calculated, and then the annual emission rate was estimated at 1.18 ± 0.39 Gg year^{-1}. Combined the FTIR observations of HFC-23 with those of HCFC-22, it is possible to estimate the origination of the FTIR-retrieved HFC-23.

This thesis demonstrates that ground-based FTIR measurements are capable of monitoring the long-term trends of HFC-23 and HCFC-22. Furthermore, it is shown that there is a possibility we can estimate regional emission of HFC-23 combining the ground-based FTIR measurement data of HFC-23 and HCFC-22. If the FTIR measurement techniques of atmospheric HFC-23 developed in this study was extended to other NDACC ground-based FTIR sites around world, the measurements reported from these sites would complement the global AGAGE observations by filling spatial and temporal gaps and may lead to improved insights about changes in regional and global emissions of HFC-23 and its role in global warming.

Acknowledgement

Here, I am about to write my appreciation for all of the people who supported my research activity for a long time since I enrolled in Tohoku University in 2013. I have acquired not only many academic experiences but also non-academic by help from these people, in the long way to complete my doctoral study.

I would like to begin by expressing my deepest gratitude to my supervisor, Professor Hideaki Nakajima, for giving me the motivation of this study and his great support throughout my doctoral course. I have greatly benefited from his precise advices, deep experimental knowledge, and continuous encouragement. And I blessed with a chance to go to Antarctica. I could get involved with twice scientific expedition in Antarctica as a summer member of the 56th Japanese Antarctic Research Expedition (JARE-56) and a wintering member of JARE-57. If it were not for his recommendation and support, I could not engage in these activities which are definitely the most wonderful experiences in my life.

I would like to express my sincere gratitude to my advisor, Associate Professor Isao Murata, for his constructive suggestions. I have learned many knowledges from the fundamental knowledge of FTIR observation to the maintenance procedure of FTIR instrument. And I was able to have a benefit discussion regarding this study with him. Also, I am sincerely grateful to Professor Noriyoshi Tsuchiya and Professor Toshinobu Machida for their helpful advices.

I would like to express my appreciate to Dr. Tomoo Nagahama in Nagoya University and Dr. Isamu Morino in the National Institute for Environmental Studies (NIES) for helping me with their advices regarding the FTIR instruments at Rikubetsu, Japan. Also, I could have many useful discussion together with them in several scientific meetings. I want to express my special gratitude to Dr. Geoffrey Toon in NASA Jet Propulsion Laboratory for providing the spectroscopic parameter data of HFC-23. None of this study would be possible without him.

I have received great support from many people for advancing this study. I would like to express my sincerely thanks to all the members of JARE-48, JARE-52, JARE-56, and JARE-57, and all other people in the National Institute for Polar Research for supporting for the FTIR observations at Syowa Station. I would like to thank Dr. Kosuke Saeki and Dr. Takeshi Kinase for performing the FTIR observations at Syowa Station in 2007 and 2011, respectively. Moreover, this work was carried out by the joint research program of the Institute for Space-Earth Environmental Research, Nagoya University. FTIR operations of the Rikubetsu site are financially supported in part by the GOSAT series project. I acknowledge Dr. Makoto Koike, Mr. Kazuo Hanano, and Mr. Nobuyuki Yokozeki for the operation of the FTIR observations at Rikubetsu. I would like to thank Dr. Tomoko Shirai, Dr. Masaatsu Miyauchi, Dr. Yoshihiro Nagahama, and Ms. Kumiko Shiba for providing a friendly work environment in the lab in NIES since 2012 when I was a graduate student in the University of Tsukuba.

Finally, I express my deepest gratitude to my parents (Etsuo and Atsuko), brother

(Naoki), and all other family members for supporting my life. I also want to express my sincere gratitude to my late maternal grandmother (Mitsuko) for her affection since I was a child.

Masanori Takeda

Contents

List of Tables

List of Figures

Chapter 1

Introduction

1.1 Earth's atmosphere

Earth's atmosphere is mainly composed by nitrogen (N_2) of 78%, oxygen (O_2) of 20.95%, and argon (Ar) of 0.93%, by volume. Although water vapor (H_2O) is accounted as the fourth composition with a contribution of 0.25% to total air by mass, its temporal and spatial variability is very large (0–5% by volume) (Wallace and Hobbs, 2006). Therefore, the earth's atmosphere is generally represented as dry-air which removed water vapor, and ratios of many atmospheric compositions are habitually listed related to the dry-air (Table 1.1). The remaining percentage of the dry air includes hundreds of chemical species, which are generally called "trace gases," despite of its very few percentage to the total air. The trace gases are closely related to global atmospheric environmental issues like the stratospheric ozone depletion and the global warming. For example, H_2O,

CO_2, O_3, CH_4, and N_2O are greenhouse gases (GHGs) which affect the global warming because these molecules have radiative absorption features in infrared (IR) region of light (electro-magnetic radiation).

The Earth's atmosphere is composed of some layers as shown in Figure 1.1. Most of the atmospheric phenomenon as known as "weather" occur in the troposphere which is covering the altitudinal range from ground to about 15 km. In the troposphere, the temperature is decreasing with increasing altitude in accordance with the mean temperature lapse rate ($\Gamma = -6.5$ °C/km), because the Earth's surface is heated by radiation from the sun. Therefore, the tropospheric air accounted for approximately 80% of the mass of the Earth's atmosphere is well-mixed due to convection between cold air in the upper and warm air in the lower. The atmospheric layer between approximately 15 km and 50 km is called as the stratosphere. In contrast with the troposphere, the temperature in the stratosphere is increasing with rising altitude and the stratosphere is strongly stratified. Therefore, convection is strongly inhibited in the stratosphere and cloud does not appear except for the polar stratosphere. The temperature structure in the stratosphere is caused by the ozone-rich region (ozone layer) because O_3 molecules in the ozone layer absorb a part of ultraviolet (UV) radiation from the sun and heat ambient air. The cause of the ozone layer is described in section 1.3.1.

The development, diversification, and continuation of the atmospheric observations have largely contributed to the discovery of important signals of global environmental change. Since the Industrial Revolution, changes in global air quality have become more

dramatic than before due to the expansion of human production activities. The global atmospheric environmental problems what we have faced until today are mainly (1) rising Earth's surface temperature (global warming) and (2) destruction of the stratospheric ozone layer (stratospheric ozone depletion), except for the problems of acidic rain and regional air pollution coming from harmful gases and aerosols. The following sections will be summarized about historical background of these global environmental problems.

Table 1.1: Fractional concentrations by volume of the atmospheric constituents up to an altitude of 105 km, against dry air. Adapted from Wallace and Hobbs (2006).

Constituents	Molecular weight	Fractional concentration by volume
Nitrogen (N_2)	28.01	78.08%
Oxygen (O_2)	32.00	20.95%
Argon (Ar)	39.95	0.93%
Water vapor (H_2O)	18.02	0–5%
Carbon dioxide (CO_2)	44.01	412 ppm[a]
Neon (Ne)	20.18	18 ppm
Helium (He)	4.00	5 ppm
Methane (CH_4)	16.04	1.88 ppm[b]
Krypton (Kr)	83.80	1 ppm
Hydrogen (H_2)	2.02	0.5 ppm
Nitrous oxide (N_2O)	56.03	0.33 ppm[c]
Ozone (O_3)	48.00	0–0.1 ppm

[a] Global mean value in 2020. Reference: `https://www.esrl.noaa.gov/gmd/ccgg/trends/global.html`, last access at November 5, 2020.

[b] Global mean value in 2020. Reference: `https://www.esrl.noaa.gov/gmd/ccgg/trends_ch4/`, last access at November 5, 2020.

[c] Global mean value in 2020. Reference: `https://www.esrl.noaa.gov/gmd/ccgg/trends_n2o/`, last access at November 5, 2020.

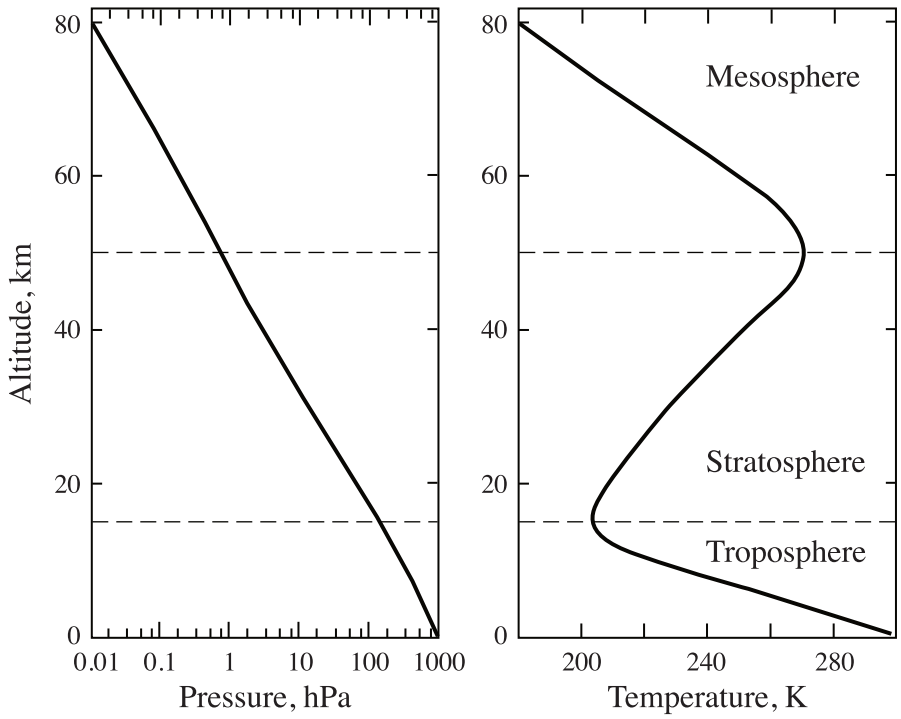

Figure 1.1: Mean pressure and temperature vs. altitude at 30°N, March. Reproduced from Jacob (1999).

1.2 Global warming

The scientific discussion between Earth's climate and GHGs has been continued for more than a century. This history was summarized in Fleming (1998), Weart (2008), and Le Treut et al. (2007). Horace Benedict de Saussure (1740–1799), a Swiss geologist, meteorologist, physicist, and mountaineer, demonstrated for the first time by simple greenhouse experiments in the 1760s that Earth's air itself could capture thermal radiation. In the 1820s, Joseph Fourier (1768–1830) (Figure 1.2), a French physicist and

Figure 1.2: Joseph Fourier (1768–1830). Reproduced from Wikipedia (`https://en.wikipedia.org/wiki/Joseph_Fourier`, last access: 8 January 2021).

mathematician, mathematically derived the temperature of the Earth's surface warmed by only incoming solar radiation, and found that its temperature should be lower than actual one. In 1824, Fourier presented a hypothesis that, in addition to solar radiation, actual Earth's atmospheric temperature is generated by intervention of atmosphere which traps thermal radiation from the Earth's surface, in reference to the Saussure's experiments. His concept of the possibility that the atmosphere might behave as a resistance of some kind is widely known as the first proposal of the greenhouse effect.

John Tyndall (1820–1893), an Irish physicist, began laboratory experiments in term of absorption properties for thermal radiation with various molecules in 1859. The first ratio spectrophotometer was constructed in his experimentation, and he accurately mea-

sured the relative absorptive powers of nitrogen, oxygen, hydrogen, water vapor, carbon dioxide, and other trace gases. In the paper of Tyndall (1861), he indicated that H_2O and CO_2 significantly absorb IR radiation from the Earth's surface, and said that "The chief influence be exercised by the aqueous vapour, every variation of this constituent must produce a change of climate. Similar remarks would apply to the carbonic acid diffused through the air." Tyndall's report is the first discovery of GHGs, and he also mentioned the possibility of their influence to climate change.

Svante Arrhenius (1859–1927), a Swedish physicist and chemist, respected the considerations of pioneers (i.e. Fourier, Tyndall), and calculated how the change in CO_2 concentration in Earth's atmosphere would affect the surface temperature as the first climate sensitivity experiment. Arrhenius reported that the doubling in the atmospheric CO_2 concentration would increase by 5–6 °C in the surface temperature. In addition, he predicted that CO_2 emission caused by human activity would be large enough to induce global warming, but it would take thousands of years to double the atmospheric CO_2 concentration considering to the CO_2 emission rate at that time. Therefore, nobody was interested in his study at that time because people believed that human activity does not mostly affect Earth's climate in a short time range.

Guy Stewart Callendar (1898–1964), an English steam engineer and inventor, linked global warming to greenhouse gases by analysis of many observational records. By screening only good quality data from the land-based temperature records at large number of station around the world, without use of a computer, he showed the increased tempera-

ture from the end of the 19th century to the early 20th century, and linked the increased temperature to a rise of atmospheric CO_2 concentration due to combustion of fossil fuel. However, Callendar's proposal was not accepted seriously due to unreliability in CO_2 measurements at that time (Weart, 2008).

High accuracy and continuously observation of GHGs began in the latter half of the 20th century. In 1958, the high-precision long-term measurements of the atmospheric CO_2 concentration were started at Mauna Loa, Hawaii, United State of America (USA) by Charles David Keeling (1928–2005) of the Scripps Institution of Oceanography (Keeling, 1960). Keeling et al. (1976) reported the long-term variation in CO_2 concentration at Mauna Loa, and indicated the first quantitative discussion on the impact of CO_2 emission caused by human activity such as fossil fuel combustion. After the Keeling's pioneering work, accurate ground-based observations of CO_2 were rapidly expanded around the world, with a common concentration calibration scale.

Until the 1950s, only CO_2 and H_2O were concerned as the significant GHGs. Since the 1970s, other GHGs (e.g. CH_4, N_2O, Halocarbons) have been widely recognized (Ramanathan, 1975; Wang et al., 1976).

In 1988, the World Meteorological Organization (WMO) established the Intergovernmental Panel on Climate Change (IPCC) with the support of the United Nations Environment Programme (UNEP). The IPCC continues its work through the present day, and issues a series of Assessment Reports and supplemental reports that describe the state of scientific understandings at the time each report is prepared. Scientific developments

during this period are summarized about once every five to six years in the IPCC Assessment Reports which were published in 1990 (First Assessment Report), 1995 (Second Assessment Report), 2001 (Third Assessment Report), 2007 (Fourth Assessment Report), and 2013/2014 (Fifth Assessment Report). Since the 1990s, research on climate change has expanded and grown, linking many fields such as atmospheric sciences, numerical modeling, social sciences, geology and economics, or security.

The United Nations Framework Convention on Climate Change (UNFCCC) is an international environmental treaty to seek for the stabilization of greenhouse gas concentrations in the atmosphere for a purpose that would prevent dangerous anthropogenic human-induced interference with the earth's climate system. The UNFCCC was drafted in May 1992 and was established on 21 March 1994. Its highest decision-making body, the Conference of the Parties (COP), holds annually to assess progress in the efforts for climate change. Based on the scientific consensus that global warming is occurring and it is extremely probable that human-made GHGs emissions have predominantly caused it, the Kyoto Protocol was adopted in the 3rd Conference of the Parties (COP-3) in Kyoto, Japan, on 11 December 1997, as an international framework until 2020 which extends the 1992 UNFCCC. One of the tasks set by the UNFCCC was for signatory nations to establish national greenhouse gas inventories of GHG emissions and reductions. Under the Kyoto Protocol, developed countries must submit annually updated inventories. On the other hand, developing countries are not obliged to reduce GHG emissions. The Kyoto Protocol applies to the six greenhouse gases listed: carbon dioxide (CO_2), Methane

(CH_4), nitrous oxide (N_2O), hydrofluorocarbons (HFCs), perfluorocarbons (PFCs), and sulfur hexafluoride (SF_6). The Kyoto Protocol came into effect on 16 February 2005. There are currently 191 participating countries (Canada withdrew from the protocol in December 2012) and the European Union (EU) to the Protocol. The Kyoto Protocol also includes what came to be known as Kyoto mechanisms such as emissions trading, joint implementation, and clean development mechanism (CDM). The CDM, defined in Article 12 of the Protocol, was intended to meet two objectives: (1) to assist developing countries in achieving sustainable development and in contributing to the ultimate objective of the UNFCCC which is to prevent dangerous climate change; and (2) to assist developed countries in achieving compliance with their quantified emission limitation and reduction commitments (GHG emission caps).

As measures to be taken after the end of the Kyoto Protocol in 2020, the Paris Agreement was adopted in COP-21 in Le Bourget, near Paris, France, in 12 December 2015, and entered into force on 4 November 2016. The agreement is an independent treaty under the UNFCCC rather than an amendment of the Kyoto Protocol. The Paris Agreement's aim is to keep the increasing of global mean surface temperature to "well below" a increase of 2 °C, hopefully 1.5 °C compared to pre-industrial levels. All 197 members (include the EU) of the UNFCCC have signed the Paris Agreement and 189 remain party to it as of 2020. Of the eight countries which are not party to the agreement, the only significant emitters are Iran and the United States. Under the Paris Agreement, each participating country must determine and regularly report on the contribution that undertakes to pre-

vent irremediable global warming. There is no force that a country should set a specific emissions target by a specific date, but each target should go beyond previous targets.

1.3 Stratospheric ozone destruction

1.3.1 Ozone layer

O_3 molecules in the ozone layer absorb a part of UV radiation from the sun. Solar UV radiation is divided into three types of UV-A, UV-B, and UV-C (see Figure 1.3). Solar UV-C radiation (wavelength range from 100 to 280 nm), high energy radiation, is extremely harmful to us and other life forms. Solar UV-C radiation is perfectly absorbed in the ozone layer and by atmospheric oxygen. Solar UV-B radiation (wavelength range from 280 to 315 nm) is partially absorbed in the ozone layer and then humans and other life forms are exposed to some UV-B radiation. Excessive exposure to UV-B radiation raises the risks of skin cancer, cataracts, and a suppressed immune system for humans. Solar UV-A radiation (wavelength range from 315 to 400 nm), which causes premature aging of the skin for humans, is not absorbed mostly by the ozone layer. Stratospheric ozone is considered "good ozone" since it protects the terrestrial biosphere from the harmful solar UV radiation (shorter wavelength than 315 nm). In contrast, O_3 in the troposphere is considered "bad ozone" because it affects the atmosphere as a greenhouse gas and plays a significant role in the production of smog and related pollutants. Also, O_3 molecules cause damage to a human body directly.

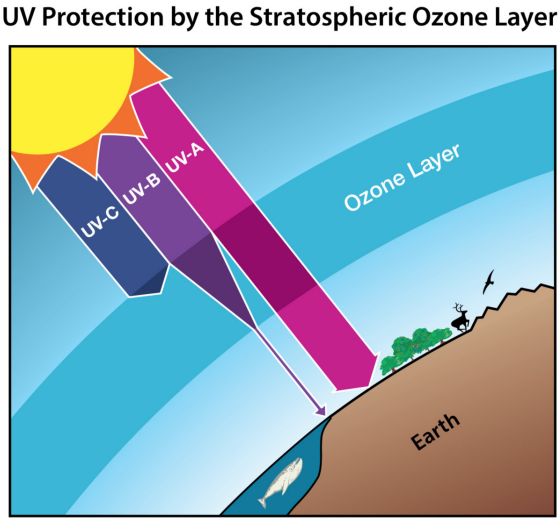

Figure 1.3: Protection from ultraviolet radiation by the ozone layer. Reproduced from Salawitch et al. (2019).

Ozone is naturally generated and destroyed in the stratosphere by the Chapman mechanism (Chapman, 1930):

$$\mathrm{O_2} + h\nu \rightarrow \mathrm{O} + \mathrm{O} \tag{1.1}$$

$$\mathrm{O} + \mathrm{O_2} + \mathrm{M} \rightarrow \mathrm{O_3} + \mathrm{M} \tag{1.2}$$

$$\mathrm{O_3} + h\nu \rightarrow \mathrm{O_2} + \mathrm{O}(^1\mathrm{D}) \tag{1.3}$$

$$\mathrm{O_3} + \mathrm{O} \rightarrow 2\mathrm{O_2} \tag{1.4}$$

$$\mathrm{Net} : 3\mathrm{O_2} \rightarrow 2\mathrm{O_3} \tag{1.5}$$

where $h\nu$ represents a photon of ultraviolet light, and M represents a generic both gas

molecule. According to this mechanism, O_3 should naturally have a chemical equilibrium concentration that is approximately a factor of two greater than the observed value (Jacob, 1999). A more complete description requires stratospheric dynamics which redistributes O_3 from the tropics, where it is formed, to the mid-latitude and polar regions (Dobson, 1956). The chemical destruction of stratospheric ozone through chemical loss cycles is also an important process.

The chemical destruction of stratospheric ozone is caused by the following catalytic reaction cycle:

$$\mathrm{X} + \mathrm{O_3} \rightarrow \mathrm{XO} + \mathrm{O_2} \tag{1.6}$$

$$\mathrm{XO} + \mathrm{O} \rightarrow \mathrm{X} + \mathrm{O_2} \tag{1.7}$$

$$\mathrm{Net} : \mathrm{O_3} + \mathrm{O} \rightarrow 2\mathrm{O_2} \tag{1.8}$$

where X is a catalytic molecule (atom) which does not transform before and after the cycle. For example, hydrogen oxides HO_x (i.e. H, OH, HO_2) (Hant, 1966), nitrogen oxides NO_x (e.g. NO, NO_2) (Crutzen, 1970; 1971) act catalysis for the cycle.

1.3.2 Ozone depletion and the Montreal Protocol

Most important stratospheric O_3 loss mechanism is the catalytic cycle driven by halogen (e.g. Cl, Br). Molina and Rowland (1974) indicated that increases of the production and consumption of chlorofluorocarbons (CFCs) contribute the stratospheric ozone loss,

for the first time. CFCs were developed for industrial uses in USA in the 1930s, and had been widely used to many applications (e.g. refrigerants of air condition and refrigerator, blowing agents, aerosol spray propellants, solvents). Molina and Rowland (1974) explained that $CFCl_3$ (CFC-11) and CF_2Cl_2 (CFC-12), major atmospheric CFCs, are easily transported into the stratosphere due to chemical inertness in the troposphere and high volatility, and then are decomposed by the following photolytic reactions at altitude of 20–40 km:

$$CFCl_3 + h\nu \rightarrow CFCl_2 + Cl \tag{1.9}$$

$$CF_2Cl_2 + h\nu \rightarrow CF_2Cl + Cl. \tag{1.10}$$

The photodissociation in the stratosphere generates significant amounts of chlorine atoms, and lead to the destruction of stratospheric ozone through the catalytic cycle. There are also other cycles that incorporate more than one halogenated compound (such as BrO and ClO). In addition to halogenated catalytic loss through gas-phase chemical reaction, heterogeneous reaction can also occur in the presence of aerosols. Heterogeneous reaction is particularly efficient in the polar regions when stratospheric temperatures become low enough to form polar stratospheric clouds (PSCs) (Solomon et al., 1986; Solomon, 1999). Consequently, the heterogeneous reactions on surfaces of PSCs play an important role in explaining the observed depletion of ozone over Antarctica (Molina et al., 1987).

Chubachi (1984), in the presentation in the Quadrennial Ozone Symposium in Greece,

reported a decline of total ozone observed in austral spring (September to October) in 1982 at Syowa Station, Antarctica. Chubachi's presentation is actually the first report of polar ozone depletion, well-known as the ozone hole. Farman et al. (1985) reported that total ozone above the Antarctica in the austral spring had been decreasing since the late 1970s at least, based on the observations at Halley Bay, Antarctica. Moreover, their report indicated the relationship between the observed decrease in total ozone and increases in organochlorinated compounds (i.e. CFC-11 and CFC-12) for the first time. The ozone observation data taken from Nimbus 7 satellite since 1978 showed us an appearance of ozone depletion spreading over the Antarctica like a "hole" for each year (Stolarski et al., 1986).

Various scientific knowledges relevant to the ozone depletion accumulated since the 1970s gave us an incentive to decide frameworks to prevent destruction of the ozone layer through international organizations such as the World Meteorological Organization (WMO) and the United Nations. The Vienna Convention for the Protection of the Ozone Layer is a multilateral environmental agreement signed on 22 March 1985 that provided frameworks for international reductions in the production of organic halogenated compounds (halocarbons) like CFCs affecting the ozone layer and entered into force on 22 September 1988. While not a binding agreement, it acts as a framework for the international efforts to protect the ozone layer. In accordance with the 1985 Vienna Convention, the Montreal Protocol on Substances that Deplete the Ozone Layer, well-known simply as the Montreal Protocol (UNEP, 2000), is an international rule designed to protect the ozone

layer by phasing out the production of numerous substances that are responsible for ozone depletion (ozone-depleting substances; ODSs). The Montreal Protocol was adopted on 26 August 1987 and entered into force on 26 August 1989. The treaty was amended to ban CFC production after 1995 in the developed countries, and later in developing countries. Compounds containing carbon–hydrogen (C–H) bonds (such as hydrochlorofluorocarbons; HCFCs) have been designed to replace CFCs in certain applications. These replacement compounds are more reactive and most of the compounds are decomposed, before reaching the stratosphere where they could affect the ozone layer. While being less damaging than CFCs, HCFCs can have a negative impact on the ozone layer, so they are also being phased out. This production phaseout was possible because of efforts to ensure that there would be substitute chemicals and technologies for all ODSs uses. These gases are being gradually replaced by hydrofluorocarbons (HFCs) and other compounds that do not destroy stratospheric ozone at all.

As a result of the international agreement, Solomon et al. (2016) indicated that "healing" of the Antarctic ozone layer has now begun to occur in austral spring, based on satellite and ground-based observations, balloon-borne measurements, and model calculations. However, some breakdown can be expected to continue because of ODSs used by nations which have not banned them, and caused by gases which are already in the atmosphere because some ODSs, including CFCs, have very long atmospheric lifetimes. The world's leading chemistry-climate models (CCMs) indicate that the multi-model mean time series of the springtime Antarctic total column ozone will return to 1980 levels shortly after the

midcentury (about 2060) (Langematz et al.,2019).

The Vienna Convention and the Montreal Protocol have each been ratified by 196 countries and the EU, making them the first treaties ratified by all members in United Nations history. Kofi A. Annan, the seventh Secretary-General of the United Nations, described the Montreal Protocol as "perhaps the single most successful international agreement to date," due to its widespread adoption and implementation.

1.4 International initiatives toward HFC reduction

Hydrofluorocarbons have been used in refrigeration, air conditioning, thermal insulating foam, and miscellaneous applications since the 1990s, replacing the CFCs and HCFCs that were traditionally used in these applications. With the global CFC phase-out in 2010 and the ongoing HCFC phase-out, the use of HFCs has increased substantially, not only for various refrigeration and air conditioning applications, but also as foam blowing agents, as medical aerosols, and to a lesser extent as cleaning, etching, and fire-extinguishing agents. As was true for ODSs, emissions of HFCs follow production and consumption with a delay of months to decades, depending on the type of application in which the HFCs are used. HFCs do not contain ozone-depleting chlorine or bromine, but are potent greenhouse gases (Harris et al., 2014). Since 1997, HFCs have been included in the Kyoto Protocol to the UNFCCC as one group among many greenhouse gases. HFC emissions were not directly controlled by the Kyoto Protocol because the controls applied to the sum of all greenhouse

gases. To ensure that radiative forcing from the substitute HFCs does not offset climate gains provided by the Montreal Protocol phase-out of CFCs and HCFCs, Parties to the Montreal Protocol agreed to an Amendment to include some HFCs as controlled substances in Kigali, Rwanda in October 2016 (Kigali Amendment) and came into effect on January 1, 2019. Their production and consumption (GWP-weighted) are phased down in coming decades as shown in Figure 1.4 (UNEP, 2018). Limiting climate change is not the primary goal of the 1985 Vienna Convention for the Protection of the Ozone layer, but climate change considerations are addressed in this Convention. Limiting climate change was also a contributing factor to the 2007 Adjustment of the Montreal Protocol for an accelerated HCFC phase-out (UNEP, 2007). HFCs controlled by the Kigali Amendment include: HFC-23, HFC-32, HFC-41, HFC-125, HFC-134, HFC-134a, HFC-143, HFC-143a, HFC-152, HFC-152a, HFC-227ea, HFC-236cb, HFC-236ea, HFC-236fa, HFC-245ca, HFC-245fa, HFC-365mfc, and HFC-43-10mee (Table 1.2). This Amendment also specifies that emissions of HFC-23 generated during production of HCFCs or HFCs be destroyed to the extent practicable beginning January 2020.

Determining whether atmospheric concentrations of HFCs are changing as expected or not is promoted by the reporting by developed countries to the UNFCCC of national emissions because developing countries are not obligated to report their HFC emissions to the UNFCCC. For HFC-23, emission estimates for developing countries derived from information collected by the Montreal Protocol's Multilateral Fund are also considered. Emission magnitudes from countries not required to report emissions to the UNFCCC are

estimated by inverse analyses based on atmospheric measurements.

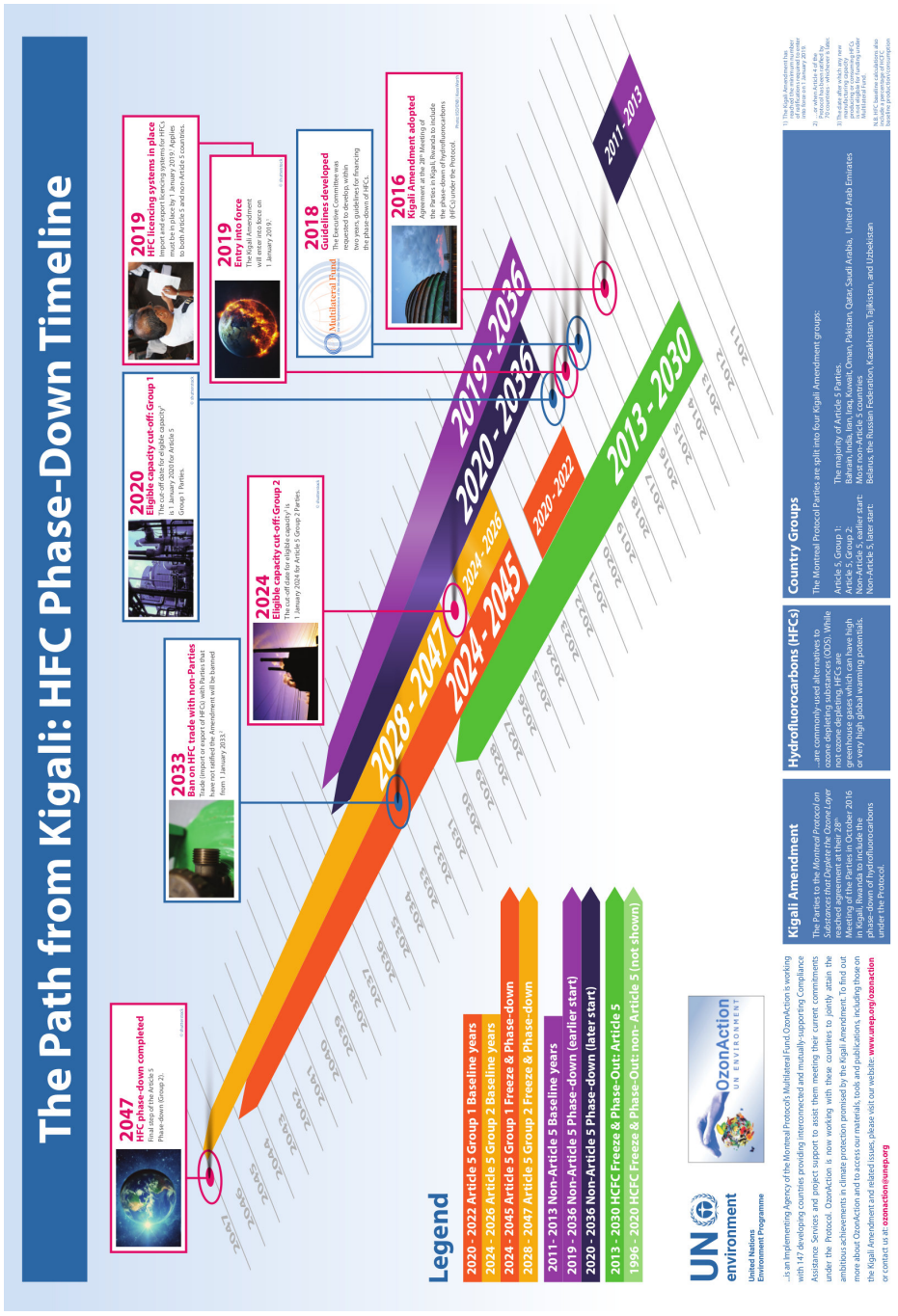

Figure 1.4: Base level and phase-down schedule for production and consumption of controlled HFCs under the Kigali Amendment to the Montreal Protocol (UNEP, 2018).

Table 1.2: Lifetimes and global warming potentials of HFCs listed as controlled substances in the Kigali Amendment to the Montreal Protocol. Adapted from Montzka et al. (2018).

Industrial designation of chemical name	**Chemical formula**	**Total lifetime [years, unless otherwise indicated]**	**100-year GWP**
HFC-23	CHF_3	228	12,690
HFC-32	CH_2F_2	5.4	705
HFC-41	CH_3F	2.8	116
HFC-125	CHF_2CF_3	30	3,450
HFC-134	CHF_2CHF_2	10	1,135
HFC-134a	CH_2FCF_3	14	1,360
HFC-143	CH_2FCHF_2	3.6	340
HFC-143a	CH_3CF_3	51	5,080
HFC-152	CH_2FCH_2F	172 days	17
HFC-152a	CH_3CHF_2	1.6	148
HFC-227ea	CF_3CHFCF_3	36	3,140
HFC-236cb	$CH_2FCF_2CF_3$	13.4	1,235
HFC-236ea	CHF_2CHFCF_3	11.4	1,370
HFC-236fa	$CF_3CH_2CF_3$	213	7,680
HFC-245ca	$CH_2FCF_2CHF_2$	6.6	720
HFC-245fa	$CHF_2CH_2CF_3$	7.9	880
HFC-365mfc	$CH_3CF_2CH_2CF_3$	8.9	810
HFC-43-10mee	$CF_3CHFCHFCF_2CF_3$	17.0	1,470

1.5 HFC-23

Trifluoromethane (CHF_3), also known as hydrofluorocarbon-23 (HFC-23), has an atmospheric lifetime of 228 years and a global warming potential integrated over a 100-year time scale (100-year GWP) of 12,690 (Montzka et al., 2018). Due to this high GWP, emissions of HFC-23 are contributing to climate change. HFC-23 is an unwanted by-product of

the production of chlorodifluoromethane ($CHClF_2$), hydrochlorofluorocarbon-22 (HCFC-22), with the HFC-23/HCFC-22 production ratio estimated to be up to 4% (McCulloch and Lindley, 2007). The Montreal Protocol is phasing out the production and consumption of HCFCs for emissive uses by 2020 in developed countries, and by 2030 in developing countries, while use for feedstock (e.g. in production of HFCs and fluoropolymers) is not restricted. Hence, emissions of HCFCs to the earth's atmosphere are expected to continue for quite a while. HCFC-22, one of the major HCFCs with an ozone depletion potential (ODP) of $\sim$ 0.03 and a 100-year GWP of 1,760 (Harris et al., 2014), has been widely used in air conditioners, refrigerators, foaming agents, or heat insulating materials, and therefore large banks still exist, which also contribute to ongoing emissions. Emission of HCFC-22 has increased since 2004 (Montzka et al., 2009), and global emissions in 2010 are estimated to have reached 386 ± 41 Gg year^{-1} by an inversion model (Simmonds et al., 2018a). Clearly, HFC-23 emissions have been increasing as a subsequence.

Currently, HFCs are widely used as substitutes of CFCs and HCFCs, because they have essentially no ODP and are therefore not contributing to ozone depletion. However, HFC-23 is not used as a substitute for CFCs or HCFCs, but is used in halon-1301 ($CBrF_3$) production, semiconductor manufacturing, very low temperature refrigeration, and specialty fire extinguisher (Oram et al., 1998; Miller et al., 2010, Simmonds et al., 2018a), which means that emissions from deliberate use of HFC-23 are small. Hence, HFC-23 has mainly been vented from HCFC-22 production plants into the atmosphere (Montzka et al., 2018). Simmonds et al. (2018a) reported that global annual emissions of HFC-23

were estimated to have reached 13.3 ± 0.8 Gg year^{-1} in 2006 up from 4.2 ± 0.7 Gg year^{-1} in 1980 due to rising the production of HCFC-22. After 2006, HFC-23 emissions rapidly decreased to 9.6 ± 0.6 Gg year^{-1} in 2009 as a result of thermal destruction of HFC-23 incentivized by the CDM under the Kyoto Protocol to the UNFCCC. Due to a scheduled end of the CDM project, however, HFC-23 emission again increased, rapidly reaching 14.5 ± 0.6 Gg year^{-1} in 2014 (Simmonds et al., 2018a). The annual global average mole fraction of HFC-23 reached 28.9 ppt (parts per trillion) in 2016, which corresponds to a radiative forcing of 5.2 mW m^{-2} (Montzka et al., 2018). This is the second largest radiative forcing among all HFCs and fluorinated-gases just after HFC-134a (14.3 mW m^{-2}) as shown in Figure 1.5. Miller and Kuijpers (2011) suggested that if no additional abatement measures are implemented to reduce HFC-23, its emission will rise to 24 Gg year^{-1} in 2035, and the mole fraction will rise to 50 ppt which corresponds to a radiative forcing of 9 mW m^{-2}. Furthermore, if the emissions of HFC-23 are not regulated and all UNFCCC CDM project were terminated, the HFC-23 emission growth rate after 2030 would rise to 0.8 Gg year^{-2}, which is four times larger than the previous trend (see Figure 1.6). The 2016 Kigali Amendment to the Montreal Protocol includes to control production of HFC-23. Unfortunately, Stanley et al. (2020) reported that the global HFC-23 emissions, derived from atmospheric measurements (top-down estimate), reached 15.9 ± 0.9 Gg year^{-1} in 2018 which was higher than in any year in history. Moreover, their results indicated that the top-down global emission in 2017 was 12.5 ± 0.7 Gg year^{-1} higher than the inventory-based emission of 2.4 Gg year^{-1} (bottom-up estimate), despite

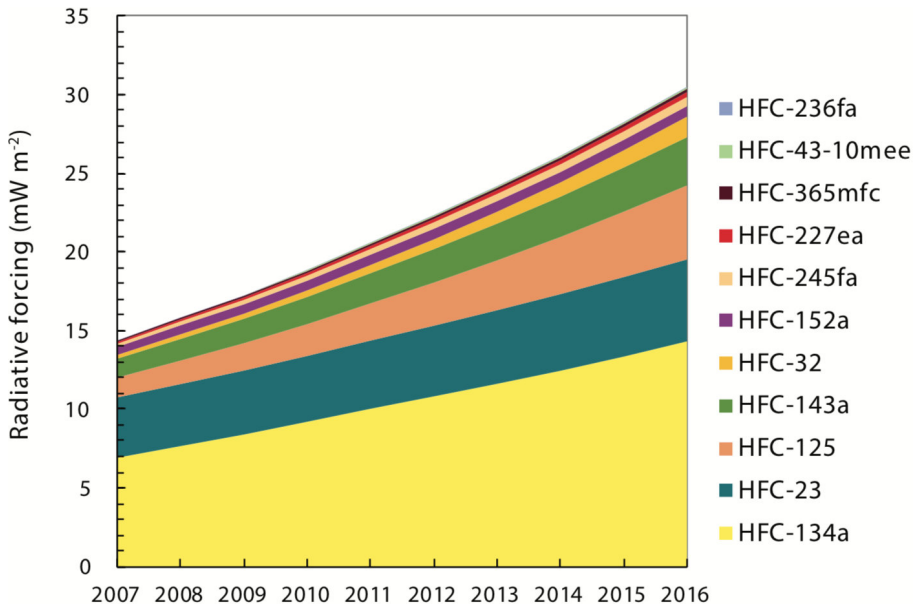

Figure 1.5: Radiative forcing supplied by individual HFCs and their sum during the past decade based on observed global mole fractions and their change over time. These forcings are derived by multiplying measured mole fractions by radiative efficiencies. Reproduced from Montzka et al. (2018)

government mandated emission reductions in China and India. This result clearly implies that unreported HFC-23 by-product emissions exist. Therefore, the global observation system of atmospheric HCFC-22 and HFC-23 abundances is important to monitor the efficacy of the phase-down under the Montreal Protocol and to accurately project the impact of emissions of these compounds on ozone depletion and climate change into the future.

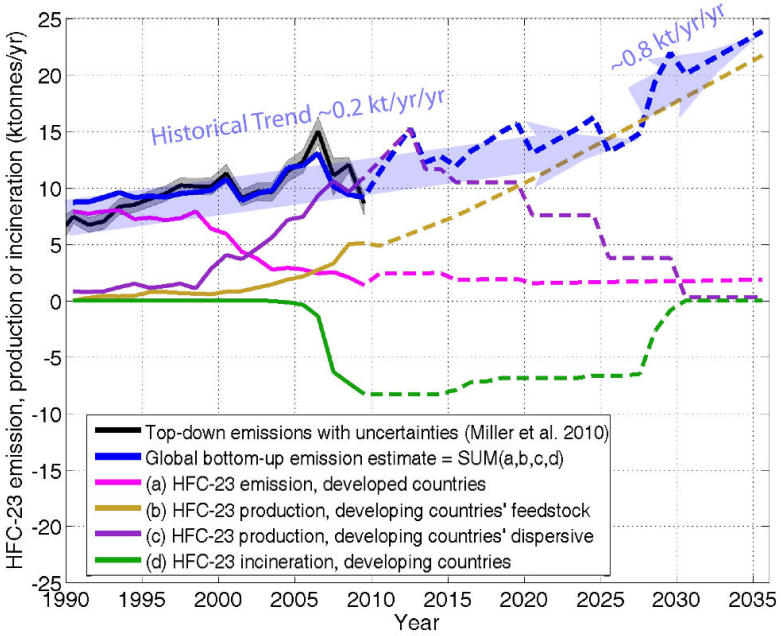

Figure 1.6: Bottom-up HFC-23 emissions for developed countries (solid line a), and HFC-23 production and incineration for developing countries (solid lines b − d), shown along with the bottom-up global HFC-23 emissions, which are the annual sums of each of these components. The bottom-up emissions, production and incineration are projected (dotted lines) to 2035 based on the "Reference Case" (RC) assumptions. Reproduced from Miller and Kuijpers (2011).

1.5.1 Measurements of atmospheric HFC-23

The history of in-situ observation of atmospheric HFC-23 is relatively short. Atmospheric HFC-23 abundances were first reported in Oram et al. (1998) based on gas chromatography-mass spectrometer (GC-MS) measurements of flask background air samples collected at Cape Grim, Tasmania, Australia (40.7°S, 144.7°E), from 1978 to 1995.

The Advanced Global Atmospheric Gases Experiment (AGAGE) observation network supported by a consortium of multinational institutions and organizations started high frequency in-situ measurements of HFC-23 after the late 2000s using the GC-MS-Medusa instrument at AGAGE stations (e.g. Cape Grim; Gosan, Jeju island, South Korea (33.3°N, 126.2°E)) (Miller et al., 2010; Kim et al., 2010; Simmonds et al., 2018a). Also, in-situ measurements of HFC-23 with AGAGE-compatible (but not identical) instruments have been operated at two stations of National Institute for Environmental Studies (NIES) in Japan: Hateruma, Okinawa (24.1°N, 123.8°E, since 2004) and Cape Ochiishi, Hokkaido (43.2°N, 145.5°E, since 2006) (Yokouchi et al, 2006; Fang et al., 2015). In total, there are, however, only 13 sites with HFC-23 in-situ measurements in the AGAGE network, including three affiliated stations.

Thanks to the evolution of molecular spectroscopy, and increasing atmospheric concentrations, space-borne remote sensing observation of HFCs, in addition to several CFCs and HCFCs, became possible (Nassar et al., 2006). For HFC-23, the first space-borne and balloon-borne remote sensing observations were done by the Atmospheric Chemistry Experiment-Fourier Transport Spectrometer (ACE-FTS) on SCISAT and the JPL MkIV interferometer, using the spectral region (1140–1160 cm^{-1}) covering the ν_2 and ν_5 vibrational-rotational transition bands of HFC-23 (Harrison et al., 2012). Fernando et al. (2019) reported the HFC-23 trend above cloud-top derived from the ACE-FTS measurements for the period of 2004–2017, and indicated that the annual HFC-23 mole fractions retrieved from the ACE-FTS consistently averaged 5% smaller than ones at ground level

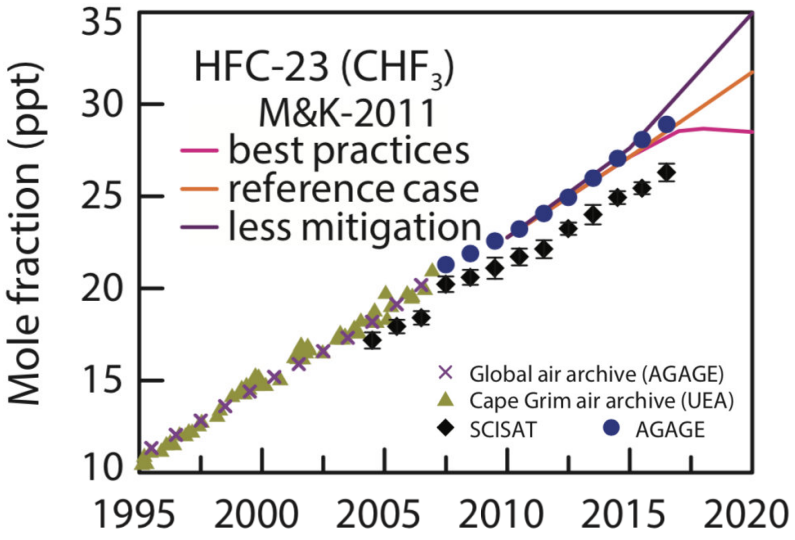

Figure 1.7: Annual mean mole fractions of HFCs and recent projections. Shown are global means estimated from in-situ instrumentation at five remote sites (AGAGE, dark blue filled circles). Global means derived from air archives in both hemispheres (AGAGE, purple crosses) are calculated using a 12-box model (Simmonds et al., 2018a). Results reported for the southern hemisphere from analyses of the Cape Grim Air Archive only are also shown (University of East Anglia (UEA) data, khaki triangles; Oram et al., 1998). Results from satellite absorption retrievals (SCISAT) represent upper troposphere-lower stratosphere means averaged from 60°N to 60°S (black diamonds; Harrison et al., 2012). Uncertainties on these satellite retrievals represent statistical variability in the data used in the averaging and do not include any systematic errors. Also shown are projections based on observations (M&K-2011; Miller and Kuijpers, 2011). Reproduced from Montzka et al. (2018)

from the AGAGE annual global mean dataset. However, the ACE-FTS observations do not have sensitivity to the troposphere where all HFC-23 emissions occur.

Figure 1.7 shows a plot consolidating these HFC-23 measurements from the in-situ and satellite in "Scientific Assessment of Ozone Depletion: 2018" (Montzka et al., 2018).

1.5.2 NDACC-IRWG

Established in 1991, the Network for the Detection of Stratospheric Change (NDSC) (Kurylo and Solomon, 1990) focused on observing and measuring stratospheric ozone, ozone-related chemicals, and meteorological variables, at a globally distributed set of ground-based remote-sensing stations. The network includes lidars and ultraviolet, visible, IR, and microwave instruments for total column and vertical profile measurements, as well as in situ aircraft and balloon sounding instruments. While the NDSC continues to monitor changes in the stratosphere with a focus on the ozone layer and its evolution, it now also evaluates trends in both stratospheric and tropospheric composition, investigates links between climate change and atmospheric composition, validates space-based measurements of the atmosphere, organizes scientific field campaigns, and contributes to the testing and the improvement of atmospheric models. To better reflect these purposes and the scientific focus on the altitudinal region between tropospheric and stratospheric, the network changed its name to the Network for the Detection of Atmospheric Composition Change (NDACC) in 2005 (De Mazière et al., 2018). Today, NDACC is composed of more than 70 globally distributed, ground-based, remote-sensing research stations with more

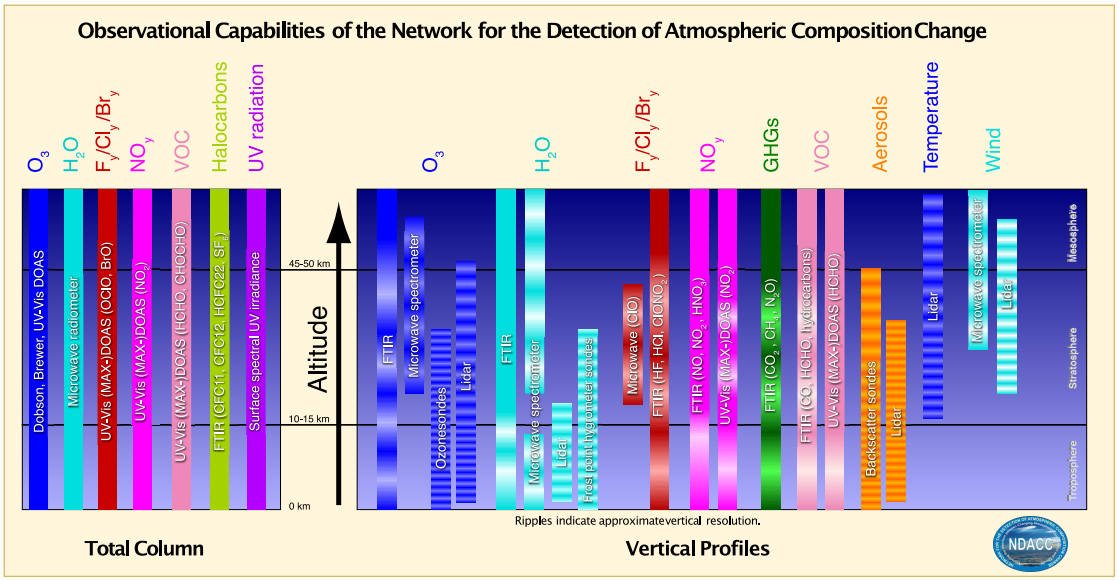

Figure 1.8: NDACC measurement capabilities, including species and parameters measured, instrumental measurement techniques, and each measurement's approximate vertical resolution (indicated by the ripple). Reproduced from NDACC home page (http://www.ndacc.org, last access: 8 January 2021.

than 160 currently active instruments and consists of nine working groups, representing the various techniques that are used in the network, as shown in Figure 1.8: Dobson and Brewer, Infrared, Lidar, Microwave, Ozone and Aerosol sondes, UV-visible, Spectral UV, Satellite, and Theory and Analysis.

The Network for the Detection of Atmospheric Composition Change - Infrared Working Group (NDACC-IRWG) has been globally monitoring abundances of various atmospheric trace gases (e.g. O_3, HCl, HNO_3, CH_4, CO) using ground-based Fourier transform infrared spectrometer (FTIR) instruments (De Mazière et al., 2018). At present,

the contributing ground-based FTIR instruments to the NDACC-IRWG are located at more than 20 sites around the world, and have yielded long-term consistent high-quality data by adherence to strict measurement and analysis procedures. For CFCs and HCFCs, for example, atmospheric CFC-11, CFC-12, and HCFC-22 have been retrieved from solar IR spectra taken by ground-based FTIRs at Reunion island (Zhou et al., 2016; Prignon et al., 2019). For HFCs, however, there has been no attempt to retrieve their atmospheric abundances. If routine observations of atmospheric HFC-23 using the NDACC's ground-based FTIRs were possible, we could fill spatial and temporal gaps in the existing observations by AGAGE and ACE-FTS, which would allow for monitoring of global atmospheric HFC-23 abundances in greater detail than ever.

1.6 Objects of this study

Monitoring of atmospheric HFC-23 is very important as mentioned above, but only 13 sites in the AGAGE network, including three affiliated stations, are currently available to measure atmospheric HFC-23 abundance from ground-based instrument in the world. By providing higher quality remote sensing observation data in addition to the AGAGE in-situ measurements, it is expected that the global emission status of HFC-23 will be analyzed in more detail. Moreover, if it was possible to retrieve atmospheric HFC-23 abundance from solar IR spectrum at surface, intercomparison between ground-based FTIR and satellite observations enables validation work of these remote sensing observations. This study aims

mainly to investigate the retrieval procedure of atmospheric HFC-23 using the overlapping ν_2 and ν_5 vibrational-rotational transition bands of HFC-23. I analyze solar IR spectra observed by two ground-based FTIRs installed at Rikubetsu, Japan, and Syowa Station, Antarctica. These retrieval results are validated by comparing with in-situ measurements from the AGAGE network or modelled annual global mean dataset based on the AGAGE measurements. Furthermore, retrieval of HCFC-22 which is closely relevant to HFC-23 were carried out as a part of my study in doctor course, and a relationship between HFC-23 and HCFC-22 retrieved from the FTIR observations at Rikubetsu is described in this thesis. In Chapter 2, a theory of measuring spectrum with FTIR instrument is summarized and a brief details of the FTIR observations at Rikubetsu and Syowa Station are described. In Chapter 3, the retrieval strategies of HFC-23 and retrieval error budgets for both sites are described in detail. Chapter 4 presents the retrievals of HCFC-22 at both sites following the retrieval strategy of the previous study (Prignon et al., 2019), including the retrieval error analysis. In Chapter 5, the trends of the FTIR-retrieved HFC-23 and HCFC-22 are compared to surface mole fraction data from the AGAGE network. In addition, the correlations between HFC-23 and HCFC-22, which are retrieved from the FTIR observations at Rikubetsu, are discussed with backward trajectory analysis of the air masses arriving at the site. Finally, conclusions and perspectives are summarized in Chapter 6.

Chapter 2

Fourier transform infrared spectrometry

It is important to understand the basic physical properties of atmospheric molecules in order to properly perform a study with the interaction between infrared radiation and atmospheric gases. Ground-based solar absorption FTIR spectrometry has been established as a powerful tool to measure the composition of the earth atmosphere. It uses the sun as a light source, and measures the solar spectrum in the infrared region. The gas molecules absorb solar radiation at certain frequency, so that we can determine the abundances (either total columns or profiles) of the atmospheric trace gases from the measured spectrum. In the following, it is explained how the transitions between energy states of molecule generate spectroscopic features of infrared region.

2.1 Radiative transfer

IR radiation is a part of electromagnetic wave which is synchronized oscillations of electric and magnetic fields. The speed of electromagnetic wave (light), c, in vacuum is given by:

$$c = \lambda\nu = 2.998 \times 10^8 \text{ [m s}^{-1}\text{]} \tag{2.1}$$

where λ is the wavelength and ν is the frequency. In IR spectroscopy, the unit for expressing radiation is the wavenumber, k, in unit of cm^{-1}:

$$k = \frac{1}{\lambda}. \tag{2.2}$$

IR radiation behaves like both waves and particles in the same time which have been explained by the theory of quantum mechanism. Therefore, the radiation behaving a particle is called a photon. The energy of a photon, E, depend only on its frequency, ν, or inversely, its wavelength λ:

$$E = h\nu = hck \tag{2.3}$$

where h is Planck's constant (6.626×10^{-34} J s).

The radiance I_{B} emitted by a black body with a temperature of T, dependent on

wavelength λ is described by Planck's law:

$$I_{\mathrm{B}}(\lambda) = \frac{2hc^2}{\lambda^5} \frac{1}{\exp\left(\frac{hc}{\lambda k_{\mathrm{B}} T}\right) - 1} \tag{2.4}$$

where k_{B} is Boltzmann's constant (1.381×10^{-23} J K^{-1}).Setting the derivative equal of Equation 2.4 to zero, Wien's displacement law is derived:

$$\lambda_m = \frac{0.2897}{T} \tag{2.5}$$

where λ_m is the wavelength of peak radiation from a black body at temperature T in unit of °C, and is expressed in unit of cm.

Figure 2.1 shows the spectrum of solar radiation measured outside the Earth's atmosphere and at sea level. The spectrum outside the atmosphere matches closely that of a blackbody at 5800 K. Therefore, the Sun is a good black body, and estimating from the spectrum the temperature at the Sun's surface is 5800 K. Solar radiation peaks in the visible range of wavelengths from 400 to 700 nm and is maximum at 500 nm (the green light). About half of total solar radiation is in the IR range and a small fraction is in the UV range. The solar radiation flux at sea level is weaker than at the top of the atmosphere, in part because of reflection by clouds. Furthermore, there are major absorption features by O_2 and O_3 in the UV and by H_2O, CO_2, and O_3 in the IR.

Since radiation reaching Earth from the Sun is well characterized as mentioned above,

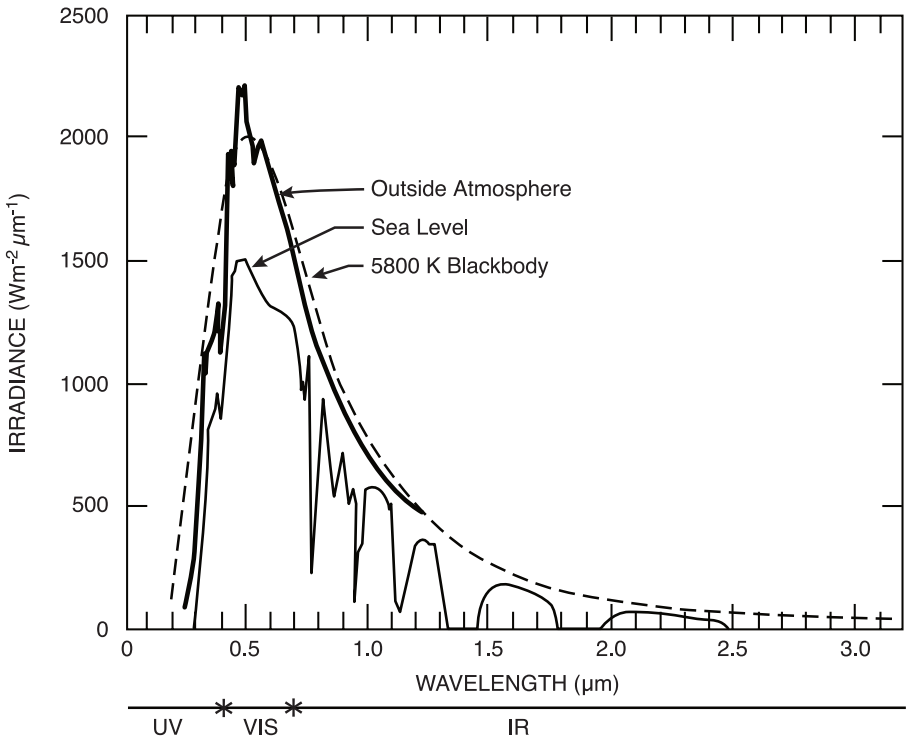

Figure 2.1: Solar radiation spectra measured from a satellite outside Earth's atmosphere (bold line) and at sea level, along with a spectrum from a black body at 5800 K (dashed line).

measurements of sunlight reaching the surface can be used to infer the composition of the atmosphere. As sunlight passes through the atmosphere, gases absorb some of that light. The absorption of sunlight at a particular wavelength can be described using the Beer-Bouguer-Lambert Law, or Beer's Law :

$$I(\lambda) = I_0(\lambda) \exp\left(-\frac{\tau(\lambda)}{\cos\theta}\right) \tag{2.6}$$

where I is the solar radiation intensity reached at the ground, I_0 is the solar radiation intensity at the top of the atmosphere, τ is the atmospheric optical depth, which is a measure of the absorption for solar radiation for a given λ cumulated in passing through a vertical air-column, and θ is the solar zenith angle (SZA). The atmospheric optical depth, τ, is defined by:

$$\tau(l) = \int_0^l \alpha(l)\mathrm{d}l = \int_0^l \rho(l)\sigma(l)\mathrm{d}l \tag{2.7}$$

where l is the ray path of the incident radiation, α is the absorption coefficient, ρ is the density of the air, and σ is the absorption cross section.

2.2 Infrared absorption spectrum

The molecules only absorb discrete and specific wavelengths, because only radiation that equal to the molecular energy state gaps can be absorbed or emitted. Therefore the absorption lines are assigned to certain molecules. The molecular spectra are divided into electronic transitions, vibrational transitions, and rotational transitions. The spectral types resulted from the three molecular transitions are summarized in Table 2.1. The electronic transition has the highest energy, and can be observed in the UV and visible region. The vibrational transition happens mainly in the IR region. The rotational transition has the lowest energy and it is dominantly in the microwave and far-infrared (FIR) region. Additionally, the electronic, vibrational, and rotational transitions can occur at the same time. In the IR region, the absorption involves changes in both the

vibrational and rotational states of the molecule, and results in vibrational-rotational transition.

Table 2.1: Summary of spectral types classified by molecular transitions.

Spectral type	**Transition**	**Spectral region**
Rotational	Rotational	Microwave, FIR
Vibrational-rotational	Vibrational, rotational	IR
Electronic	Electronic, vibrational, rotational	Visible, UV

The total internal energy of a gas molecule can be expressed by:

$$E = E_{\mathrm{e}} + E_{\mathrm{v}} + E_{\mathrm{r}} + E_{\mathrm{t}} \tag{2.8}$$

where E_{e} is the energy level of the orbits of the electrons in the atoms, E_{v} and E_{r} are the energy levels of the vibrational and rotational states in the molecule, and E_{t} is the translational energy related to the molecular motions. Quantum mechanics predicts that only certain configurations of electron orbits are permitted within each atom, and only certain vibrational frequencies and amplitudes and only certain rotation rates are permitted for a given molecular species. Each possible combination of electron orbits, vibration, and rotation is characterized by its own energy level, which represents the sum of the three kinds of energy. Note that the translational energy is not quantized in this matter.

To cause interaction between a molecule and electromagnetic wave, it is necessary for the molecule to couple with the electric field. This is generally facilitated though the

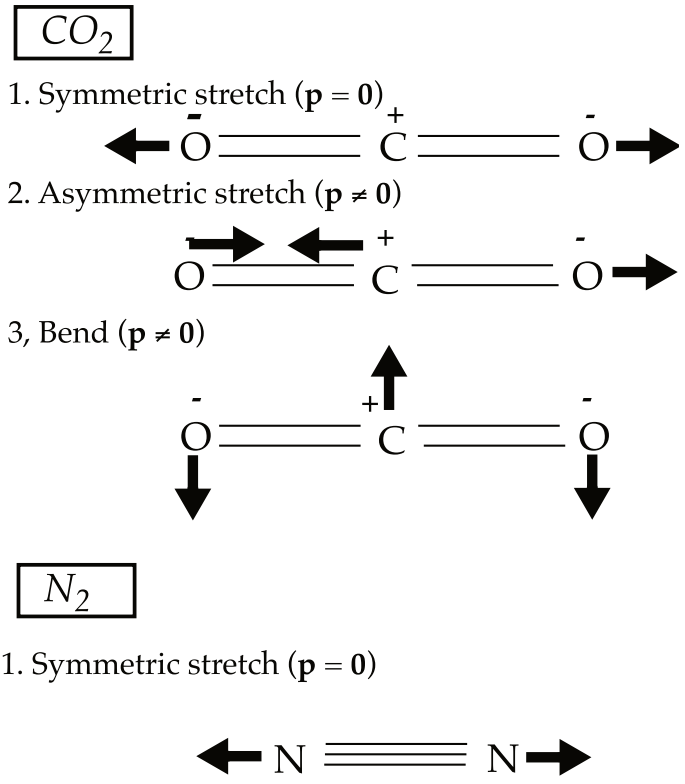

Figure 2.2: Normal vibrational modes of CO_2 and N_2. Reproduced from Jacob (1999).

electric dipole or quadrupole moment of the molecule. A selection rule from quantum mechanics is that vibrational transitions are allowed only if the change in vibrational state changes the dipole moment p of the molecule. Vibrational states represent different degrees of stretching or flexing of the molecule, and an electromagnetic wave incident on a molecule can modify this flexing or stretching only if the electric field has different effects on different ends of the molecule, that is if $p \neq 0$. Examination of the structure of the molecule can tell us whether a transition between two states changes p.

Molecules that have more complex charge orientations, such as H_2O, O_3, and CO_2, have dipole moments that allow for the absorption and emission of infrared radiation. In general, a linear molecule with N atoms has $3N - 5$ normal vibrational modes, while a nonlinear molecule has $3N - 6$ normal modes. Considering the CO_2 molecule as shown in Figure 2.2, its vibrational state is defined by a combination of three normal vibrational modes and by a quantized energy level within each mode. Vibrational transitions involve changes in the energy level (vibrational amplitude) of one of the normal modes (or rarely of a combination of normal modes). In the "symmetric stretch" mode the CO_2 molecule has no dipole moment, since the distribution of charges is perfectly symmetric; transition to a higher energy level of that mode does not change the dipole moment of the molecule and is therefore forbidden. Changes in energy levels for the two other, asymmetric, modes change the dipole moment of the molecule and are therefore allowed. In this manner, CO_2 has absorption lines in the IR region.

The most abundant gases in the atmosphere, O_2 and N_2, are linear and symmetrically charged, resulting in the absence of dipole moments. In the case of N_2, its molecule has a uniform distribution of charge and its only vibrational mode is the symmetric stretch as shown in Figure 2.2. Transitions within this mode are forbidden, and thus the N_2 molecule does not absorb in the IR region.

For a simple diatomic molecule allowed to rotate about its centre of mass, a rigid rotor model is adequate to describe its energy (Herzberg, 1950). The energy of the rotational

state in the molecule is given by:

$$E_{\mathrm{r}} = BJ(J+1) \tag{2.9}$$

where B is the rotational constant and $J = 0,\ 1,\ 2,\ \ldots$ is known as the rotational quantum number. B is expressed in units of wavenumbers and is composed of:

$$B = \frac{h^2}{8\pi^2 cI} \tag{2.10}$$

where I is the moment of inertia of the molecule. In classical physics, radiation of any frequency could be absorbed or emitted by a molecule with a dipole moment, however, quantum theory restricts the energy levels of the molecule to be only those described by Equation 2.9. Furthermore, Planck's relation (Equation 2.3) shows that changes between two adjacent energy levels, ΔE, give rise to distinct frequencies of radiation, ν:

$$\Delta E = h\nu. \tag{2.11}$$

This means that a purely rotational spectrum for a simple diatomic molecule would consist of lines equidistantly spaced at $2B$ cm^{-1} from one another. The transitions between states are governed by quantum mechanical selection rules, resulting in only $\Delta J = \pm 1$ being allowed for this model, refer to Herzberg (1950) for a detailed derivation of selection rules. For a slightly more complicated model in the non-rigid rotor, a centrifugal distortion

constant must be considered, which results in the lines of the rotational spectrum no longer being evenly spaced, but slightly skewed toward lower wavenumber values for higher rotational quantum numbers:

$$E_{\mathrm{r}} = BJ(J+1) - DJ^2(J+1) \tag{2.12}$$

where D is the constant representing the centrifugal distortion.

For more large and complicated polyatomic molecules, the changes in the rotational energy states are constrained by the different moments of inertia. For linear molecules, the rotational spectral lines are the same as those of simple diatomic molecules, although the spacing between lines is different. However, for molecules that have two different axes about which they can rotate, two different moments of inertia must be considered and, therefore, a second quantum number, K, must be introduced. Depending on the geometry of the molecule, different values of J and K are permitted, but beyond the scope of this study and not be considered in detail. Polyatomic molecules that have three axes of rotation are obviously the most complicated, and general analytical expressions for their energy states cannot be made.

The vibrational energy in case of a diatomic molecule can be written by:

$$E_{\mathrm{v}} = \frac{1}{2\pi c}\sqrt{\frac{k_{\mathrm{f}}}{\mu}}\left(v + \frac{1}{2}\right) \tag{2.13}$$

where k_f is the force constant, μ is the reduced mass of the molecule, and $v = 0,\ 1,\ 2,\ \ldots$ is the vibrational quantum number. As with rotational energy, it is important to note that transitions between different states of vibrational energy are restricted by the selection rule $\Delta v = \pm 1$. By considering Equations 2.13, this selection rule restricts the allowable transitions to all have the same energy. This means that there will be only one spectral line that corresponds to transitions between all vibrational energy states.

Obviously real molecules do not vibrate with simple harmonic oscillation, and are explained by the anharmonic oscillator model like the Morse Potential (Morse, 1929). The Morse Potential accounts for the anharmonic motion of real molecular bonds and allows for overtone and combination vibrational modes as shown in Table 2.2. Considering the Morse Potential, the vibrational energy states are given by:

$$E_\mathrm{v} = \omega_\mathrm{e}\left(v + \frac{1}{2}\right) - \omega_\mathrm{e}x_\mathrm{e}\left(v + \frac{1}{2}\right)^2 \tag{2.14}$$

where ω_e and x_e are the equilibrium oscillation frequency and anharmonicity constant, respectively derived from the Morse Potential Function. Using this model, the vibrational quantum number are permitted as:

$$\Delta v = \pm 1,\ \pm 2,\ \pm 3,\ \ldots \tag{2.15}$$

that is, transitions between all vibrational energy states are allowed.

Table 2.2: Vibrational transition.

Vibrational transition	**Name of transition**
$v = 0 \rightarrow v = 1$	Fundamental mode
$v = 0 \rightarrow v = 2$	First overtone
$v = 0 \rightarrow v = 3$	Second overtone
$v = 0 \rightarrow v = 4$	Third overtone

For a simple diatomic molecule, the vibrational-rotational energy states are expressed as the sum of the two terms:

$$\begin{aligned} E_{\mathrm{v,r}} &= E_{\mathrm{v}} + E_{\mathrm{r}} \\ &= \omega_{\mathrm{e}} \left(v + \frac{1}{2} \right) - \omega_{\mathrm{e}} x_{\mathrm{e}} \left(v + \frac{1}{2} \right)^2 + BJ(J+1) - DJ^2(J+1). \end{aligned} \tag{2.16}$$

The quantum mechanical selection rules for these energy states are a combination of the previous rules:

$$\Delta v = \pm 1,\ \pm 2,\ \pm 3,\ \ldots;\ \Delta J = \pm 1. \tag{2.17}$$

Therefore, for each value of v (i.e. for each vibrational band), there are a large number of rotational lines that correspond to various J numbers. Figure 2.3 shows the spectral lines that correspond to the fundamental vibrational mode (ν_2) of CO_2. Three distinct branches of spectral lines are apparent. The branch on the left side of the spectrum (low wavenumber side) is called the P-branch, and that on the right side (high wavenumber side) is called the R-branch. These branches of rotational lines correspond to the energy

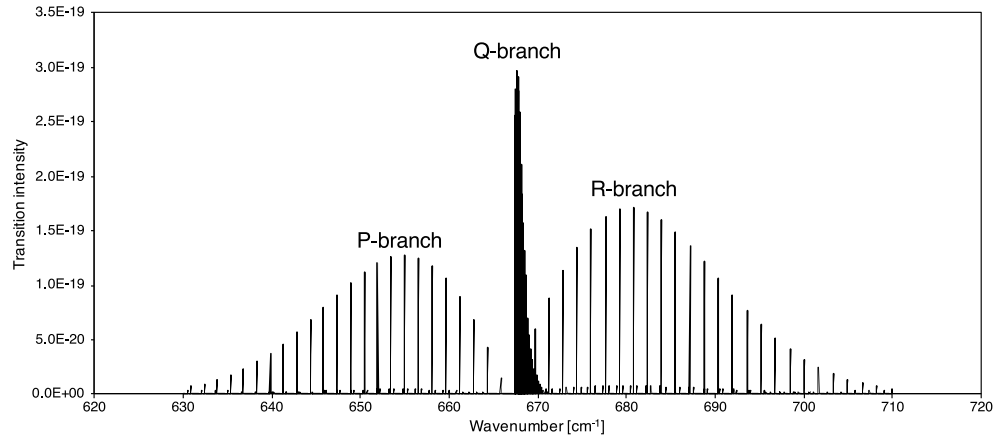

Figure 2.3: Line intensities of various rotational transition corresponding to the ν_2 fundamental vibrational mode of CO_2, using the spectroscopic parameters from the HITRAN 2016 database.

transitions between the different allowable states. The lines in the P-branch are for all $\Delta J = -1$ transitions, while those of the R branch represent the $\Delta J = +1$ transitions. Similarly structured P and R branches are found for all the other vibrational modes of CO_2. For polyatomic molecules, the simplifying assumption of vibration and rotation being decoupled no longer holds true. Linear polyatomic molecules can also vibrate in a manner such that the dipole moment is changed perpendicular to the principal axis of rotational symmetry and in this case the selection rules also allow $\Delta J = 0$ (i.e. the vibrational energy change can occur without an accompanying rotational transition). In such spectra, the Q-branch appears at the band center between the P and R-branches (around the fundamental vibrational frequency). The intensity of Q-branch is relatively

strong because the vibrational transitions occur from all existing rotational states with approximately the same energy change. For large polyatomic molecules, their spectra are more complex, and require the introduction of a supplementary rotational quantum number K, but beyond the scope of this study.

2.3 Line intensity

The line intensity by a transition, S, is related to the monochromatic absorption coefficient α_k:

$$S = \int_{-\infty}^{\infty} \alpha_k \mathrm{d}k \tag{2.18}$$

where k is the wavenumber. If local thermodynamic equilibrium is assumed then the state occupations in a molecule can be assumed to follow a Boltzmann distribution. Therefore, the intensity, in unit of $\mathrm{cm}^{-1}/(\mathrm{molecule\ cm}^{-2})$, of an absorption line with a central wavenumber, k_0, at absolute temperature T is given by:

$$S(T) = S(T_{\mathrm{ref}}) \frac{Q(T_{\mathrm{ref}})}{Q(T)} \frac{\exp\left(\frac{-hcE''}{k_{\mathrm{B}}T}\right)}{\exp\left(\frac{-hcE''}{k_{\mathrm{B}}T_{\mathrm{ref}}}\right)} \frac{\left[1 - \exp\left(\frac{-hck_0}{k_{\mathrm{B}}T}\right)\right]}{\left[1 - \exp\left(\frac{-hck_0}{k_{\mathrm{B}}T_{\mathrm{ref}}}\right)\right]} \tag{2.19}$$

where T_{ref} is a reference temperature which is generally 296 K, Q is a factorizing term called the partition function, and E'' is the lower (ground) state energy of the vibrational-rotational transition.

The partition function Q is very important since it governs to a large extent the

temperature dependency of the line intensity. It describes the internal energy distribution of the molecule between rotational, vibrational, and electronic states. Since the energy levels are well separated, the partition function, $Q(T)$ can be expressed as:

$$Q(T) = Q_{\mathrm{r}}(T)Q_{\mathrm{v}}(T)Q_{\mathrm{e}}(T) \tag{2.20}$$

where Q_{r}, Q_{v}, and Q_{e} are the partition functions of the rotational, vibrational, and electronic parts, respectively. The temperature dependency of the rotational partition function, $Q_{\mathrm{r}}(T)$, can be approximated by:

$$Q_{\mathrm{r}}(T) = \left(\frac{T_{\mathrm{ref}}}{T}\right)^{j} \tag{2.21}$$

where j is 1.0 or 1.5 for a linear molecule or a non-linear molecule, respectively. The vibrational partition function $Q_{\mathrm{v}}(T)$ is calculated by modeling the molecule as a harmonic oscillator:

$$Q_{\mathrm{v}}(T) = \prod_{i} \left[1 - \exp\left(\frac{-h\nu_i}{k_{\mathrm{B}}T}\right)\right]^{-d_i} \tag{2.22}$$

where ν_i is the fundamental frequency of mode i and d_i is the degeneracy, which is normally 1. For example, the degeneracy, d, for the bending mode ν_2 of C_2O is 2. With a few exceptions, $Q_{\mathrm{e}}(T)$ can be approximated as unity for temperatures found in the atmosphere. Neglecting the effect of stimulated emission, thus the temperature dependency of the line intensity can be written by:

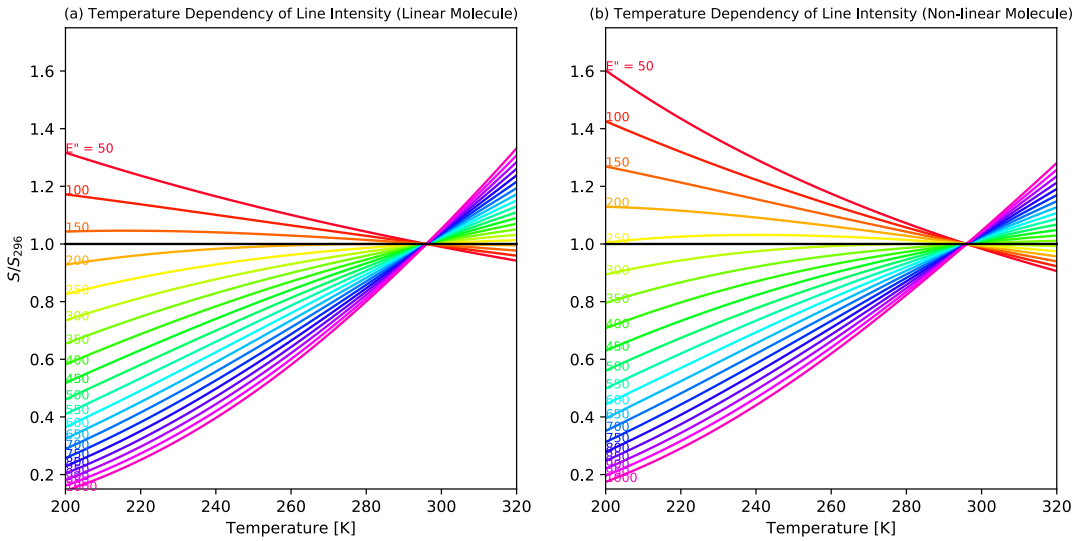

Figure 2.4: Temperature dependencies of line intensities for a linear molecule (a) and for a non-linear molecule (b).

$$S(T) = S(T_{\mathrm{ref}}) \left(\frac{T_{\mathrm{ref}}}{T}\right)^{j} \frac{\prod \left[1 - \exp\left(\frac{-h\nu_i}{k_{\mathrm{B}} T_{\mathrm{ref}}}\right)\right]^{-d_i}}{\prod \left[1 - \exp\left(\frac{-h\nu_i}{k_{\mathrm{B}} T}\right)\right]^{-d_i}} \frac{\exp\left(\frac{-hcE''}{k_{\mathrm{B}} T}\right)}{\exp\left(\frac{-hcE''}{k_{\mathrm{B}} T_{\mathrm{ref}}}\right)}. \tag{2.23}$$

Figure 2.4 shows the temperature dependencies of the line intensities for a linear molecule and for a non-linear molecule. In case of a line having E'' of 500 cm^{-1}, the intensity at 240 K is about 30% weaker than at 296 K for a linear molecule.

In reality, the spectral lines are never monochromatic and have a certain width, depth and shape due to the perturbations in the energy levels as a result external influences on the molecule, which are determined by the temperature and pressure of the gas.

2.4 Line shapes

2.4.1 Collisional broadening

Collisional broadening occurs as a result of collisions between molecules in a gas. The line shape function f_{L} of the spectral line is given by a Lorentzian profile (Liou, 2002):

$$f_{\mathrm{L}}(k) = \frac{\alpha_{\mathrm{L}}\pi^{-1}}{\alpha_{\mathrm{L}}^2 + (k - k_0 - \delta_{\mathrm{L}})^2} \tag{2.24}$$

where k_0 is the center wavenumber, α_{L} is the half width at half maximum (HWHM) of the collision-broadened line at pressure p and temperature T given by:

$$\alpha_{\mathrm{L}} = \left(\frac{T_0}{T}\right)^{n_{\mathrm{air}}} [\gamma_{\mathrm{air}}(T_0, p_0)(p - p_{\mathrm{self}}) + \gamma_{\mathrm{self}}(T_0, p_0)p_{\mathrm{self}}]. \tag{2.25}$$

The pressure-dependent shift of the line center frequency, $\delta_{\mathrm{L}} = \delta_{\mathrm{air}}p$, is introduced in Equation 2.24 to account for the failure of the strong collision approximation at high pressures, where δ_{air} is the coefficient of the air-broadened pressure shift [cm^{-1} atm^{-1}] measured at a reference temperature and pressure ($T_0 = 296$ K, $p_0 = 1$ atm). δ_{L} has a temperature dependence of the same form as α_{L}, and n_{air} is used in the absence of other information. The α_{L} [cm^{-1}] is calculated with the different air- and self-broadening coefficients, γ_{air} and γ_{self} [cm^{-1} atm^{-1}], which are also measured at $T_0 = 296$ K and $p_0 = 1$ atm, the partial pressure of the gas, p_{self}, and the exponent of the temperature dependence of the broadening coefficients, n_{air}. Equation 2.25 assumes one temperature dependence for

both the self- and air-broadening processes in the absence of other information (n_{air} takes on different values depending on the nature of the colliding partners and the particular transition).

Collisional broadening is greatest in the troposphere below about 20 km due to the pressure dependence of the Lorentz line shape.

2.4.2 Doppler broadening

Doppler broadening is the result of the relative motion of the molecule along the line of sight. The line shape function f_{D} for a Doppler-broadened line is given by (Liou, 2002):

$$f_{\text{D}}(k) = \frac{1}{\alpha_{\text{D}}\sqrt{\pi}} \exp\left[-\frac{(k-k_0)^2}{\alpha_{\text{D}}}\right] \tag{2.26}$$

where α_{D} is a measure of the Doppler-broadened line width and is given by:

$$\alpha_{\text{D}} = k_0\sqrt{\frac{2k_{\text{B}}T}{mc^2}} \tag{2.27}$$

where m is the mass of the molecule, c is the speed of light. Doppler broadening dominates in the stratosphere above about 50 km as a result of its temperature dependence.

2.4.3 Voigt line shape

In the atmosphere, where both collisional and Doppler broadening occur, the line shape can be modelled by the convolution of the Lorentz and Doppler line shapes (Liou,

2002) known as the Voigt line shape:

$$\begin{aligned} f_{\mathrm{V}}(k) &= f_{\mathrm{L}}(k) * f_{\mathrm{D}}(k) \\ &= \frac{y}{\alpha_{\mathrm{D}}\pi^{3/2}} \int_{-\infty}^{\infty} \frac{\exp\left(-k'^2\right)}{(x-k')^2+y^2} \mathrm{d}k' \end{aligned} \tag{2.28}$$

where $x = (k - k_0)/\alpha_{\mathrm{D}}$ and $y = \alpha_{\mathrm{L}}/\alpha_{\mathrm{D}}$. The Voigt line shape is commonly used in spectroscopy to represent the line shape of an absorbing gas in the atmosphere.

2.5 HITRAN database

The HITRAN (High Resolution Transmission) database is a research-standard database containing reference temperature and pressure line strengths ($S(k_0)$) and pressure-broadening and shift parameters (γ_{air}, γ_{self}, δ_{air}, along with their temperature dependence exponent n_{air}) for the vibrational-rotational transitions of various atmospheric molecules. The database also contains lower state energy (E'') information necessary for the line strength calculation and several other quantum mechanical parameters. The current version, HITRAN2016, contains the line-by-line parameters for 49 molecules and, with their respective isotopologues. More accurate measurements are continuously being compiled for updates of the database. In addition to line-by-line parameters, cross-section data and aerosol indices of refraction are also included for some species in some pressure, temperature and wavenumber ranges (Gordon et al, 2017).

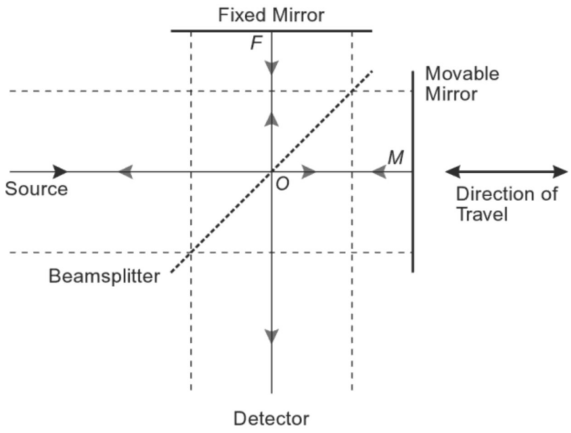

Figure 2.5: Michelson interferometer schematic diagram. Reproduced from Griffiths and de Haseth (2007).

2.6 Fourier transform infrared spectrometry

The science of Fourier transform interferometry was initiated in 1880, when Albert Michelson invented the interferometer (Bell, 1972). It remains the back-bone of many interferometers used today. The optical diagram of the basic Michelson interferometer is shown in Figure 2.5.

Figure 2.6 shows the path followed by light in a Bruker-made IFS-120M instrument as a modern FTIR instrument. Basically, the light passes through the input aperture into the interferometer compartment of the instrument, where the beam is collimated by a parabolic collimating mirror, and then the collimated beam is directed to the filter wheel. The rotating filter wheel contains several spectral bandpass filters to limit the sampled spectral range of the beam. The filtered beam is directed onto the beamsplitter where it

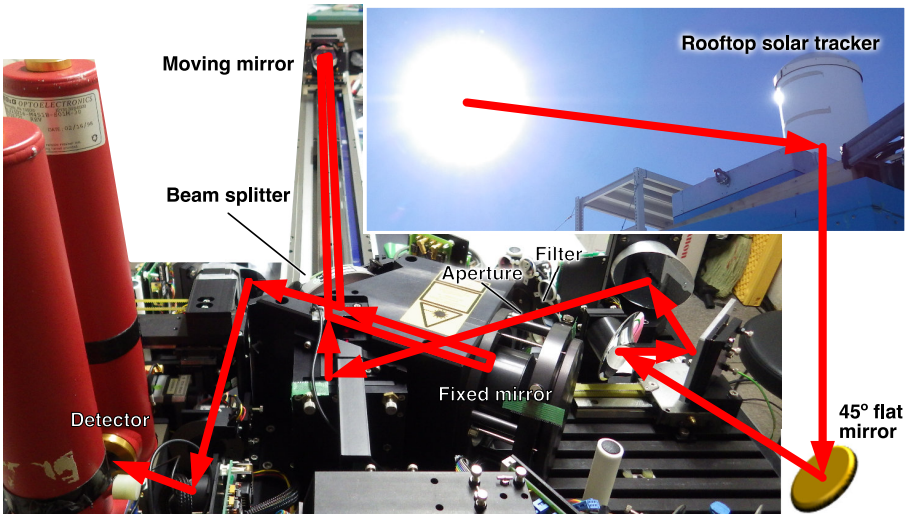

Figure 2.6: Diagram of a Bruker IFS-120M FTIR instrument at Syowa Station. Red arrows show the path of light.

is split into two beams of equal intensity. One beam is directed onto the fixed mirror and the other to the scanning mirror in the interferometer arm. The two beams are directed back to the beamsplitter and due to their optical path difference (OPD), there is a phase difference between the two. The beams are recombined at the beamsplitter and directed to one of two detectors through a series of flat mirrors and a parabolic mirror. Details of the bandpass filters and detectors of the instruments at Syowa Station and Rikubetsu are discussed in Section 2.8.1 and 2.8.4, respectively.

The detector measures the intensity of the interfered beam, where the beam intensity is given by:

$$I(x) = \frac{1}{2}\int_0^\infty B(k)\cos(2\pi kx)\mathrm{d}k \tag{2.29}$$

where $I(x)$ is the intensity as a function of OPD x and $B(k)$ is the intensity of the input beam as a function of wavenumber k. Applying a Fourier transform to Equation 2.29, we obtain $B(k)$:

$$B(x) = 2\int_0^\infty I(x)\cos(2\pi kx)\mathrm{d}x. \tag{2.30}$$

The measured intensity $I(x)$ is the interferogram, which is the interference pattern as a result of varying phase difference as the scanning mirror is moved along the path of the interferometer arm. The quantity $B(k)$ is the measured spectrum, which is the solar absorption spectrum or lamp spectrum of the input beam.

The integrals of Equations 2.29 and 2.30 are an idealization of the real-world case as these expressions assume an OPD ranging from 0, defined as the zero path difference (ZPD), to infinity. In reality, the interferometer has a finite maximum OPD resulting in a finite resolution of the sampled spectrum. Therefore, an apodization is applied to Equation 2.8. A boxcar apodization is generally used in the form:

$$D(x) = \begin{cases} 0 & \text{if } |x| > x_{\max} \\ 1 & \text{if } |x| \leq x_{\max} \end{cases} \tag{2.31}$$

where x is the OPD and $x_{\max}$ is the maximum OPD. Applying the convolution of Equation 2.31 with Equation 2.29 results in a sinc function after the Fourier transform. The applied apodization therefore influences the resolution of the sampled spectrum. For a boxcar apodization, the resolution is defined using the full width at half maximum (FWHM),

corresponding to a resolution of $0.6/x_{\max}$ (Bell, 1972). For the Bruker IFS 120M, the manufacturer defines the resolution as $0.9/x_{\max}$.

There are advantages to using FTIR instrument compared to prism and grating (dispersive) instruments. An FTIR instrument can measure simultaneously the entire spectrum covering all wavelengths of the input light (Fellgett, 1958). This reduces the measurement time compared to dispersive instruments that must measure a small range of an overall spectrum. Especially, this is advantageous when a large range of wavelengths are of interest.

While dispersive instruments input light through a narrow slit which limits the amount of light, the circular aperture in the FTIR instrument allows more amount of light into the instrument and therefore is possible to measure the spectrum with high signal-to-noise ratios (SNRs) (Jacquinot, 1960).

Furthermore, FTIR measurement has high wavenumber precision because the sampling of interferogram can be calibrated by a laser beam of known wavelength (e.g. red helium-neon (He-Ne) laser at 633 nm) that passes through the interferometer (Connes and Connes, 1966). The consistent sampling at accurate OPD enables the addition and subtraction of interferograms.

2.7 Instrumental line shape

The information on the instrumental line shape (ILS) is derived from two parameters in the interferogram domain: modulation efficiency and phase error. The modulation efficiency is a measure of the attenuation of the signal intensity on the detector as a function of OPD when compared with ideal instrument. The phase error is a measure of the asymmetry of the ILS. The interferogram $\tilde{I}(x)$ as a function of OPD, x, is given by:

$$\tilde{I}(x) = A(x)M(x)\int_{-\infty}^{\infty} S(k)\cos[2\pi kx + \phi(x)]dk, \tag{2.32}$$

where $A(x)$ is the apodization function, $M(x)$ is the modulation efficiency, $S(k)$ is the monochromatic spectrum at wavenumber k, and $\phi(x)$ is the phase error. For an ideal instrument, the interferogram is un-apodized: $A(x) = 1.0$, $M(x) = 1.0$, and $\phi(x) = 0.0$. The measured spectrum $\tilde{S}(k)$ is given by Fourier transform of $\tilde{I}(x)$:

$$\begin{aligned} \tilde{S}(x) &= \mathfrak{F}[\tilde{I}(x)] \\ &= S(k) \otimes \mathcal{ILS}(k) \end{aligned} \tag{2.33}$$

where $\mathfrak{F}$ is the Fourier transform operator and $\mathcal{ILS}(x)$ is the instrumental line shape function.

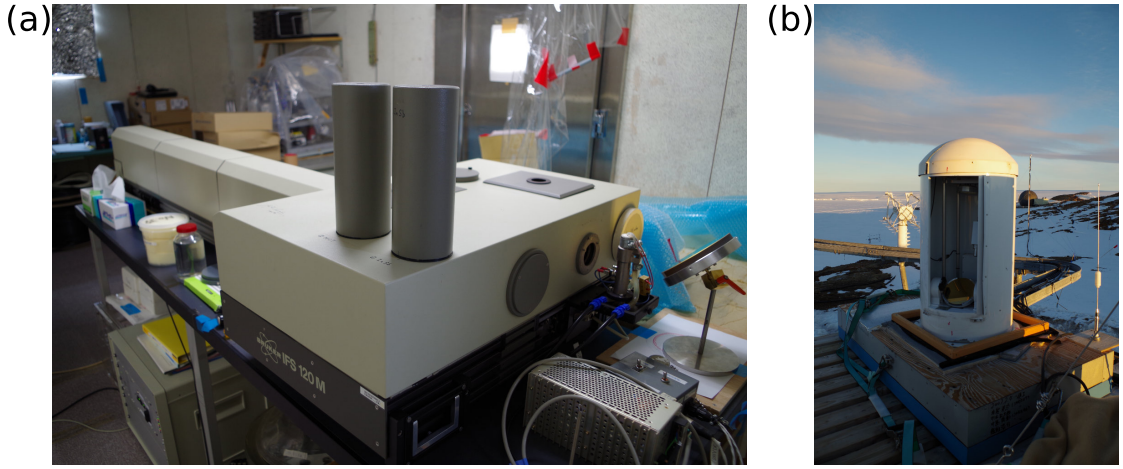

Figure 2.7: The setup of the FTIR instrument at Syowa Station. (a) The IFS-120M FTIR instrument equipped in the observation building at Syowa Station. (b) The solar tracker set in the rooftop of the building.

2.8 Measurements

2.8.1 The IFS-120M FTIR at Syowa Station

Since the Japanese Antarctic Syowa Station (69.0°S, 39.6°E; 10 m a.s.l.) was established in 1957, various kinds of scientific observations (e.g. meteorology, upper atmospheric physics, cryospheric sciences, biology, geology) have continuously been conducted around the station. Syowa Station has been maintained by members of the Japanese Antarctic Research Expedition (JARE) each year. In 2007, a Bruker IFS-120M FTIR instrument was installed in the observation building at Syowa Station by NIES and Tohoku University, in cooperation with the 48th JARE (JARE-48) members. Measurements using

Table 2.3: NDACC optical narrow bandpass filters used in the FTIR observations at Syowa Station, wavenumber range, wavelength range, aperture diameter, and the retrieved species

Filter	Wavenumber range [cm^{-1}]	Wavelength range [μm]	Aperture diameter [mm]	Retrieved species
0	4000–7500	1.33–2.50	0.3	CO_2
1	3900–4400	2.27–2.56	0.5	HF
2	2800–3700	2.70–3.57	0.5	HCN, C_2H_2, H_2CO
3	2400–3200	3.13–4.17	0.5	CH_4, C_2H_6, N_2O, HCl, O_3, H_2CO, H_2O
4	2000–2600	3.85–5.00	0.65	CO
5	1700–2200	4.55–5.88	0.65	CO, OCS, N_2O
6	500–1400	7.14–20.0	0.85	O_3, $ClONO_2$, HNO_3, CH_3OH, HCOOH, NH_3, CFC-11, CFC-12, HCFC-22
7*	500–1100	9.09–20.0	0.85	O_3, $ClONO_2$, HNO_3, NH_3, CFC-11, HCFC-22
8*	1000–1400	7.14–10.0	0.85	CH_3OH, HCOOH, CFC-12

the FTIR at Syowa Station contributed to research related to stratospheric composition near the edge of the polar vortex during ozone hole evolution, due to its geographical location (Nakajima et al., 2020). As the station is a remote site in Antarctica, it is possible to observe the background atmosphere of the southern hemisphere which it is not influenced by local human activity.

As shown in Figure 2.7, the FTIR observation at Syowa Station had been operated with a solar tracker and the IFS-120M instrument. The solar tracker set on the observation building roof guides a solar beam into the room, and then the solar beam is guided toward to the entrance window to the IFS-120M instrument through a 45° flat mirror. The IFS-120M instrument is operated using an annexed personal computer (PC) with Windows XP as an operating system. A Bruker-made OPUS software installed in the PC

can measure a spectrum by individual setting parameters (e.g. optical filter, aperture diameter, number of scans, detector, gain amplification). The solar tracker is independently controlled with control switches in the room.

The instrument had two liquid nitrogen-cooled detectors: a photovoltaic indium-antimonide (InSb) and a photoconductive mercury-cadmium-telluride (HgCdTe, well-known as MCT). Solar mid-infrared (MIR) spectra from 500 to 7500 cm^{-1} were recorded using a potassium bromide (KBr) beam splitter and the NDACC recommended optical bandpass filters, under clear-sky conditions in 2007, 2011 and 2016, but not the polar night period. The spectral intervals of the NDACC optical filters are listed in Table 2.3, along with corresponding aperture sizes and available atmospheric trace gases for retrieval.

The InSb detector is sensitive to light between about 1800 and 10000 cm^{-1}. The MCT detector is sensitive to light between about 600 and 5000 cm^{-1}, but if higher solar flux reaches the detector then its non-linearity response appears prominently. Therefore, a narrow bandpass filter must be used for a measurement using the MCT detector. For the FTIR measurements at Syowa Station since 2011, two narrow bandpass filters covering the interval of 500–1100 cm^{-1} (filter #7) and 1000–1400 cm^{-1} (filter #8) were used as alternative of the filter #6 covering the interval of 500–1400 cm^{-1}.

In this study, the spectra covering 500–1400 cm^{-1} measured with the MCT detector are used to retrieve atmospheric HFC-23 and HCFC-22. Typically, measurements with 2 scans were executed to acquire a spectrum with resolution of 0.0035 cm^{-1}, however, sometimes 4 to 16 scans were co-added in order to improve signal-to-noise ratios (SNR).

For HFC-23 retrieval, these spectra are degraded to the resolution of 0.0070 cm^{-1} (see Section 3.3).

2.8.2 Monitoring instrument performance

The optical system of the IFS-120M instrument at Syowa Station was in suitable condition at installation in 2007. Drift of the optical components in the instrument is likely over time during routine operation of the instrument. Therefore, important to monitor the alignment of the instrument on a routine basis. The instrument alignment is monitored by the measurement of the absorption spectrum of a hydrogen bromide (HBr) gas cell, filled with a known amount of HBr, using an internal MIR lamp source of the instrument (Coffey et al., 1998). The FTIR performance check with the HBr cell need a background (no cell) measurement and a measurement with the cell placed on the light path between the internal lamp source and the interferometer. For both the background and cell measurement, 64 co-added scans are performed using the NDACC filter #4 and 0.65 mm diameter aperture. These spectra are measured with 0.0035 cm resolution (maximum OPD of 257 cm). To obtain a transmission spectrum which contains the HBr absorption lines to be fitted, the cell spectrum is divided by the background spectrum. The fitted microwindows is listed in Table 2.4.

The transmission spectrum of HBr is analyzed with LINEFIT version 14. The detail of the LINEFIT algorithm is described by Hase et al. (1999). LINEFIT generates a theoretical ILS, modulation efficiency (MOD), and phase error (PHA) based on the in-

Table 2.4: HBr absorption lines for calculating the ILS of the IFS-120M instrument at Syowa Station

Filter	Wavenumber range [cm^{-1}]
1	2590.32–2590.72
2	2590.71–2591.11
3	2605.60–2606.00
4	2606.00–2606.40
5	2620.39–2620.79
6	2620.80–2621.20
7	2634.70–2635.10
8	2635.10–2635.50
9	2648.50–2648.90
10	2648.90–2649.30
11	2661.76–2662.16
12	2662.18–2662.58
13	2674.52–2674.92
14	2674.94–2675.34

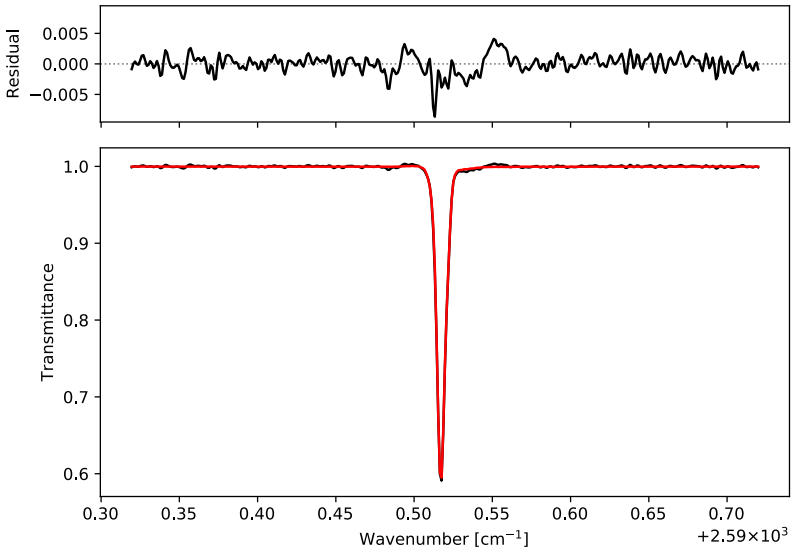

Figure 2.8: Typical fit and the residual for HBr absorption line around 2590.5 cm^{-1}.

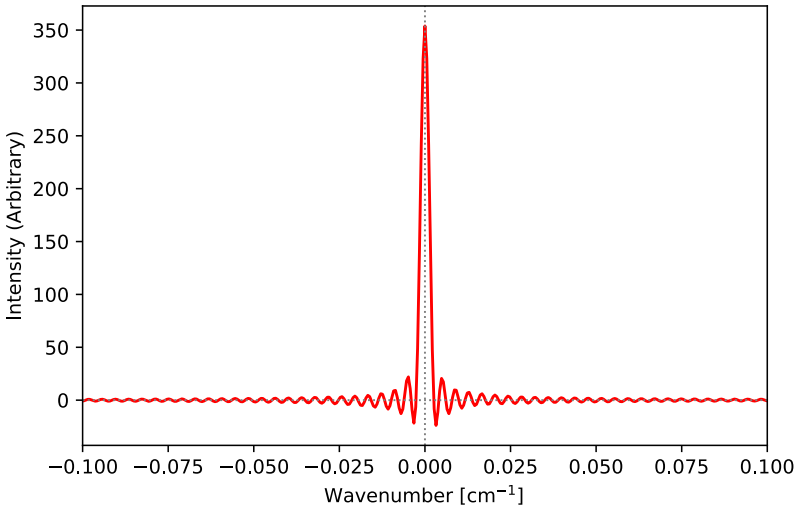

Figure 2.9: ILS obtained from the HBr cell measurement performed on 28 March 2016 using the FTIR instrument at Syowa Station.

strument field of view (FOV) and OPD. The ILS, MOD, and PHA are iteratively varied to match a simulated spectrum to the measured HBr absorption lines. Typical fit and the residual (measured - calculated spectrum) for HBr absorption line around 2590.5 cm^{-1} are shown in Figure 2.8 and the ILS obtained from the HBr cell measurement performed on 28 March 2016 using the IFS-120M instrument at Syowa Station is shown in Figure 2.9.

2.8.3 The FTIR observations in the JARE-57 activity

As part of my doctoral course, I participated in the JARE-56 summer party from November 2014 to March 2015 and the JARE-57 wintering party from December 2015 to March 2017, and actually performed FTIR observations and maintenance of the instrument at Syowa Station. In the JARE-56 summer activity, I mainly carried out preliminary check and maintenance of the IFS-120M instrument and some test measurements in preparation for FTIR observations in the JARE-57 wintering activity. The JARE-57 wintering activity at Syowa Station was done from February 2016 to January 2017. Until March in 2016, I carried out alignment works of the IFS-120M instrument. The modulation efficiency (MOD) and phase error (PHA) values of the ILS functions between March 2007 and March 2016 are shown in Figure 2.10. From March 2007 to February 2016, MOD and PHA for the IFS-120M instrument gradually deteriorated from their ideal state (MOD=1 and PHA=0). However, due to this alignment work, both MOD and PHA improved significantly on 28 March 28, 2016.

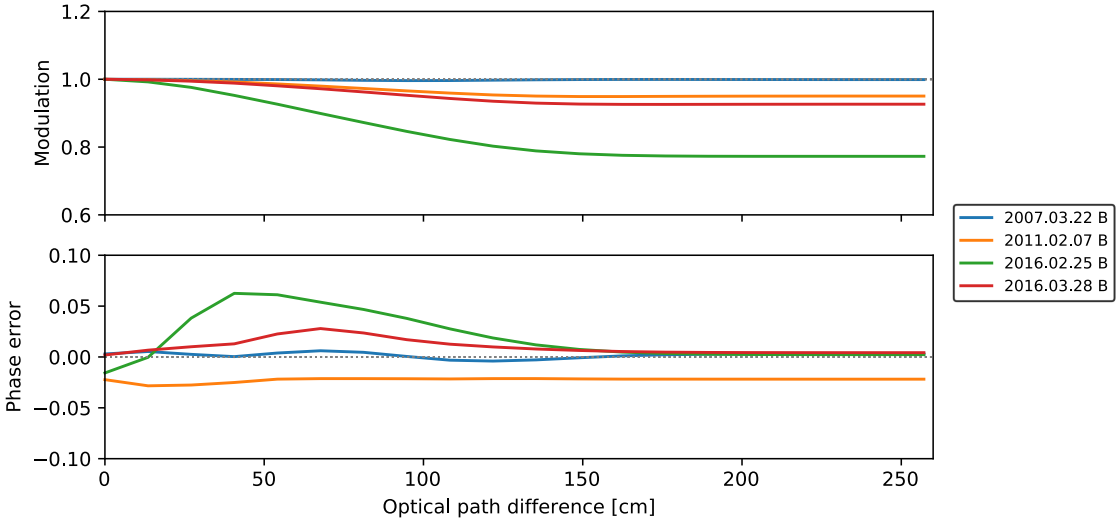

Figure 2.10: Modulation efficiency (upper panel) and phase error (lower panel) for the IFS-120M instrument at Syowa Station between March 2007 and March 2016. These values were analyzed using LINEFIT version 14.

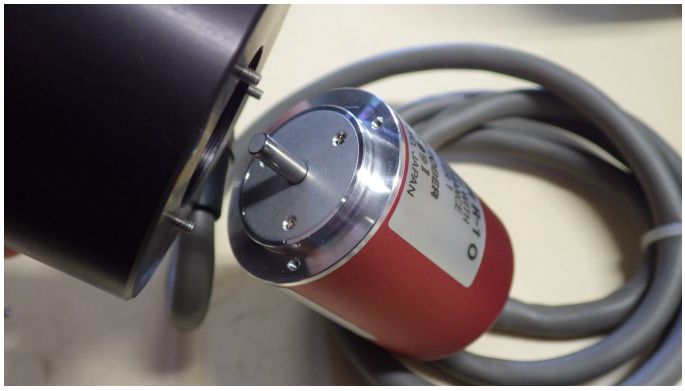

Figure 2.11: Laser rotary encoder that monitors the rotation speed of the scanner DC motor.

Table 2.5: Number of spectra acquired with the IFS-120M instrument at Syowa Station during the JARE-57 wintering activity.

		2016					2017	
Filter	Wavenumber range [cm^{-1}]	Mar.	Apr.	May.	Nov.	Dec.	Jan.	Total
0	4000–7500	2	2	0	3	17	2	26
1	3900–4400	1	2	0	3	14	2	22
2	2800–3700	1	2	0	4	15	2	24
3	2400–3200	1	2	0	4	16	2	25
4	2000–2600	1	3	0	4	14	1	23
5	1700–2200	0	3	0	4	11	1	19
7	500–1100	3	5	1	7	20	2	38
8	1000–1400	2	4	1	5	20	2	34

The number of spectra acquired with the IFS-120M instrument at Syowa Station between March 2016 and January 2017 is summarized in Table 2.5. In early May 2016, FTIR measurement became impossible due to a malfunction of the movable mirror (scanner) of the IFS-120M instrument. This is because the laser rotary encoder (Figure 2.11), monitoring the rotation speed of the DC motor that drives the scanner, reached the end of its life. Since it was not possible to transport to Syowa Station in winter, replacement parts were procured by air transport in November 2016, and replacement work was carried out immediately. After the replacement work, the instrument worked without any problems and continued to acquire solar infrared spectra until early January 2017.

2.8.4 The FTIR instruments at Rikubetsu

Measurements of atmospheric trace gases at Rikubetsu, Hokkaido, Japan (43.5°N, 143.8°E), have been carried out using two high spectral resolution FTIR instruments since May 1995, contributing to the NDACC-IRWG. The site is 200 km east of Sapporo and located in a small town surrounded by forests and pastures. In October 1997, this observatory was relocated to the top of a hill (380 m a.s.l.) in the vicinity of the town. The first instrument, which operated until April 2010, was a Bruker IFS-120M FTIR spectrometer. In 2013, a Bruker IFS-120/5HR, an upgrade of the IFS-120HR, was installed as a second instrument taking over the observations by the IFS-120M, contributing to the Total Carbon Column Observing Network (TCCON) in addition to the NDACC-IRWG. NDACC MIR measurements covering from 500 to 7500 cm^{-1} are performed with the same settings as the measurements at Syowa Station (see Table 2.3), but no measurements using the NDACC filter #7 and #8. MIR measurements with 2 scans were executed to acquire a spectrum with resolution of 0.0035 cm^{-1}, but sometimes 4 to 16 scans were performed. The spectra, covering long-term periods, have been used for various studies of atmospheric tracers (e.g. O_3, CO, C_2H_6, and HCN) related to stratospheric composition change and biomass burning (Nakajima et al., 1997; Zhao et al., 1997; 2002; Koike et al., 2006; Nagahama and Suzuki, 2007).

In this study, we used the spectra measured with the NDACC optical filter #6 (covering 500–1400 cm^{-1}) and a MCT detector under clear-sky conditions since October 1997.

For the observations with the NDACC filter #6 using the IFS-120/5HR from 2013 up to 2018, unfortunately, the SNR values of the spectra are about 20% of those achieved before the replacement of the instrument because smaller apertures were used. Since February 2019, the more suitable aperture diameter of 1.7 mm has been adopted for the measurements using the NDACC optical filter #6. Hence, the spectra measured in the period between February 2019 and May 2020 were additionally used in the retrievals of HFC-23. Also, these spectra are degraded to 0.0070 cm^{-1} (see Section 3.3).

Chapter 3

Retrieval of atmospheric HFC-23

To derive HFC-23 vertical mole fraction profiles and total column abundances, all spectra taken from the FTIR instruments at Rikubetsu and at Syowa Station were analyzed with the SFIT4 version 0.9.4.4 program (see https://wiki.ucar.edu/display/sfit4/) based on the optimal estimation method (OEM) of Rodgers (Rodgers, 1976; Rodgers, 2000). This program was developed by scientists from the National Center for Atmospheric Research (NCAR), the University of Bremen, and other institutes taking part in the NDACC-IRWG, as an up-grade version of the previous SFIT2 algorithm (Pougatchev et al., 1995). This program includes the procedure which calculates the theoretical absorption spectrum based on prior information (e.g. meteorological profiles, a priori profile of target) and fits the calculated spectrum to the observed one, for selected one or more spectral regions (micro-windows; MWs). Finally, the program derives the most suitable

state vector (i.e. the retrieved target profile) that balances information obtained from observation and from the a priori. Hereafter, the details of HFC-23 retrieval are described.

3.1 Retrieval method

From the Rodgers's OEM, measured spectrum $\boldsymbol{y}$ can be written using a forward model $\boldsymbol{F}$ with a vector vertical profile of gas $\boldsymbol{x}$ and all non-retrieved parameters (temperature, pressure, etc.) vector b as;

$$\boldsymbol{y} = \boldsymbol{F}(\boldsymbol{x},\ \boldsymbol{b}) + \boldsymbol{\varepsilon} \tag{3.1}$$

where $\boldsymbol{\varepsilon}$ is a measurement noise. By taking a Taylor's series expansion around a priori profile x_{a} and best estimated value $\hat{\boldsymbol{b}}$ of $\boldsymbol{b}$, and neglecting higher orders, I get the linear expression of Equation 3.1 as;

$$\begin{aligned} \boldsymbol{y} &= \boldsymbol{F}(\boldsymbol{x_{\mathrm{a}}},\ \hat{\boldsymbol{b}}) + \frac{\partial \boldsymbol{F}}{\partial \boldsymbol{x}}(\boldsymbol{x} - \boldsymbol{x_{\mathrm{a}}}) + \frac{\partial \boldsymbol{F}}{\partial \boldsymbol{b}}(\boldsymbol{b} - \hat{\boldsymbol{b}}) + \boldsymbol{\varepsilon} \\ &= \boldsymbol{y_{\mathrm{a}}} + \boldsymbol{K}(\boldsymbol{x} - \boldsymbol{x_{\mathrm{a}}}) + \boldsymbol{K_{\mathrm{b}}}(\boldsymbol{b} - \hat{\boldsymbol{b}}) + \boldsymbol{\varepsilon} \end{aligned} \tag{3.2}$$

where $\boldsymbol{y_{\mathrm{a}}}$ is a spectrum calculated from a priori, $\boldsymbol{K}$ and $\boldsymbol{K_{\mathrm{b}}}$ are weighting function matrices, which are often so-called Jacobian, for state vector $\boldsymbol{x}$ and model parameter $\boldsymbol{b}$, respectively. From the inversion of Equation 3.2, I get the best estimated vertical profile

of gas mole fraction vector $\hat{\boldsymbol{x}}$ as;

$$\hat{\boldsymbol{x}} = \boldsymbol{x}_{\mathbf{a}} + \boldsymbol{G}\boldsymbol{K}(\boldsymbol{x} - \boldsymbol{x}_{\mathbf{a}}) + \boldsymbol{G}\boldsymbol{K}_{\mathbf{b}}(\boldsymbol{b} - \hat{\boldsymbol{b}}) + \boldsymbol{G}\boldsymbol{\varepsilon} \tag{3.3}$$

where $\boldsymbol{G} = \partial\hat{\boldsymbol{x}}/\partial\boldsymbol{y}$ is a gain matrix, whose line elements are so-called contribution function, which mean inversion sensitivity. Combining a profile $\boldsymbol{x}$ taken from an observed spectrum $\boldsymbol{y}$ with a priori profile as described in Rodgers (1976), if there is a linear relationship of $\boldsymbol{y} = \boldsymbol{K}(\boldsymbol{x}) + \boldsymbol{\varepsilon}$, the best estimation $\hat{\boldsymbol{x}}$ is defined as following weighted average;

$$\begin{aligned} \hat{\boldsymbol{x}} &= (\boldsymbol{S}_{\mathbf{a}}^{-1} + \boldsymbol{K}^T\boldsymbol{S}_{\boldsymbol{\varepsilon}}^{-1}\boldsymbol{K})^{-1}(\boldsymbol{S}_{\mathbf{a}}^{-1}\boldsymbol{x}_{\mathbf{a}} + \boldsymbol{K}^T\boldsymbol{S}_{\boldsymbol{\varepsilon}}^{-1}\boldsymbol{K}\boldsymbol{x}) \\ &= \boldsymbol{x}_{\mathbf{a}} + \hat{\boldsymbol{S}}\boldsymbol{K}^T\boldsymbol{S}_{\boldsymbol{\varepsilon}}^{-1}(\boldsymbol{y} - \boldsymbol{K}\boldsymbol{x}_{\mathbf{a}}) \end{aligned} \tag{3.4}$$

where $\boldsymbol{S}_{\mathbf{a}}$ and $\boldsymbol{S}_{\boldsymbol{\varepsilon}}$ are a priori and measurement noise covariance matrices, respectively,

$$\begin{aligned} \hat{\boldsymbol{S}} &= (\boldsymbol{S}_{\mathbf{a}}^{-1} + \boldsymbol{K}^T\boldsymbol{S}_{\boldsymbol{\varepsilon}}^{-1}\boldsymbol{K})^{-1} \\ &= \boldsymbol{S}_{\mathbf{a}}\boldsymbol{K}^T(\boldsymbol{S}_{\boldsymbol{\varepsilon}} + \boldsymbol{K}\boldsymbol{S}_{\mathbf{a}}\boldsymbol{K}^T)^{-1}\boldsymbol{S}_{\boldsymbol{\varepsilon}}\boldsymbol{K} \end{aligned} \tag{3.5}$$

is a covariance matrix of $\hat{\boldsymbol{x}}$. Comparing the Equation 3.3, which is neglected the error terms of the forward model parameters and the measurement noise, with Equation 3.4, I get the following matrix, so-called averaging kernel matrix $\boldsymbol{A}$;

$$\boldsymbol{A} = \boldsymbol{G}\boldsymbol{K} = \frac{\partial\hat{\boldsymbol{x}}}{\partial\boldsymbol{x}} = \hat{\boldsymbol{S}}\boldsymbol{K}^T\boldsymbol{S}_{\boldsymbol{\varepsilon}}^{-1}\boldsymbol{K} \tag{3.6}$$

which is described in Rogers (2000) in detail. Each line in matrix $\boldsymbol{A}$ is called the averaging kernel, which represents the sensitivity of retrieved value compared to the true value. The sum of diagonal elements of matrix $\boldsymbol{A}$ (trace; tr($\boldsymbol{A}$)) is called degrees of freedom for signal (DOFS), which gives the number of pieces of vertical information.

Since the forward model for FTIR observation is usually non-linear problem, $\hat{\boldsymbol{x}}$ is taken by minimizing the following cost function $\boldsymbol{J}$ derived from Bayes' theorem and Gaussian statistics;

$$\boldsymbol{J}(\boldsymbol{x}) = (\boldsymbol{y} - \boldsymbol{K}\boldsymbol{x})^T \boldsymbol{S}_{\boldsymbol{\varepsilon}}^{-1} (\boldsymbol{y} - \boldsymbol{K}\boldsymbol{x}) + (\boldsymbol{x} - \boldsymbol{x}_{\mathbf{a}})^T \boldsymbol{R} (\boldsymbol{x} - \boldsymbol{x}_{\mathbf{a}}) \tag{3.7}$$

where $\boldsymbol{R} = \boldsymbol{S}_{\mathbf{a}}^{-1}$ is a regularization matrix. The second term of Equation 3.7 is generally called the constraint and it is important for solving stably the state vector $\boldsymbol{x}$. In the case of Rodgers' OEM, the covariance matrix obtained from a realistic variability of target gas is used as the regularization matrix $\boldsymbol{R}$, but I use Tikhonov regularization (Tikhonov, 1963) to set up $\boldsymbol{R}$ in this study. The details about selection of the regularization matrix is described at Section 3.5. Finally, the cost function is minimized by the Gauss-Newton iteration method, so the appropriate profile is found by the iteration which is described as;

$$\boldsymbol{x}_{i+1} = \boldsymbol{x}_{\mathbf{a}} + \boldsymbol{S}_{\mathbf{a}} \boldsymbol{K}_i^T (\boldsymbol{S}_{\boldsymbol{\varepsilon}} + \boldsymbol{K}_i \boldsymbol{S}_{\mathbf{a}} \boldsymbol{K}_i^T)^{-1} [\boldsymbol{y} - \boldsymbol{y}_i + \boldsymbol{K}_i (\boldsymbol{x}_i - \boldsymbol{x}_{\mathbf{a}})] \tag{3.8}$$

where $i = 0,\ 1,\ 2,\ \ldots$ is the iteration counter, $\boldsymbol{K}_i$ is the Jacobian diagnosed at $\boldsymbol{x}_i$, and $\boldsymbol{y}_i = \boldsymbol{F}(\boldsymbol{x}_i)$. If this iterative calculation converges, the best estimate of $\hat{\boldsymbol{x}}$ results.

3.2 Retrieval windows

Table 3.1 summarizes the strategy for the retrieval of HFC-23 executed in this study. For the retrieval of HFC-23 from FTIR spectra, I used the ν_2 and ν_5 vibrational-rotational transition bands of HFC-23 located around 1150 cm^{-1}, which is the same spectral region as the retrieval of ACE-FTS (Harrison et al., 2012). The IR absorption by HFC-23 contributes typically to only about 1% of the atmospheric transmittance of solar IR radiation at ground level (see Figure 3.4). Hence, choice of MWs is critically important for the retrieval from the ground-based measurement. To avoid three strong H_2O absorption lines at 1149.47 cm^{-1}, 1151.54 cm^{-1} and 1152.44 cm^{-1}, I used two MWs as; MW1: 1138.5–1148.0 cm^{-1}, MW2: 1154.0–1160.0 cm^{-1}. Major interfering species in these MWs are O_3, N_2O, CH_4, H_2O, HDO, CCl_2F_2 (CFC-12), $CHClF_2$ (HCFC-22), and $CH_3C(O)OONO_2$ (peroxyacetyl nitrate: PAN). Since there are several strong absorption lines of O_3 and N_2O in these MWs, I retrieve profiles of these gases in addition to HFC-23. For the other species except for CH_4, I fit to an observed spectrum by scaling the a priori profile (column retrieval). In addition, CH_3CCl_2F (HCFC-141b) and CH_3CClF_2 (HCFC-142b) exist as minor interfering gases in the MWs, but these gases were not retrieved in this study because the contributions of these gases to the transmittance in the MWs are very small. More detail is described in the following.

Table 3.1: Summary of retrieval settings used for HFC-23 retrievals.

Micro-windows	MW1	MW2
Spectral region [cm^{-1}]	1138.5–1148.0	1154.0–1160.0
Profile retrieval	HFC-23, N_2O, O_3	
Column retrieval	H_2O, HDO, CFC-12, PAN, HCFC-22	H_2O, HDO, CFC-12, PAN
Pre-retrieval	H_2O, HDO, CH_4	
Fixed species	CH_4, HCFC-141b, HCFC-142b	
Spectroscopic parameters	PLL (HFC-23, CFC-12, PAN, HCFC-22)	
	ATM18 (H_2O, HDO)	
	HITRAN2008 (others)	
Pressure and temperature	NCEP Reanalysis-1, CIRA86	
A priori profiles (HFC-23)	Naik et al. (2000) but scaled to 16 ppt (Rikubetsu) / 24 ppt (Syowa Station) at surface	
A priori profiles (others)	Mean profiles in the period of 1995–2010 (Rikubetsu) / 2007 – 2016 (Syowa Station) from WACCM version 6 (CFC-12, HCFC-22, HCFC-141b, HCFC- 142b) WACCM version 6 mean profiles from 1980 to 2020 (except for the above)	
Signal-to-noise ratio (SNR)	Calculated from each observed spectrum	
Background correction	Slope, Curvature	
Instrumental line shape (ILS)	LINEFIT9/14	

3.3 Spectral correction and instrumental line shape

As stated in Section 2.8, absorption spectra which include HFC-23 retrieval MWs were recorded with the NDACC #6 and #8 optical filters in the MCT channel with 0.0035 cm^{-1} resolution. In order to reduce the spectral random noise, I degraded the spectral resolution from 0.0035 cm^{-1} to 0.0070 cm^{-1}. Note that the zero-level of the measured spectra (see Figure 3.1) are raised (in maximum, about +5% relative to maximum signal intensity) and curved due to the non-linearity of the MCT detector. Therefore, I corrected this zero-level offset in measurement spectrum with second order polynomial fitting using well-known absorption saturated bands sprinkled over the spectral region between 750–1350 cm^{-1}.

On the other hand, the continuum level, which is equal to 100% in transmittance, was fitted by the following, because the shape of the continuum level is caused by the optical characterization of the FTIR instrument, especially the optical bandpass filter. Since the MWs for HFC-23 retrieval are rather wide, the slope and curvature (parabola) of the spectral continuum level over each MWs are retrieved in the SFIT4 program. This correction multiplies the transmission spectrum $\boldsymbol{B}$ by;

$$\boldsymbol{B} = \alpha(\boldsymbol{w} - w_0)^2 + \beta(\boldsymbol{w} - w_0) + 1 \tag{3.9}$$

where α is the curvature, β is the slope factor, $\boldsymbol{w}$ is the wavenumber vector in the MW, and w_0 is the starting wavenumber of the MW. As a result, calculated spectrum $\boldsymbol{y}_c$ can

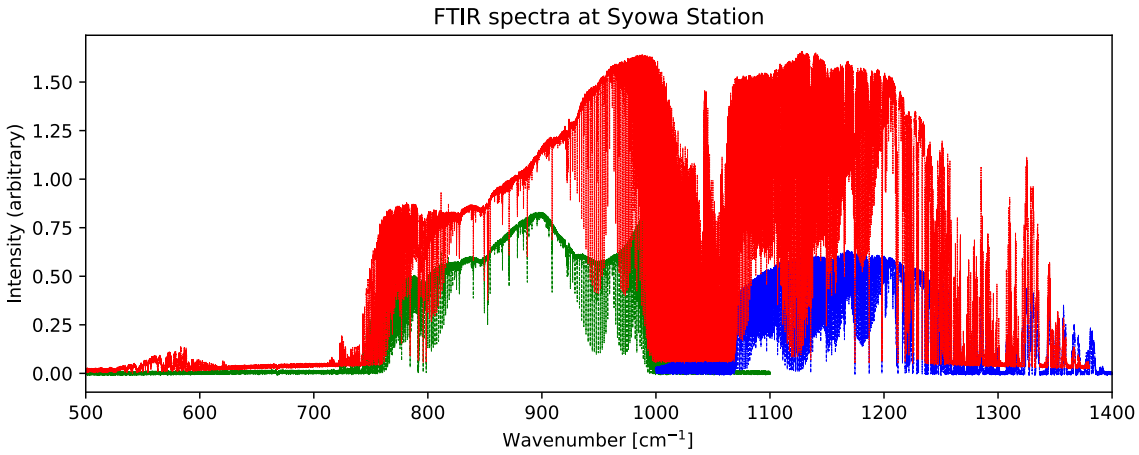

Figure 3.1: Examples of solar absorption spectra taken from FTIR observations at Syowa Station. The red spectrum was obtained with the filter #6 on 30 September 2007. The green and the blue ones were measured with filter #7 and #8 on 30 September 2011, respectively. A positive zero-level offset is clearly seen on the red filter #6 spectrum.

be written as;

$$\boldsymbol{y}_{\mathrm{c}} = \boldsymbol{B} \cdot \boldsymbol{\psi}[\boldsymbol{\tau}(\boldsymbol{w})] \tag{3.10}$$

where $\boldsymbol{\tau}(\boldsymbol{w})$ is a calculated transmission spectrum with absorptions by each gas and solar lines (the Fraunhofer lines), $\boldsymbol{\psi}[\boldsymbol{\tau}(\boldsymbol{w})]$ is a transmission spectrum of $\boldsymbol{\tau}(\boldsymbol{w})$ convolved with instrumental line shape (ILS) function.

Hydrogen bromide (HBr) gas-cell spectra were taken using a MIR internal light source in order to check the alignment of the FTIR instrument and to evaluate the ILS function for both the instruments at Rikubetsu and Syowa Station. At Rikubetsu, the first HBr cell spectrum was taken at 26 March 2002 after the relocation of the instrument in

October 1997. In this study, all observed spectra from October 1997 to April 2010 with the IFS-120M instrument were convolved with the ILS function derived from the HBr cell measurement, but for all observed spectra with the IFS-120/5HR instrument no ILS function was used because the instrument has always been maintained best optical alignment. At Syowa Station, HBr cell spectra were taken from time to time following installation and re-alignment. Therefore, ILS corrections were applied for all the spectra. The modulation efficiency and phase error of the ILS at Rikubetsu and Syowa Station were evaluated with LINEFIT9 and LINEFIT14 programs, respectively (Hase et al., 1999).

3.4 Spectroscopic parameters

For the calculation of absorption by each atmospheric chemical species, the HITRAN 2008 line-by-line spectroscopic database (Rothman et al., 2009) was primarily used. For spectroscopic parameters for H_2O and its isotopes, the updated ATM18 line-list by one of us (G. C. Toon, NASA/JPL) was used (For detail, see `https://mark4sun.jpl.nasa.gov/toon/atm18/atm18.html`). For heavy molecules (such as CFCs, HCFCs, HFCs, and PAN), there are no resolved line-lists available by HITRAN 2008. For our retrieval of CFC-12, HCFC-22, HFC-23, and PAN, I used pseudo-line-list (PLL) developed by G. C. Toon (For detail, see `https://mark4sun.jpl.nasa.gov/pseudo.html`). In these PLLs, the 296 K line strength and ground-state energy (E'') for each pseudo line were empirically reproduced by fitting transmittance laboratory spectra (absorption cross sections)

acquired under various temperature and pressure conditions. In Harrison et al. (2012), the PLL of HFC-23 obtained from the cross sections acquired with a resolution of 0.02 cm^{-1} and a temperature range of 214–300 K and a total pressure range of 0.184–253 Torr by Chung (2005) were used to analyze solar occultation spectra, but there was a large systematic bias of approximately 30% in the retrieved profiles. This is dominantly caused by the poor quality of the used cross section dataset (e.g. inconsistency between the spectral absorptions and the temperature-pressure-mole fraction conditions). In order to reduce the systematic uncertainty in the HFC-23 PLL, Harrison (2013) reported new absorption cross section measurements with a resolution of 0.015 cm^{-1}, which cover a wider spectral range of 950–1500 cm^{-1} and more realistic atmospheric conditions in the troposphere and the stratosphere (i.e. a wider temperature range of 188–294 K and a wider pressure range of 23–762 Torr.)

For the current study, a new HFC-23 PLL was used with a wavenumber interval of 0.004 cm^{-1} over a spectral range of 1105–1425 cm^{-1} (`https://mark4sun.jpl.nasa.gov/data/spec/Pseudo/CHF3_PLL_Update.pdf`). In addition to the Chung's laboratory spectra, this pseudo-line parameters were obtained from re-fitting Harrison's 2013 laboratory spectra, three spectra from the Pacific Northwest National Laboratory (PNNL) IR database (Sharpe et al., 2004), and one spectrum from Gohar et al. (2004). Using this new PLL, which is dominated by the Harrison 2013 data, the bias in MkIV balloon measurements of HFC-23 is eliminated. In the forward model, the absorption line intensities are calculated by assuming the Boltzmann distribution which includes the temperature

dependences of rotational/vibrational partition functions and induced emission. For the rotational partition function, its temperature dependence is calculated from $(296/T)^j$, where T is temperature and j is temperature coefficient. For HFC-23, j was set to 1.5, the normal value for non-linear molecules. To calculate the vibrational partition function, I assumed a harmonic oscillator approximation and used the fundamental vibrational frequencies and degeneracies from Ceausu-Velcescu et al. (2003). For solar lines, I used the empirical line-by-line parameters in MIR region (Hase et al. 2006), which is in the SFIT4 program package.

3.5 Information of atmospheric state and regularization matrix

I consider 47 atmospheric layers for Rikubetsu, and 48 layers for Syowa Station from ground to 120 km in altitude. The thickness of the layers increases with height. I used Reanalysis-1 daily temperature and pressure data by National Center for Environmental Prediction (NCEP; `http://www.ncep.noaa.gov`) from the ground to 40 km, and zonal monthly-mean climatological profiles by the COSPAR International Reference Atmosphere 1986 (CIRA-86) from 40 km to 120 km (Rees et al., 1990). For a priori profiles of atmospheric compositions, the averaged profiles in the period of 1980–2020 derived from the monthly-mean profile data computed by the Whole Atmospheric Community Climate Model (WACCM) version 6 (Chang et al., 2008) were basically used.

For HFC-23, the WACCM does not compute its profile and thus a priori profile of HFC-23 was based on globally and annually mean mole fraction profile by two-dimensional chemistry-radiation-transport model by Naik et al. (2000). This a priori profile shows little decrease above the tropopause, reflecting a very long lifetime (228 years) of HFC-23 in the atmosphere (Montzka et al., 2019). For Rikubetsu, the HFC-23 a priori profile was scaled to 16 ppt at ground, which corresponds to the mole fraction of HFC-23 in 2002 in the northern hemisphere. For Syowa Station, the HFC-23 a priori profile was scaled to 24 ppt at ground, which corresponds to the mole fraction of HFC-23 in 2011 in the southern hemisphere.

For CFC-12, HCFC-22, HCFC-141b, and HCFC-142b, the mean profiles for 1995–2010 at Rikubetsu and for 2007–2016 at Syowa Station derived from the WACCM monthly dataset were used, because these species in the atmosphere have dramatically increased since 1980. Note that the mean profiles of HCFC-141b and HCFC-142b were used as fixed profiles in the HFC-23 retrieval.

For H_2O, HDO, and CH_4, a priori profiles were preliminarily retrieved (pre-retrieved) using other independent MWs, because these profiles may induce large uncertainties in the HFC-23 retrieval. The detailed pre-retrieval procedure is described in the following section.

In retrieval of atmospheric profile, it is crucial to select an optimal regularization matrix as a constraint on the a priori profile, because the regularization matrix affects the vertical resolution and the retrieval error. In the case of the general OEM, the regular-

ization matrix $\boldsymbol{R}$ is the inverse of the a priori covariance matrix $\boldsymbol{S_a}$ which represents the natural variability for the target. To calculate $\boldsymbol{S_a}$, the climatological dataset, which is constructed by a large number of independent profiles, should be used. For O_3, this is available because there are several high frequency observations (e.g. balloon-borne sondes, satellite measurements). In many cases, however, it is difficult to calculate a realistic natural variability for a priori profile, and our target gas also is one of them. Therefore, Sa is set up by an *ad hoc* method. In this study, Tikhonov regularization (Tikhonov, 1963) was used as in the previous studies of Sussman et al. (2009) for water vapor and Vigouroux et al. (2009) for formaldehyde (HCHO), and the regularization matrix is defined as:

$$\boldsymbol{R} = \alpha \boldsymbol{L}^T \boldsymbol{L} \tag{3.11}$$

where α is the strength parameter of the constraint and $\boldsymbol{L}$ is a discrete derivative operator. I used the discrete first-order derivative operator $\boldsymbol{L}_1$ as $\boldsymbol{L}$:

$$\boldsymbol{L}_1 = \begin{pmatrix} -1 & 1 & 0 & \dots & 0 \\ 0 & -1 & 1 & \ddots & \vdots \\ \vdots & \ddots & \ddots & \ddots & 0 \\ 0 & \dots & 0 & -1 & 1 \end{pmatrix}. \tag{3.12}$$

The operator respects the vertical shape of the a priori profile and suppresses oscillation of the retrieved profile. I have to properly determine the value of the regularization

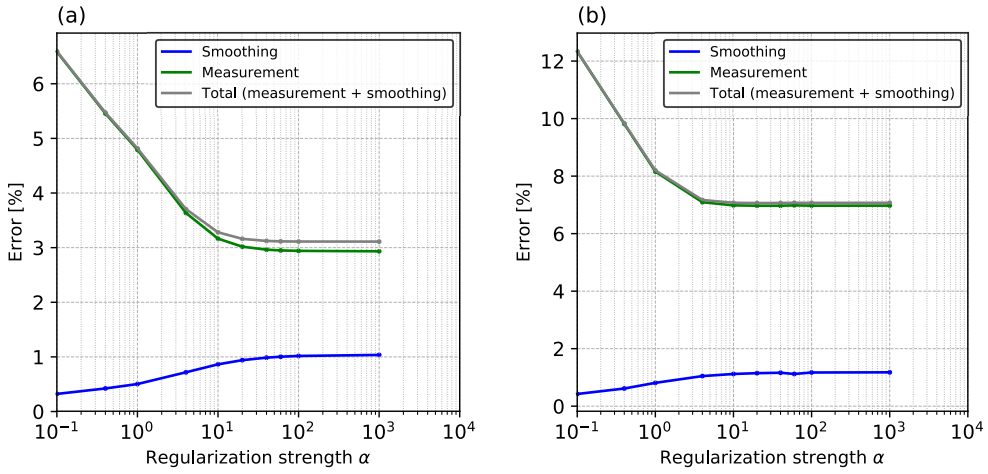

Figure 3.2: Determinations of the α parameters for the observations at Rikubetsu at 1:36 UTC on 6 January 2005 (a) and at 5:59 UTC on 12 July 2005 (b).

parameter α, which is tuned to balance the constraint on the a priori profile and the residual between the measured and the calculated spectra, so-called the L-curve method (Hansen, 1992). In this study, I were tuning α following the alternative method described in Section 4.D of Steck (2002). This method can determine the optimal α to minimize the total retrieval error (the smoothing plus the measurement errors; for details, see in Section 3.8). Figure 3.2 shows the determinations of the α parameters for the observations at Rikubetsu on 6 January 2005 (a) and on 12 July 2005 (b). In the case of Figure 3.2 (a), the total retrieval error is minimum at $\alpha = \sim 100$. However, in the case of Figure 3.2 (b), the total error is minimum at $\alpha = \sim 20$ and flat in larger than it. In this study, I used $\alpha = 100$ for all retrievals at Rikubetsu and Syowa Station.

According to Equation 3.7, I can understand that the measurement noise covariance matrix $\boldsymbol{S_\varepsilon}$ is also a key constraint that balances the observations against the regularization matrix. The real SNR of the measured spectrum is an indicator of the noise level for each spectrum, but for each retrieval the *ad hoc* SNR is used to determine $\boldsymbol{S_\varepsilon}$. The *ad hoc* SNR is defined as the inverse of the root-mean-square (RMS) value of the residuals in a spectral fit (referred to as the fitted residuals). The *ad hoc* SNR is smaller than the real one since the fitted residuals are caused by various imperfections in forward model parameters (e.g. spectroscopic data, temperature profile, ILS) in addition to simple measurement noise. It is assumed that $\boldsymbol{S_\varepsilon}$ is a diagonal matrix, and I put

$$\mathrm{SNR}^{-2} = (\boldsymbol{y_m} - \boldsymbol{y_c})^T(\boldsymbol{y_m} - \boldsymbol{y_c})/N \tag{3.13}$$

in the diagonal elements of $\boldsymbol{S_\varepsilon}$, where $\boldsymbol{y_m}$ and $\boldsymbol{y_c}$ are the measured and the calculated spectrum, respectively, and N is the number of spectral points.

Table 3.2: Windows used for the pre-retrievals of H_2O, HDO, and CH_4. Profile-retrieved species are in bold characters.

Target species	Micro-windows [cm^{-1}]	Interfering species	References
H_2O	824.40–825.90	**O_3**, CO_2, C_2H_6	Meier et al. (2004)
HDO	1208.40–1209.10	CH_4, N_2O, H_2O, CO_2, O_3, HNO_3, COF_2	Vigouroux et al. (2012)
CH_4	1201.820–1202.605	**N_2O**, H_2O, O_3, HNO_3	Meier et al. (2004)

3.6 Pre-retrievals for H_2O, HDO, and CH_4

The vertical gradient and spatial-temporal variability of water vapor in the atmosphere are very large. In many cases with ground-based FTIR observations, it is impossible to choose the retrieval MWs without absorption structures of water vapor and its isotopes, and thus it is important to use accurate water vapor profiles that are coincident with the location and time of each observation. Many previous studies (Vigouroux et al., 2009; 2012; Ortega et al., 2019) used the pre-retrieved H_2O (and/or HDO) profiles using the dedicated MWs in order to reduce their interference errors. In this study, a priori profiles of H_2O and HDO were acquired by pre-retrievals using the different MWs shown in Table 3.2.

H_2O profiles were retrieved by using the MW of 824.40–825.90 cm^{-1} which has been shown in the Atlas (Meier et al., 2004) and the monthly profiles derived from the WACCM version 6 in the period of 1980–2020 as a priori profile for each spectrum. Since an H_2O absorption line having E'' of 586.48 cm^{-1} is in the MW, we assume that the uncertainties

of the retrieved H_2O profiles caused by temperature dependence of line strength are small. The H_2O line is relatively weak and is hardly ever saturated, even when the humidity at Rikubetsu is high in summer. For HDO, the profile was pre-retrieved using the MW of 1208.40–1209.10 cm^{-1}, and the pre-retrieved H_2O profile shape was used as a priori profile shapes of HDO and H_2O. This HDO MW was used in the study of Vigouroux et al. (2012), but our MW is slightly wider than the previous study because the DOFS for HDO was increased when the wider window used. We estimated the retrieval uncertainties of approximately 10% for the pre-retrieved total columns of H_2O and HDO, which were mainly due to the systematic uncertainties of the spectroscopic parameters based on the HITRAN 2008.

It is important in deriving the HFC-23 retrieval that the interfering CH_4 profile is pre-retrieved with the dedicated MW shown in Table 2 because the weak CH_4 absorption structure in the retrieval MWs of HFC-23 could disturb estimation of the true condition of HFC-23. Figure 3.3 shows the time-series of the total columns of HFC-23 and CH_4 retrieved from the FTIR spectra observed at Syowa Station in 2007 and their scatter plot. The HFC-23 total column amounts (red-x plots) derived from retrievals of HFC-23 accompanied by column-retrieval (scaling) of CH_4 profile, and the scaled CH_4 total columns (green-x plots) are presented in Figure 3.3 (a). There is an anti-correlation between these two time-series. Since the typical seasonal cycle of CH_4 shows a minimum in summer due to destruction by the OH radical, the seasonal cycle of the scaled CH_4 total columns in the retrievals is inconsistent with the expected cycle. Furthermore, a

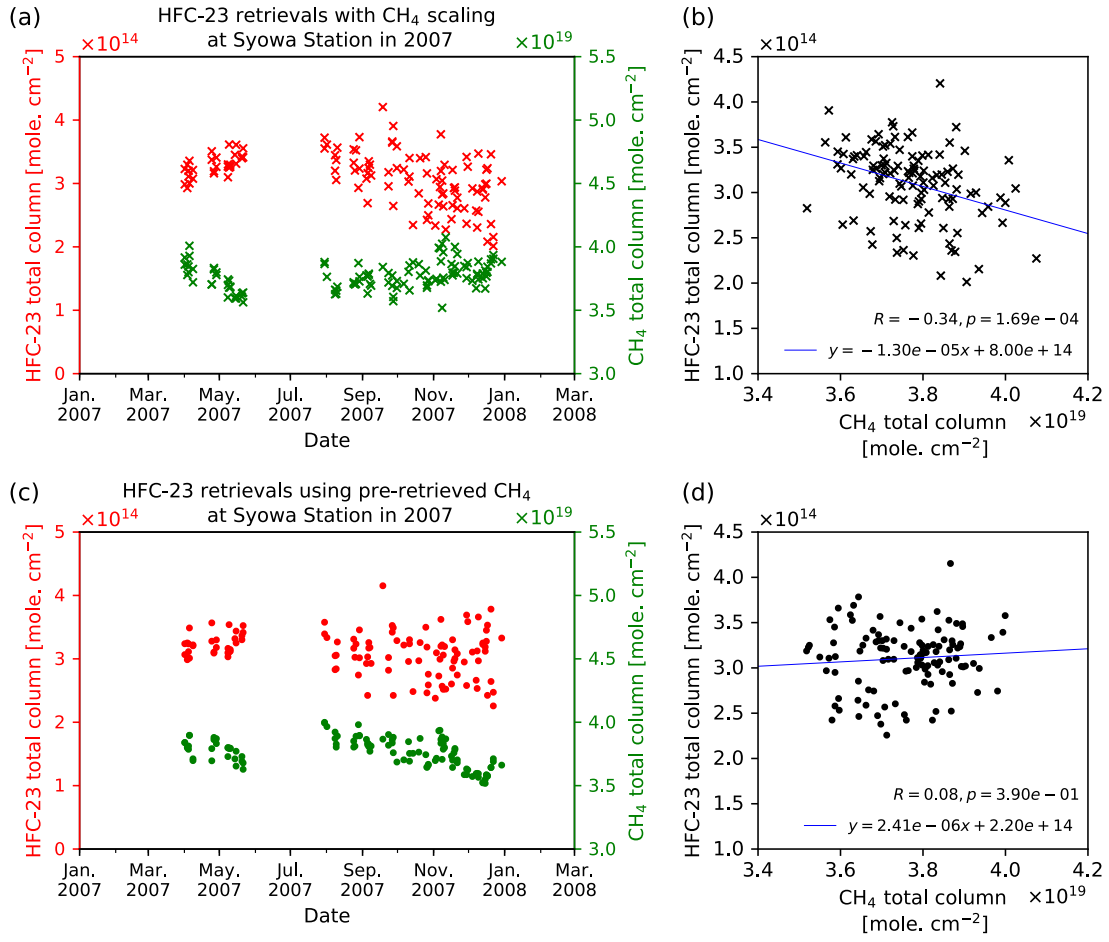

Figure 3.3: Time-series of the total columns of HFC-23 and CH_4 retrieved from FTIR spectra observed at Syowa Station in 2007. (a) HFC-23 total columns (red-x plots) derived from HFC-23 retrievals accompanied by column-retrieval (scaling) of CH_4 profile, and the scaled CH_4 total columns (green-x plots). (b) The correlation between HFC-23 and CH_4 of (a). (c) Independent retrieved CH_4 total columns using a spectral region from 1201.820 to 1202.605 cm^{-1} (green dots), and HFC-23 total columns from retrievals using the independent retrieved CH_4 profiles as fixed profiles (red dots). (d) The correlation between HFC-23 and CH_4 of (c). Note that these retrieved HFC-23 columns were selected by the threshold of the fitted RMS value depending on the value of solar zenith angle (SZA): the threshold of the fitted RMS are $< 0.5\%$ for SZA $<$ 85o and $< 1.5\%$ for SZA of 85% or greater.

seasonal cycle in the HFC-23 total columns is observed, but this is not expected since the atmospheric lifetime of HFC-23 is very long and thus its variability due to atmospheric loss is very small. Figure 3.3 (b) shows that the scatter plot of the total columns of HFC-23 and CH_4 in Figure 3.3 (a). Examination by a two-side hypothesis testing with Student's t-distribution under a null hypothesis in which there is no correlation between these total columns, the anti-correlation between HFC-23 and CH_4 is statistically significant with a significance level of 5% (p-value < 0.05). Figure 3.3 (c) shows the time-series of the independent retrieved CH_4 total columns using a spectral region from 1201.820 to 1202.605 cm^{-1} from Meier et al. (2004) (green dots), and of the HFC-23 total columns from retrievals using the independent retrieved CH_4 profiles (CH_4-fixed retrievals; red dots). In contrast to the scaled CH_4 in Figure 3.3 (a), the independently retrieved CH_4 shows the expected seasonal cycle. As the result, there is no un-realistic cycle in the HFC-23 total columns analyzed by the CH_4-fixed retrievals. As can be seen in the scatter plot of Figure 3.3 (d), there is no correlation between HFC-23 and interfering CH_4. Therefore, we decided to pre-retrieve the CH_4 profile with the independent window before the retrieval of HFC-23. For pre-retrieving the profile of CH_4, we used the mean CH_4 profile (1980–2020) derived from the WACCM and the pre-retrieved H_2O profiles mentioned above. In conclusion, the pre-retrieved profiles of H_2O, HDO, and CH_4 were used as a priori profiles (H_2O and HDO) and fixed profile (CH_4) in the subsequent retrieval of HFC-23.

3.7 Results of HFC-23 retrievals

Figure 3.4 shows an example of a spectral fitting result for the two MWs (MW1 and MW2) for HFC-23. This typical fitting was for a spectrum observed by the IFS-120M FTIR spectrometer at Syowa Station on 9 November 2011 at 13:47 UTC with a solar zenith angle (SZA) of 67.3°. In this case, the absorption contribution of HFC-23 is about 1% relative to the total transmittance around 1156 cm^{-1}, corresponding to a total column of 3.85×10^{14} molecules cm^{-2}. The typical root-mean-square (RMS) of the fitted residual (observed minus calculated spectrum) is 0.34%.

A summary of all the HFC-23 retrievals with SFIT4 at Rikubetsu and Syowa Station is shown in Table 3.3. The retrievals at Rikubetsu are summarized for the periods of 1997–2010 and 2019–2020 due to use of different instruments. The retrievals without negative values in profile were counted into the number of observations as the "valid" number, and those results were used to calculate each statistic. About 6% of observations at Rikubetsu in 1997–2010 were rejected. On the other hand, almost all of observations at Rikubetsu in 2019–2020 and at Syowa Station were used. The mean RMS of the fitted residuals with the one standard deviation (1σ) at Rikubetsu is $0.35 \pm 0.14\%$ and $0.27 \pm 0.03\%$ for the 1997–2010 and 2019–2020, respectively. The mean RMS with 1σ at Syowa Station is $0.43 \pm 0.38\%$. The mean HFC-23 total column with 1σ standard deviation at Rikubetsu increased from $(3.23 \pm 1.10) \times 10^{14}$ molecules cm^{-2} in the 1997–2010 period to $(5.59 \pm 0.43) \times 10^{14}$ molecules cm^{-2} in the 2019–2020 period due to the increase of

atmospheric HFC-23.

As mentioned in Section 3.1, the vertical information content of the FTIR retrievals is characterized by the averaging kernel matrix $\boldsymbol{A}$, defined by Equation 3.5. Figure 3.5 shows typical averaging kernels of the HFC-23 retrieval for the same spectrum shown in Figure 3.4. Each curve coloured according to the right colour-bar in Figure 3.5 represents the row value of the averaging kernel matrix on the corresponding vertical layer. All the retrievals, including the typical case in Figure 3.5, are sensitive to troposphere and lower stratosphere, having a sensitivity peak in averaging kernel at about 4 km. The full widths at half maximum of the averaging kernels are about 20 km, and the mean DOFS for both all retrievals at Rikubetsu and Syowa Station is approximately 1.0. We conclude that only one piece of vertical information (the total column) can be extracted in this study.

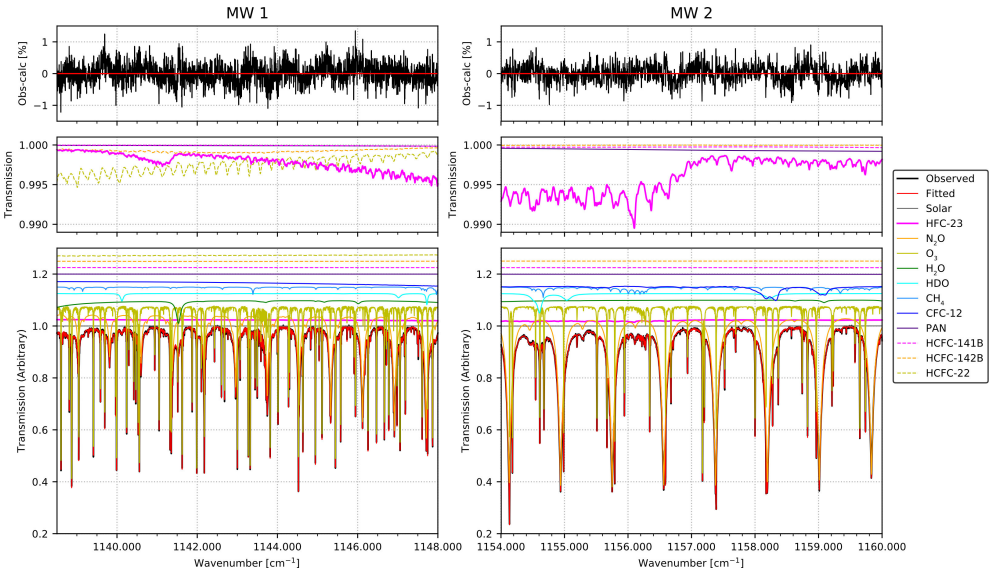

Figure 3.4: Typical spectral simulation results of the two HFC-23 retrieval micro-windows (left panel: MW1; right panel: MW2) fitted to the observed spectrum at Syowa Station on 9 November 2011 at 13:47 UTC. The top two panels show the residuals (observed minus calculated) of the fittings for MW1 and MW2. The middle two panels show the absorption contributions of HFC-23, PAN, HCFC-141b, HCFC-142b, and HCFC-22 in MW1 and MW2. The bottom two panels show the individual contributions from each interfering species, shifted by multiples of 0.025 for clarity, except the observed and the calculated lines.

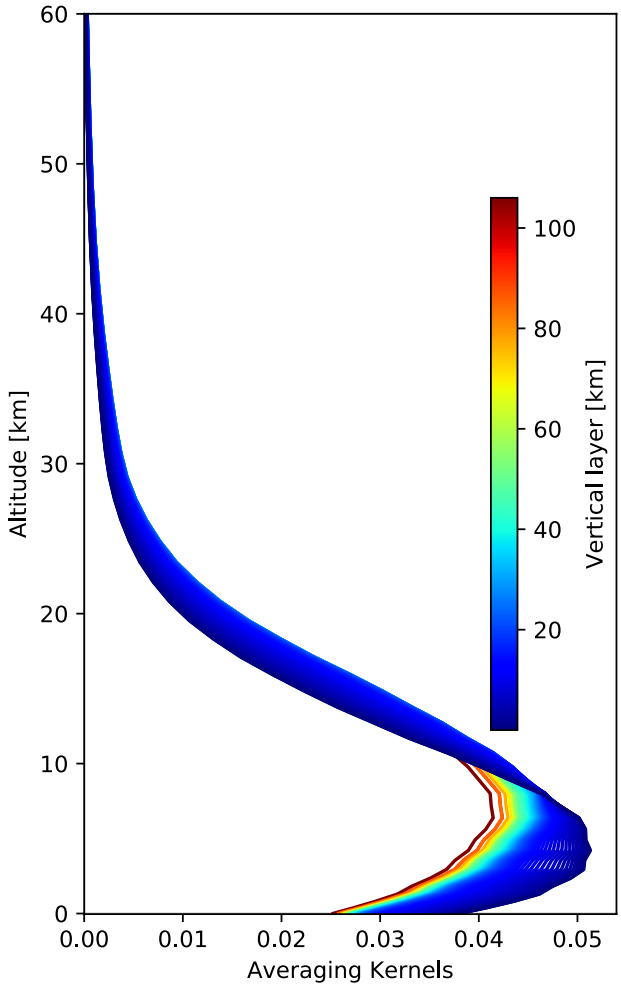

Figure 3.5: Typical averaging kernels of the HFC-23 retrieval for the same spectrum shown in Figure 3, which are normalized using the a priori profile. Note that the vertical scale is from surface up to 60 km because there is almost no sensitivity above 60 km.

Table 3.3: Statistic summary of the fitted SNRs, the root-mean-squares (RMSs) of the fitted residuals (observed minus calculated spectrum), the degree of freedom for signals (DOFSs) and the retrieved HFC-23 total columns at Rikubetsu and Syowa Station. The errors of the fitted RMSs, the DOFSs, and the total columns are the one standard deviation (1σ) around the averages. The numbers of the HFC-23 retrievals (N) are divided into two parts of a number of the retrievals used in this analysis (valid) and of total ones including rejected ones (total).

Site (instrument)	Period	N (valid / total)	Mean fitted SNR (MW1 / MW2)	Mean fitted RMS [%]	Mean DOFS	Mean HFC-23 total column [10^{14} molecules cm^{-2}]
Rikubetsu (IFS-120M)	1997–2010	1081/1152	293/371	0.35 ± 0.14	1.0 ± 0.02	3.23 ± 1.10
Rikubetsu (IFS-120/5HR)	2019–2020	30/30	350/414	0.27 ± 0.03	1.0 ± 0.01	5.59 ± 0.43
Syowa Station (IFS-120M)	2007–2016	206/207	294/308	0.43 ± 0.38	1.0 ± 0.03	3.69 ± 1.35

3.8 Error analysis

The retrieval error can be considered as the difference between the retrieved and the true state vector. Subtract the true state vector $\boldsymbol{x}$ from Equation 3.3 including the systematic forward model error $\boldsymbol{\varepsilon_f}$, the difference is defined as the following equation:

$$\hat{\boldsymbol{x}} - \boldsymbol{x} = (\boldsymbol{A} - \boldsymbol{I})(\boldsymbol{x} - \boldsymbol{x_a}) + \boldsymbol{G}\boldsymbol{K_b}\boldsymbol{\varepsilon_b} + \boldsymbol{G}\boldsymbol{\varepsilon_f} + \boldsymbol{G}\boldsymbol{\varepsilon} \tag{3.14}$$

where $\boldsymbol{I}$ is an identity matrix and $\boldsymbol{\varepsilon_b} = \boldsymbol{b} - \hat{\boldsymbol{b}}$ (Rodgers, 1990; 2000). The retrieval error consists of four parts: the smoothing error $(\boldsymbol{A} - \boldsymbol{I})(\boldsymbol{x} - \boldsymbol{x_a})$, the non-retrieved forward model parameter error $\boldsymbol{G}\boldsymbol{K_b}\boldsymbol{\varepsilon_b}$, the forward model error $\boldsymbol{G}\boldsymbol{\varepsilon_f}$ and the measurement noise $\boldsymbol{G}\boldsymbol{\varepsilon}$. The smoothing error is caused by the lack of vertical sensitivity combined with uncertainty in $\boldsymbol{x_a}$ and includes the uncertainties from target gas, interfering gases and any other retrieved parameters (e.g. background correction parameters). The forward model parameter error $\boldsymbol{G}\boldsymbol{K_b}\boldsymbol{\varepsilon_b}$ comes from the uncertainties of the parameters (e.g. profiles of temperature and pressure, line lists of target and interfering gases, SZA, etc.) that are used for the forward model calculation. The forward model error is from the uncertainty in the forward model itself relative to true physics. In this study, the forward model error was ignored, because the physical process (radiation transfer, IR absorption, etc.) in the SFIT4 algorithm has been established well in previous studies.

The smoothing random error from target gas profile retrieval is described by the

covariance matrix

$$\boldsymbol{S}_{\mathbf{s,Tar}} = (\boldsymbol{A}_{\mathbf{Tar}} - \boldsymbol{I})\boldsymbol{S}_{\mathbf{a,Tar}}(\boldsymbol{A}_{\mathbf{Tar}} - \boldsymbol{I})^T, \tag{3.15}$$

where $\boldsymbol{A}_{\mathbf{Tar}}$ is a part of the full averaging kernel matrix $\boldsymbol{A}$ where the row and column elements run over all target components, $\boldsymbol{S}_{\mathbf{a,Tar}}$ is the a priori covariance matrix. In general, $\boldsymbol{S}_{\mathbf{a,Tar}}$ should represent the natural variability of the target gas, but we don't know well the natural variability of HFC-23 profile due to the lack of vertically measurement data. Therefore, a variability matrix derived from the AGAGE in-situ/sampling measurement dataset was used at each site as a substitute of $\boldsymbol{S}_{\mathbf{a,Tar}}$. For Rikubetsu, the variability of 25% against the a priori profile (square of $0.25\boldsymbol{x}_{\mathbf{a}}$) based on the background air sampling data at Cape Grim in the period of 1995–2009 (Simmonds et al., 2018b) was adopted to the diagonal elements of the variability matrix. For Syowa Station, the variability of 10% against the a priori profile (square of $0.10\boldsymbol{x}_{\mathbf{a}}$) computed from the non-polluted data of the AGAGE in-situ measurements at Cape Grim (`https://agage2.eas.gatech.edu/data_archive/agage/gc-ms-medusa/complete/tasmania/`) was set to the diagonal elements of the matrix. Note that the systematic uncertainty for the smoothing error was not considered because we assumed that the shape of the HFC-23 a priori profile does not have a large altitudinal gradient as mentioned in Section 3.5. The smoothing random errors for the retrieval uncertainties from all interfering species and some other retrieval parameters (background slope and curvature correction, wavenumber shift, solar line shift, solar line

strength, and simple phase correction) can be written by:

$$\boldsymbol{\varepsilon}_{\mathbf{ret}} = \boldsymbol{A}_{\mathbf{Tar,Int}}(\boldsymbol{x}_{\mathbf{t}}^{\mathbf{Int}} - \boldsymbol{x}_{\mathbf{a}}^{\mathbf{Int}}) + \boldsymbol{A}_{\mathbf{Tar,Oth}}(\boldsymbol{x}_{\mathbf{t}}^{\mathbf{Oth}} - \boldsymbol{x}_{\mathbf{a}}^{\mathbf{Oth}}), \tag{3.16}$$

where $\boldsymbol{A}_{\mathbf{Tar,Int}}$ is a part of the full averaging kernel matrix $\boldsymbol{A}$ where the row elements run over all target components and the column elements run over all interfering species; $\boldsymbol{A}_{\mathbf{Tar,Oth}}$ is a part of the $\boldsymbol{A}$ matrix where the row and column elements run over all target and other parameter components, respectively; $\boldsymbol{x}_{\mathbf{t}}^{\mathbf{Int}}$ and $\boldsymbol{x}_{\mathbf{a}}^{\mathbf{Int}}$, $\boldsymbol{x}_{\mathbf{t}}^{\mathbf{Oth}}$ and $\boldsymbol{x}_{\mathbf{a}}^{\mathbf{Oth}}$ are the true and a priori state vectors of interfering species and other parameters, respectively. To estimate the retrieval errors from the interfering gases, the variabilities around the a priori profiles for H_2O (HDO) were set to 10% and the ones for other species were set to the values calculated from the used WACCM datasets.

In order to estimate the non-retrieved forward model parameter error, the following covariance matrix $\boldsymbol{S}_{\mathbf{f}}$ is calculated:

$$\boldsymbol{S}_{\mathbf{f}} = (\boldsymbol{G}\boldsymbol{K}_{\mathbf{b}})\boldsymbol{S}_{\mathbf{b}}(\boldsymbol{G}\boldsymbol{K}_{\mathbf{b}})^T, \tag{3.17}$$

where $\boldsymbol{S}_{\mathbf{f}}$ is the model parameter covariance matrix, which is from the uncertainties in the model parameters. For the random and systematic uncertainties of temperature at Rikubetsu and Syowa Station, the uncertainties on the NCEP temperature profiles were assumed. The uncertainty of temperature at Rikubetsu is about 2 K in the troposphere,

2–10 K between the tropopause and 60 km, and 10 K above 60 km. The uncertainty of temperature at Syowa Station is about 2.5 K in the altitude range from the surface to 20 km, 2.5–10 K between 20 and 60 km, and 10 K above 60 km. The SZA random uncertainty was assumed an uncertainty of 0.15°, considering measurement time. For HFC-23, N_2O, O_3, H_2O, and HDO, the uncertainties of the spectroscopic parameters (i.e. line intensity, S_ν; air-broadening coefficient, $\gamma_{\rm air}$; temperature dependence coefficient for $\gamma_{\rm air}$, $n_{\rm air}$) were also estimated. For the uncertainties of S_ν, $\gamma_{\rm air}$, and $n_{\rm air}$ of HFC-23, we set 10%, 15%, and 15%, respectively, based on the PLL database (see `https://mark4sun.jpl.nasa.gov/data/spec/Pseudo/CHF3_PLL_Update.pdf`). With regard to heavy molecules like HFC-23, ground state energy E'' values, which are relevant to the temperature dependency of S_ν, is empirically given, and then their uncertainties are larger than light molecules (e.g. H_2O, O_3). In addition, the E'' uncertainty more affects S_ν at a cold site like Syowa Station. We assumed the error of 50 $\rm cm^{-1}$ for the E'' values of the HFC-23 PLL, and estimated the uncertainties of 10% and 15% at Rikubetsu and Syowa Station, respectively, as the effect of the E'' error to S_ν. For N_2O, O_3, H_2O and HDO, the spectroscopic uncertainties were derived from the HITRAN 2008 database. The uncertainties for N_2O and O_3 were set with 5%, 10%, and 5% for S_ν, $\gamma_{\rm air}$, and $n_{\rm air}$, respectively. For H_2O and HDO, we gave the uncertainty of 10% to each parameter.

The measurement error was calculated by the error covariance matrix $\boldsymbol{S}_{\mathbf{n}}$ defined as:

$$\boldsymbol{S}_{\mathbf{n}} = \boldsymbol{G}\boldsymbol{S}_{\boldsymbol{\varepsilon}}\boldsymbol{G}^T, \tag{3.18}$$

where $\boldsymbol{S_n}$ is the measurement noise covariance matrix. We adopted the square inverse of the *ad hoc* SNR for the diagonal elements of $\boldsymbol{S_\varepsilon}$; as mentioned in Section 3.5.

Furthermore, we estimated the impact of the interfering CH_4 to the HFC-23 retrieval because the retrieved HFC-23 total column is affected by the retrieval uncertainty of the pre-fitted CH_4 profile. The uncertainties of the pre-retrieved CH_4 total columns are dominantly caused by the systematic uncertainties of its spectroscopic parameters. Considering the spectroscopic parameter uncertainty provided by the HITRAN2008 database, the mean uncertainties of S_ν, $\gamma_{\rm air}$, and $n_{\rm air}$ on the pre-retrieved CH_4 total columns were approximately 5%, 4%, and 1%, respectively, at both sites. Since the MW for CH_4 pre-retrieval is closed to the HFC-23 MWs, these spectroscopic uncertainties on CH_4 are partly cancelled between both MWs. Therefore, we assumed that the uncertainties of S_ν, $\gamma_{\rm air}$, and $n_{\rm air}$ for CH_4 are 3%, 3%, and 1%, respectively, in the HFC-23 MWs. The effects of the CH_4 systematic uncertainties to the retrieved HFC-23 total column were calculated from Equation 3.17 using these uncertainties. On the other hand, the effect of the CH_4 random uncertainty to the retrieved HFC-23 was derived from the 1σ variability on the pre-retrieved CH_4 total columns. The 1σ standard deviations at Rikubetsu and Syowa Station were 4% and 3%, respectively. To quantity this uncertainty, we tested the HFC-23 retrievals by making the pre-retrieved CH_4 profiles scaled by $\pm$4% and $\pm$3% at Rikubetsu and Syowa Station, respectively. Then we calculated the percent difference between the HFC-23 total column retrieved with the scaled CH_4 profile ("Scaled CH_4") and the ones retrieved with the no-scaled CH_4 profile ("Normal"). The percent difference D is defined

as the following equation:

$$D[\%] = \frac{TC_{\mathrm{HFC-23,Scaled\ CH_4}} - TC_{\mathrm{HFC-23,Normal}}}{(TC_{\mathrm{HFC-23,Scaled\ CH_4}} + TC_{\mathrm{HFC-23,Normal}})/2} \times 100, \tag{3.19}$$

where $TC_{\mathrm{HFC-23,Scaled\ CH_4}}$ and $TC_{\mathrm{HFC-23,Normal}}$ are the HFC-23 total columns retrieved with the Scaled CH_4 profile and the Normal CH_4 profile, respectively.

Table 3.4 lists the mean contributions to the relative total retrieval errors on the retrieved HFC-23 total columns at Rikubetsu for the 1997–2010 period and Syowa Station for the 2007–2016 period. Assuming that each error is independent, the total errors on retrieved total columns are simply calculated from the square root of the square sum of the error components.

At Rikubetsu, the random and systematic errors are 15% and 24%, respectively. The random error is dominated by the measurement error of 12%, and the uncertainty of 7.3% on the pre-retrieved CH_4 profile. The relative random uncertainty on the CH_4 pre-retrieved profile decreases from about 10% to about 5% during the period of 1998–2010. It indicates that the random error has been decreasing with the increasing trend of atmospheric HFC-23. The systematic error is characterized by the E'' uncertainty of HFC-23, the S_ν uncertainties of HFC-23 and CH_4, and the γ_{air} uncertainties of H_2O and HDO.

At Syowa Station, the random and systematic errors are 8.6% and 19%, respectively. The random error mostly comes from the measurement uncertainty of 6.8%, and the CH_4 pre-retrieved profile uncertainty of 4.4%. The CH_4 pre-retrieved profile uncertainty re-

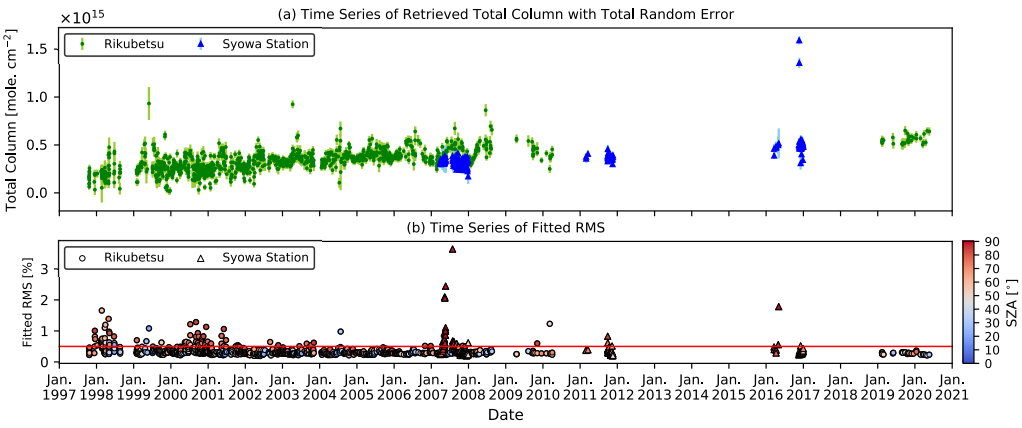

Figure 3.6: (a): Time-series of FTIR-retrieved HFC-23 total columns with total random errors at Rikubetsu and Syowa Station. (b): The fitted RMS values on individual retrieved total column. The total columns at Rikubetsu and Syowa Station are shown by green circles and blue triangles, respectively. The fitted RMS values at Rikubetsu and Syowa Station are shown by circles and triangles, respectively, with the color-coding depended on the SZA.

duces from 5% to 3% during the 2007–2016 period, similar to the result at Rikubetsu. The systematic error is mainly caused by the E'' uncertainty of HFC-23 and the S_ν uncertainties of HFC-23 and CH_4. In contrast with the retrieval at Rikubetsu, the contributions of the line parameters of H_2O and HDO are small.

As the result, the mean total error for all the retrieved HFC-23 total columns at Rikubetsu for the 1997–2010 period and Syowa Station are 28% and 21%, respectively. In our HFC-23 retrieval strategy, the retrieval error is dominated by the systematic uncertainty of the line parameters, especially the S_ν uncertainties of HFC-23 and CH_4. The contribution of the random error caused mainly by the measurement noise is relatively

small.

Figure 3.6 (a) shows the time-series of the FTIR-retrieved HFC-23 total columns with the total random errors at Rikubetsu and Syowa Station. Note that two high total columns at Syowa Station in 2016 come from temporal contamination of HFC-23 refrigerant used for Cryogenic Frost-point Hygrometer (CFH) sonde observation (Vömel et al., 2007) which was executed at the same place and days. We can see the increasing trend of the retrieved HFC-23 total columns, even taking into account the random retrieval errors on the total columns.

3.9 Impact of background correction

Since the width of the MWs for our HFC-23 retrieval is 9.5 cm^{-1} for MW1 and 6.0 cm^{-1} for MW2, the shape of continuum levels (transmittance of 1.0) in the observed spectra, which result from the characteristic of the optical filters, should be properly corrected (a so-called background correction). In this study, we used a 2nd-order polynomial (slope + curvature) for fitting of the background continuum shape for a wide MW. If a simple linear slope is employed for the background spectra, the HFC-23 total column is systematically biased toward negative. The difference between using a linear slope and of a 2nd-order polynomial was calculated using the same formula as Equation 3.19. At Rikubetsu, the mean percent difference was about -33% throughout the analysis period. At Syowa Station, the mean percent difference was about -10%, smaller than at Rikubetsu. These

relative biases lead underestimation to the trend on the retrieved HFC-23 abundances compared to that from AGAGE in-situ measurements. Therefore, it is very important that the curvature is considered to the background correction.

Table 3.4: Mean random and systematic uncertainties on FTIR-retrieved HFC-23 total columns at Rikubetsu and Syowa Station.

Site (period)	Rikubetsu (1997–2010)		Syowa Station (2007–2016)	
Error component	Random [%]	Systematic [%]	Random [%]	Systematic [%]
Smoothing	1.4		0.56	
Retrieved parameters	0.15		0.070	
Interfering species	2.8		0.51	
Measurement	12		6.8	
Temperature	3.8	3.8	1.2	1.2
SZA	1.1		2.5	
S_ν of HFC-23		10		10
E'' of HFC-23		10		15
γ_{air} of HFC-23		3.8		3.7
n_{air} of HFC-23		0.51		0.59
S_ν of N_2O		0.16		0.072
γ_{air} of N_2O		4.4		1.3
n_{air} of N_2O		0.79		0.30
S_ν of O_3		0.063		0.037
γ_{air} of O_3		0.13		0.088
n_{air} of O_3		0.054		0.038
S_ν of H_2O		0.048		0.055
γ_{air} of H_2O		6.6		2.1
n_{air} of H_2O		0.24		0.13
S_ν of HDO		0.070		0.069
γ_{air} of HDO		15		2.3
n_{air} of HDO		0.47		0.15
CH_4 pre-retrieved profile	7.3		4.4	
S_ν of CH_4		5.8		4.4
γ_{air} of CH_4		0.038		0.063
n_{air} of CH_4		0.012		0.026
Subtotal	15	24	8.6	19
Total	28		21	

Chapter 4

Retrieval of atmospheric HCFC-22

There is the closed relationship between productions of HCFC-22 and HFC-23. To invest the variations of the retrieved HFC-23 total column abundances from the FTIR measurements at Rikubetsu and Syowa Station, I also retrieve atmospheric HCFC-22 abundances from these FTIR measurements.

The main absorption features of HCFC-22 are the Coriolis-coupled doublets ν_3 (around 1108.7 cm^{-1}) and ν_8 (around 1127.1 cm^{-1}) and the Q-branches ν_4 (around 809.3 cm^{-1}) and $2\nu_6$ (around 829.1 cm^{-1}). The most intense features of HCFC-22 is the $2\nu_6$ band and then this band has been intensively used in various studies with FTIR spectrometry.

Remote sensing of HCFC-22 using IR spectroscopic technique has been made since the 1980s. Goldman et al. (1981) first identified absorption feature of atmospheric HCFC-22 obtained from IR spectra with a FTIR instrument during a balloon flight and estimated its

mixing ratio. Remote sensing of HCFC-22 from satellite has started by the Atmospheric Trace Molecule Spectroscopy (ATMOS) instrument onboard the Spacelab 3 in 1985 (Zander et al., 1987). Recently other satellite measurements of HCFC-22 have been made by Atmospheric Chemistry Experiment-Fourier Transform Spectrometer (ACE-FTS) on SCISAT (Rinsland et al., 2005; Brown et al., 2011), or Michelson Interferometer for Passive Atmospheric Sounding (MIPAS) on Envisat (Moore and Remedios, 2008; Chirkov et al., 2016).

Ground-based remote sensing of HCFC-22 with FTIR has been made since 1980 at Kitt Peak, Arizona, U.S.A. (Rinsland et al., 1989), or at Jungfraujoch, Switzerland (Zander et al., 2005). Trend analyses using ground-based FTIR data have been made in both hemispheres (Zander et al., 1994; Sherlock et al, 1997; Gardiner et al., 2008; Zhou et al, 2016; Prignon et al., 2019). Good agreement was found between FTIR and GC-MS in-situ measurements (Gardiner et al., 2008; Zhou et al., 2016; Prignon et al., 2019).

4.1 Retrieval strategy

In this study, the retrievals of atmospheric HCFC-22 abundances at Rikubetsu and Syowa Station are performed with the SFIT4 version 0.9.4.4 program (see Section 3.1), following the HCFC-22 retrieval strategy of Prignon et al. (2019). Table 4.1 summarizes the strategy for the retrieval of HCFC-22 executed in this study. For the retrieval from the FTIR measurements at both sites, the $2\nu_6$ band of HCFC-22 located around 829 cm^{-1}

Table 4.1: Summary of retrieval settings used for HCFC-22 retrievals.

Spectral region [cm^{-1}]	828.75–829.40
Profile retrieval	HCFC-22, O_3
Column retrieval	H_2O, CO_2
Pre-retrieval	H_2O
Spectroscopic parameters	PLL (HCFC-22)
	ATM18 (H_2O)
	HITRAN2008 (others)
Pressure and temperature	NCEP Reanalysis-1, CIRA86
A priori profiles (HCFC-22)	Mean profiles in the period of 1995–2010 (Rikubetsu) / 2007 – 2016 (Syowa Station) from WACCM version 6
A priori profiles (others)	WACCM version 6 mean profiles from 1980 to 2020
Signal-to-noise ratio (SNR)	Calculated from each observed spectrum
Background correction	Slope, Curvature
Instrumental line shape (ILS)	LINEFIT9/14

is used and the MW has the spectral range from 828.75 cm^{-1} to 829.40 cm^{-1}. Major interfering species in the MW are H_2O, CO_2, and O_3. While the profile of O_3 is retrieved in addition to HCFC-22, H_2O and CO_2 are simply scaled. As no resolved line-lists like the HITRAN are available for such relatively heavy molecules, I use a pseudo-line-list (PLL) created by Geoffrey C. Toon (see `https://mark4sun.jpl.nasa.gov/pseudo.html`). The PLL was built by fitting the cross-sections calculated by McDaniel et al. (1991) and Varanasi et al. (1994). For the calculation of absorption by CO_2 and O_3, the HITRAN 2008 database (Rothman et al., 2009) was primarily used. For spectroscopic parameters for H_2O, the updated ATM18 line-list by one of us (G. C. Toon, NASA/JPL) was used (For detail, see `https://mark4sun.jpl.nasa.gov/toon/atm18/atm18.html`).

I consider 47 atmospheric layers for Rikubetsu, and 48 layers for Syowa Station from ground to 120 km in altitude. The thickness of the layers increases with height. We used the NCEP Reanalysis-1 daily temperature and pressure data (`http://www.ncep.noaa.gov`) from the ground to 40 km, and zonal monthly-mean climatological profiles by the CIRA-86 from 40 km to 120 km (Rees et al., 1990). For a priori profiles of atmospheric compositions, the averaged profiles in the period of 1980–2020 derived from the monthly-mean profile data computed by the Whole Atmospheric Community Climate Model (WACCM) version 6 (Chang et al., 2008) were basically used. For HCFC-22, the mean profiles for 1995–2010 at Rikubetsu and for 2007–2016 at Syowa Station derived from the WACCM monthly dataset were used, because these species in the atmosphere have rapidly increased since 1980. For H_2O, a priori profiles were pre-retrieved using other independent MW: 824.40–825.90 cm^{-1} shown in the Atlas (Meier et al., 2004). Regarding selection of regularization matrix, the Tikhonov L_1 regularization was here used since the regularization suppresses oscillation of the retrieved profile. The determination of the regularization parameter α as a constraint strength was performed with the L-curve method (Hansen, 1992; Steck, 2002). In this study, $\alpha = 50$ was adopted for the observations at Rikubetsu and Syowa Station, as a constraint strength to minimize the total retrieval error. The measurement noise covariance matrix $\boldsymbol{S_\varepsilon}$ is a diagonal matrix with SNR^{-2} in its diagonal elements.

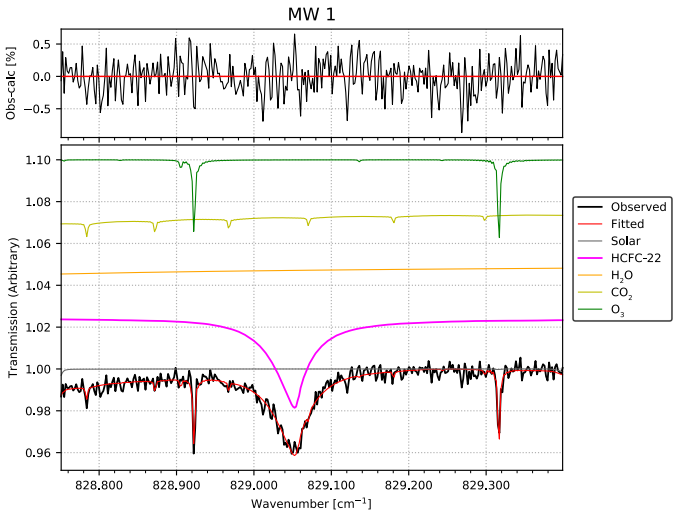

Figure 4.1: Typical spectral simulation results of the HCFC-22 retrieval micro-window fitted to the observed spectrum at Syowa Station on 9 November 2011 at 12:11 UTC. The top panel shows the residuals (observed minus calculated). The bottom panel show the individual contributions from each interfering species, shifted by multiples of 0.025 for clarity, except the observed and the calculated lines.

4.2 Result of HCFC-22 retrievals

Figure 4.1 shows an example of a spectral fitting result for the MW for HCFC-22. This typical fitting was for a spectrum observed by the IFS-120M FTIR spectrometer at Syowa Station on 9 November 2011 at 12:11 UTC with a solar zenith angle (SZA) of 59.5°. In this case, the absorption contribution of HFC-23 is about 4% relative to the total transmittance, corresponding to a total column of 4.15×10^{15} molecules cm^{-2}. The typical root-mean-square (RMS) of the fitted residual (observed minus calculated spectrum) is 0.34%.

A summary of all the HCFC-22 retrievals with SFIT4 at Rikubetsu and Syowa Station

is shown in Table 4.2. The retrievals at Rikubetsu are summarized for the periods of 1997–2010 and 2019–2020 due to use of different instruments. The retrievals without negative values in profile were counted into the number of observations as the "valid" number, and those results were used to calculate each statistic. The mean RMS of the fitted residuals with the one standard deviation (1σ) at Rikubetsu is $0.53 \pm 0.36\%$ and $0.62 \pm 0.09\%$ for the 1997–2010 and 2019–2020, respectively. The mean RMS with 1σ at Syowa Station is $0.53 \pm 0.47\%$. The mean HFC-23 total column with 1σ standard deviation at Rikubetsu increased from $(3.35 \pm 0.51) \times 10^{15}$ molecules cm^{-2} in the 1997–2010 period to $(5.20 \pm 0.29) \times 10^{15}$ molecules cm^{-2} in the 2019–2020 period due to the increase of atmospheric HCFC-22.

Table 4.2: Statistic summary of the fitted SNRs, the root-mean-squares (RMSs) of the fitted residuals (observed minus calculated spectrum), the degree of freedom for signals (DOFSs) and the retrieved HCFC-22 total columns at Rikubetsu and Syowa Station. The errors of the fitted RMSs, the DOFSs, and the total columns are the one standard deviation (1σ) around the averages. The numbers of the HFC-23 retrievals (N) are divided into two parts of a number of the retrievals used in this analysis (valid) and of total ones including rejected ones (total). Site (instrument) Rikubetsu (IFS-120M) Rikubetsu (IFS-120/5HR) Syowa Station (IFS-120M)

Site (instrument)	Period	N (valid / total)	Mean fitted SNR	Mean fitted RMS [%]	Mean DOFS	Mean HCFC-22 total column [10^{15} molecules cm^{-2}]
Rikubetsu (IFS-120M)	1997–2010	1146/1152	224	0.53 ± 0.36	1.1 ± 0.1	3.35 ± 0.51
Rikubetsu (IFS-120/5HR)	2019–2020	30/30	165	0.62 ± 0.09	1.0 ± 0.02	5.20 ± 0.29
Syowa Station (IFS-120M)	2007–2016	222/224	237	0.53 ± 0.47	1.1 ± 0.2	4.07 ± 0.57

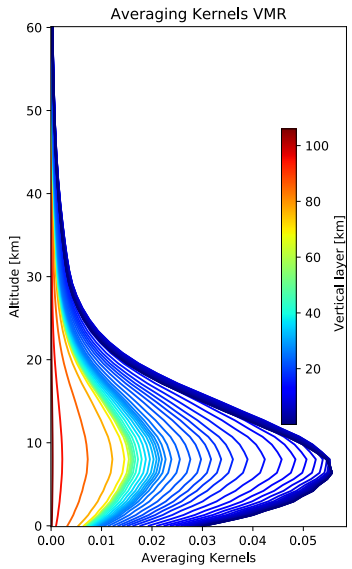

Figure 4.2: Typical averaging kernels of the HCFC-22 retrieval for the same spectrum shown in Figure 4.1, which are normalized using the a priori profile. Note that the vertical scale is from surface up to 60 km because there is almost no sensitivity above 60 km.

Figure 4.2 shows typical averaging kernels of the HFC-23 retrieval for the same spectrum shown in Figure 4.1. Each curve coloured according to the right colour-bar in Figure 4.2 represents the row value of the averaging kernel matrix on the corresponding vertical layer. All the retrievals, including the typical case in Figure 4.2, are sensitive to troposphere and lower stratosphere, having a sensitivity peak in averaging kernel at about 4 km. The full widths at half maximum of the averaging kernels are about 20 km, and the mean DOFS for both all retrievals at Rikubetsu and Syowa Station is approximately 1.0. Therefore, only one piece of vertical information (the total column) can be extracted in this study.

4.3 Error analysis

The retrieval error consists of four parts: the smoothing error $(\boldsymbol{A}-\boldsymbol{I})(\boldsymbol{x}-\boldsymbol{x}_{\mathbf{a}})$, the non-retrieved forward model parameter error $\boldsymbol{G}\boldsymbol{K}_{\mathbf{b}}\boldsymbol{\varepsilon}_{\mathbf{b}}$, the forward model error $\boldsymbol{G}\boldsymbol{\varepsilon}_{\mathbf{f}}$ and the measurement noise $\boldsymbol{G}\boldsymbol{\varepsilon}$ (for details, see Section 3.8).

The smoothing error for HCFC-22 is computed from a variability matrix of the a priori profile of HCFC-22. For the observations at Rikubetsu, the variability of 20% against the a priori profile (square of $0.20\boldsymbol{x}_{\mathbf{a}}$), which was calculated from the used WACCM datasets over the period of 1997–2010, was adopted to the diagonal elements of the variability matrix. For Syowa Station, the variability of 10% against the a priori profile (square of $0.10\boldsymbol{x}_{\mathbf{a}}$), which was calculated from the used WACCM datasets over the period of 2007–2016, was set to the diagonal elements of the matrix.

The smoothing random errors for the retrieval uncertainties from all interfering species and some other retrieval parameters (background slope and curvature correction, wavenumber shift, solar line shift, solar line strength, and simple phase correction) were calculated in the same way as mentioned in Section 3.8. To estimate the retrieval errors from the interfering gases, the variabilities around the a priori profiles for H_2O were set to 10% and the ones for other species were set to the values calculated from the used WACCM datasets.

In order to estimate the non-retrieved forward model parameter error, the following variabilities was used for each parameter. For the random and systematic uncertainties of

Table 4.3: Mean random and systematic uncertainties on FTIR-retrieved HCFC-22 total columns at Rikubetsu and Syowa Station.

Site (period)	Rikubetsu (1997–2010)		Syowa Station (2007–2016)	
Error component	Random [%]	Systematic [%]	Random [%]	Systematic [%]
Smoothing	1.2		0.60	
Retrieved parameters	0.47		0.25	
Interfering species	0.31		0.17	
Measurement	5.5		2.9	
Temperature	0.46	0.46	0.57	0.57
SZA	0.45		1.0	
S_ν of HCFC-22		5.0		5.0
Subtotal	5.6	5.0	3.2	5.0
Total	7.5		5.9	

temperature at Rikubetsu and Syowa Station, the uncertainties on the NCEP temperature profiles were assumed. The uncertainty of temperature at Rikubetsu is about 2 K in the troposphere, 2–10 K between the tropopause and 60 km, and 10 K above 60 km. The uncertainty of temperature at Syowa Station is about 2.5 K in the altitude range from the surface to 20 km, 2.5–10 K between 20 and 60 km, and 10 K above 60 km. The SZA random uncertainty was assumed an uncertainty of 0.15°. For HCFC-22, O_3, H_2O, and CO_2, the uncertainties of the spectroscopic parameters (i.e. line intensity, S_ν; air-broadening coefficient, γ_{air}; temperature dependence coefficient for γ_{air}, n_{air}) were also estimated. For the uncertainties of S_ν, γ_{air}, and n_{air} of HCFC-22, we set 5%, based on the PLL database (see `https://mark4sun.jpl.nasa.gov/pseudo.html`). For O_3, H_2O, and CO_2, the spectroscopic uncertainties were derived from the HITRAN 2008 database. The

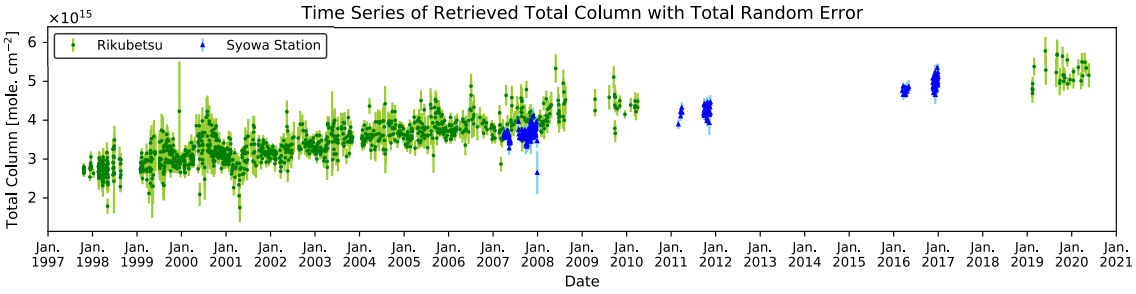

Figure 4.3: Time-series of FTIR-retrieved HCFC-22 total columns with total random errors at Rikubetsu and Syowa Station.

uncertainties for O_3 were set with 5%, 10%, and 5% for S_ν, γ_{air}, and n_{air}, respectively. For H_2O, I gave the uncertainty of 10% to each parameter. For CO_2, the uncertainties for S_ν, γ_{air}, and n_{air} were set with 5%, 10%, and 10%, respectively. The measurement error was estimated from the measurement noise covariance matrix $\boldsymbol{S_\varepsilon}$ with the square inverse of the *ad hoc* SNR for the diagonal elements of $\boldsymbol{S_\varepsilon}$ as mentioned in Section 3.5.

The error budgets on the retrieved total columns at Rikubetsu and Syowa Station are listed in Table 4.3. At Rikubetsu, the mean total error is 7.5% with the random component of 5.6% and systematic component of 5.0%, which is mainly caused by the uncertainties of the random measurement noise of 5.5% and the systematic HCFC-22 line intensity parameter of 5.0%. At Syowa Station, the mean total error is 5.9% including the random component of 3.2% and the systematic component of 5.0%, which is dominantly caused by the HCFC-22 line intensity parameter uncertainty of 5.0%. These results are consistent with the error budget at Jungfraujoch which was reported in Prignon et al. (2019).

Figure 4.3 shows the time-series of the retrieved HCFC-22 total columns with the total random errors at Rikubetsu and Syowa Station. There are clearly the increasing trends of the retrieved HCFC-22 total columns at both sites.

Chapter 5

Disscussion

5.1 Trend analysis of HFC-23

5.1.1 Datasets

Ground-based FTIR data

In this study, the fitted RMS residuals for most retrievals were less than 0.5% (Table 3.3, Figure 3.6 (b), and Figure 5.1). Figure 3.6 (b) shows the time-series of the fitted RMS residuals at Rikubetsu and Syowa Station, along with the SZA. In general, the RMS values rise with increasing SZA due to a decrease in the SNR as shown in Figure 5.1. However, with SZA lower than 50°, there are some observations with fitted RMS values exceeding 0.5% at Rikubetsu before 1999. This is caused by relatively poor optical alignment of the FTIR instrument until April 1999 when a Bruker technician re-aligned the instrument.

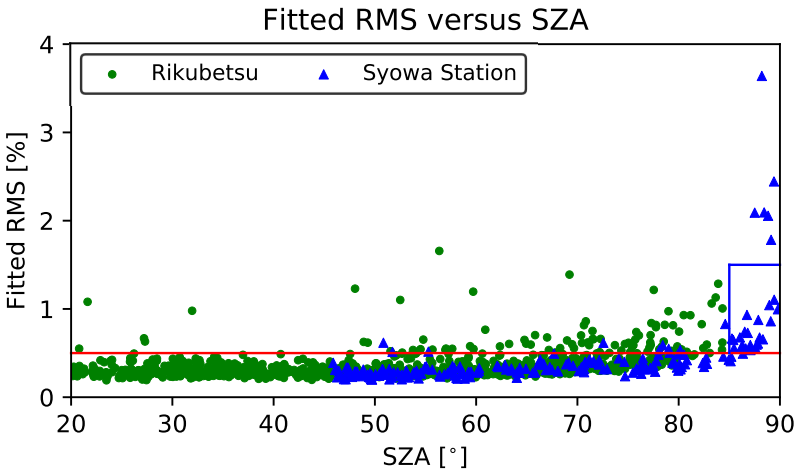

Figure 5.1: The fitted RMS residuals versus the SZA values on individual retrieval. The RMS values at Rikubetsu and Syowa Station are shown by green circles and blue triangles, respectively.

In the following analysis, we basically use the FTIR-retrieved HFC-23 data filtered with the threshold of the fitted RMS ($< 0.5\%$) in order to make the FTIR-retrieved data as uniform in quality as possible. However, this threshold rejects most retrievals at Syowa Station in winter when ground-based FTIR observations at large SZA generally give large RMS for the spectral fit residuals due to weak solar intensity. Thus, for the retrievals at Syowa Station, we applied two fitted RMS thresholds depending on the value of SZA: the thresholds are $< 0.5\%$ for SZA $< 85°$ and $< 1.5\%$ for SZA of $85°$ or greater. Note that the high HFC-23 abundances caused by the water vapor profile observations with a CFH-sonde at Syowa Station in 2016, as mentioned in Section 3.8, are also excluded.

Since the HFC-23 retrievals have only one piece of vertical information, as already

mentioned in Section 3.7, we consider the dry-air column-averaged mole fractions $X_{\mathrm{HFC-23}}$ as the following formula:

$$X_{\mathrm{HFC-23}} = \frac{TC_{\mathrm{HFC-23}}}{TC_{\mathrm{dry}}} = \frac{TC_{\mathrm{HFC-23}}}{\frac{p_{\mathrm{s}} N_{\mathrm{A}}}{g m_{\mathrm{dry}}} - TC_{\mathrm{H_2O}} \frac{m_{\mathrm{H_2O}}}{m_{\mathrm{dry}}}} \tag{5.1}$$

where $TC_{\mathrm{HFC-23}}$, TC_{dry}, and $TC_{\mathrm{H_2O}}$ are the FTIR-retrieved HFC-23 total column, the dry-air total column, and the a priori (pre-retrieved) H_2O total column, respectively; p_{s} is the surface pressure calculated from the NCEP reanalysis; N_{A} is Avogadro's constant; g is the column-averaged acceleration; m_{dry} and $m_{\mathrm{H_2O}}$ are the mean molecular masses of dry-air and H_2O, respectively. Finally, we calculated the monthly mean column-averaged $X_{\mathrm{HFC-23}}$ at both sites.

AGAGE in-situ and air archive measurements

The AGAGE instruments are based on gas chromatography coupled with mass spectrometry (GC-MS) and cryogenic sample pre-concentration system, so-called "Medusa" systems. The GC-MS-Medusa systems, with 2-hourly sampling and cooling to $\sim -180\,^{\circ}\mathrm{C}$, are operated at each AGAGE station (Miller et al., 2008; Arnold et al., 2012). For HFC-23, reported in-situ measurements started in 2007, after HFC-23 contamination from the air pump module had been resolved by changing from Viton to Neoprene diaphragms (KNF Neuberger UN05 pumps). The HFC-23 abundances at all AGAGE stations are reported relative to Scripps Institution of Oceanography (SIO), SIO-07 primary calibration

scales, in dry-air mole fractions. The absolute accuracies of the HFC-23 measurements were liberally estimated to be −3 to 2% (Simmonds et al., 2018a).

For the comparison with the FTIR measurements at Rikubetsu and Syowa Station, we used the AGAGE in-situ measurement HFC-23 data at Trinidad Head, California, USA (THD, 41.1°N, 124.2°W) and Cape Grim, Tasmania, Australia (CGO, 40.7°S, 144.7°E), respectively. We downloaded the high frequency HFC-23 in-situ measurement dataset for THD and CGO and used the embedded pollution flags (P) to remove polluted data (`https://agage2.eas.gatech.edu/data_archive/agage/gc-ms-medusa/complete/`) and then calculated daily median mole fractions. Note that there are no in-situ measurements at THD and CGO or other AGAGE sites before 2007 due to the HFC-23 pump contamination problems. Therefore, we additionally used annual global mean mole fractions of HFC-23 estimated by the AGAGE 12-box model, a 2-dimensional atmospheric chemistry and transport model (Simmonds et al., 2018a), where pre-2007 abundances are only based on HFC-23 dry-air mole fractions measured in the Cape Grim Air Archive (CGAA) samples (Simmonds et al., 2018b). These data were taken from the Simmonds et al. (2018a; 2018b) papers.

5.1.2 Time-series and seasonal variation

Figure 5.2 shows the time-series of the monthly mean FTIR-retrieved $X_{\mathrm{HFC-23}}$ at Rikubetsu and Syowa Station, along with the dry-air mole fractions from the AGAGE annual global mean dataset, the CGAA samples, and the in-situ measurements at THD

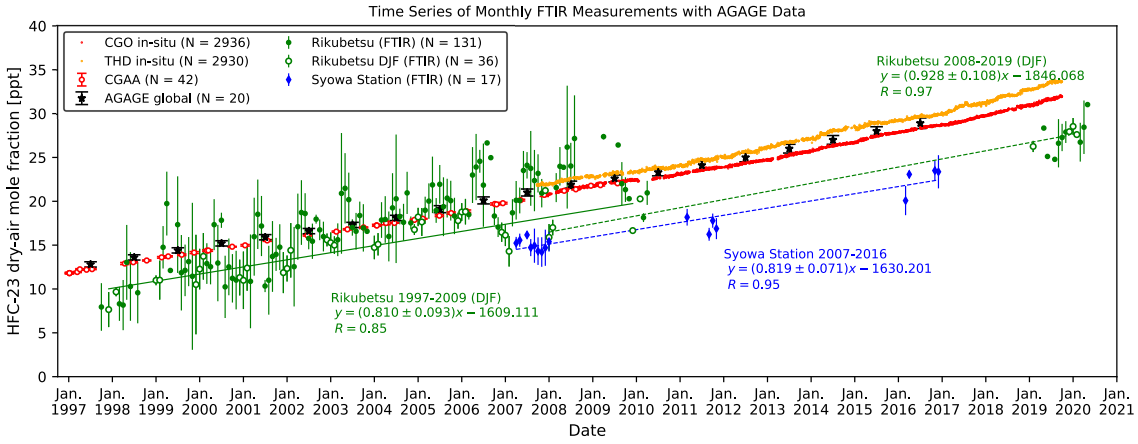

Figure 5.2: Time-series of the monthly mean FTIR-retrieved $X_{\mathrm{HFC-23}}$ at Rikubetsu and Syowa Station, along with the AGAGE in-situ measurements at CGO and THD, and the annual global mean mole fractions and the Cape Grim Air Archive samples, which were reported by Simmonds et al. (2018b).

and CGO. The error bar on each monthly mean $X_{\mathrm{HFC-23}}$ is 1σ standard deviation around the monthly mean. The AGAGE annual global mean data and the CGAA data are plotted with the uncertainties reported by Simmonds et al. (2018a, 2018b). The FTIR-retrieved $X_{\mathrm{HFC-23}}$ data at Rikubetsu during the whole period look consistent with the AGAGE annual global mean and the CGAA data. However, the FTIR dataset at Rikubetsu has a peak during spring and summer. In contrast, the time-series at Syowa Station has a systematic underestimation of about 5 ppt (about 25% relative to the CGO in-situ data in 2007) compared to the CGO in-situ data, and almost no significant seasonal cycle.

Figure 5.3 shows monthly mean de-trended $X_{\mathrm{HFC-23}}$ values (in percent, relative to the trend for all data) and 1σ standard deviations at Rikubetsu and Syowa Station. At

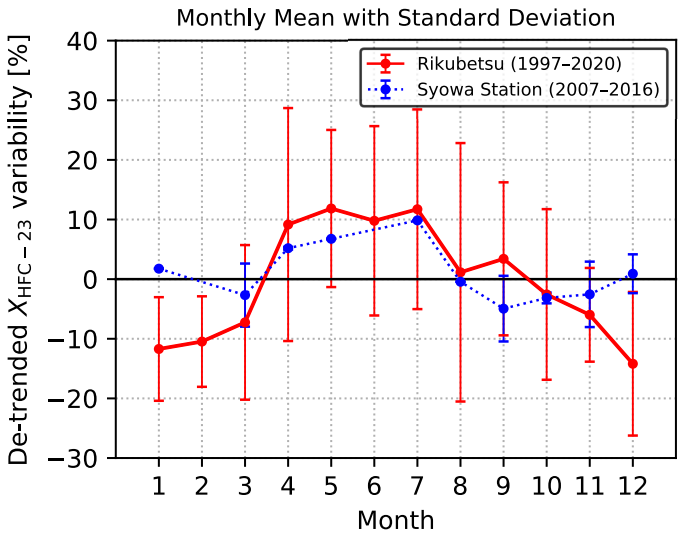

Figure 5.3: Seasonal cycles of the FTIR-retrieved $X_{\mathrm{HFC-23}}$ at Rikubetsu for the 1997–2020 period and at Syowa Station for the 2007–2016 period. Year-to-year variability is shown as 1σ standard deviation for each month. At Syowa Station, there are no observations in February and June and only 1 year of observations for January, May, July, and August; hence, no 1σ standard deviations are plotted for these months.

Rikubetsu, the monthly mean de-trended $X_{\mathrm{HFC-23}}$ shows high values from April to July, with large year-to-year variability ($\pm$15%–20%) for each month. On the other hand, the monthly mean $X_{\mathrm{HFC-23}}$ values from December to February are mostly stable, with relatively small standard deviations of about $\pm$10% and a value of 10–15% smaller than the AGAGE in-situ measurements of HFC-23. As mentioned in Section 1.5, HFC-23 has a very long lifetime of 228 years and there is almost no sink for HFC-23 in the atmosphere, i.e. HFC-23 is chemically inactive in the atmosphere. In addition, the sources of HFC-23 exist in limited places on the ground. For example, there is no HCFC-22

production in Australia and therefore Cape Grim is not impacted by this major source of HFC-23. Consequently, we expect almost no seasonal variation of the HFC-23 dry-air mole fraction at any remote site as seen in the times-series of the THD and CGO measurements. At Syowa Station, for which there are no observations in February and June and only 1 year of observations for January, May, July, and August, the seasonal cycle on the FTIR-retrieved $X_{\mathrm{HFC-23}}$ is almost unrecognized in Figure 5.3 because the variability is smaller than the retrieval random error of about 10%. We suspected some retrieval artifacts and checked the correlations between HFC-23 and H_2O, HFC-23 and temperature, and HFC-23 and HDO/H_2O. There is temperature dependency on the PLL and this explains the 5% difference in the maximum (see Section 5.1.3 for more details), but we could not find any other significant retrieval artifacts. Note that enhancements of HFC-23, especially in spring and summer, are also observed by the surface measurements at Cape Ochiishi (43.2°N, 145.5°E), which is located close (about 150 km) to Rikubetsu (https://gaw.kishou.go.jp/search/file/0053-2008-1502-01-01-9999). As a hypothesis, we suggest that the peaks at Rikubetsu during spring–summer were affected by enhancements due to atmospheric transport from a region emitting HFC-23. Several previous studies using FTIR observations of biomass-burning-derived gases and a backward trajectory analysis method (Zhao et al., 1997; 2002; Nagahama and Suzuki, 2007) showed that the airmasses over northern Japan at 800–300 hPa level during April to November were mostly transported from the Eurasian continent. Furthermore, Koike et al. (2006) investigated the seasonal contribution from various sources of tropospheric carbon monoxide

(CO) at Rikubetsu in 2001 using a three-dimensional global chemistry transport model. Their study showed that, for CO levels at 1 km, the contribution from Asian fossil fuel combustion increases from early spring to summer due to Asian pollutants transported by the weak southwesterly wind in summer. We also calculated 10-day backward trajectories for all FTIR measurement days from Rikubetsu originating at 2000 m, and the results show that, for example, nearly 30% of air masses above Rikubetsu came from China in 2006 (see Section 5.3 for more details). Figure 5 (a) of Simmonds et al. (2018a) illustrated that while the contribution to annual global emission of HFC-23 has been decreasing since 2000 for developed countries (e.g. Europe, Japan, USA), annual Chinese emission has been rapidly increasing since the late 1990s and the contribution of Chinese emission to global emission exceeded 50% in the early 2000s. Considering this, we suggest that the peaks of $X_{\mathrm{HFC-23}}$ at Rikubetsu during spring–summer before and after about 2002 may be affected by HFC-23 emissions in Japan and China, respectively. This postulated change in the location of Eurasian HFC-23 emissions needs to be examined with an inversion study, but this exceeds the focus of our study.

I also propose that the FTIR observations at Rikubetsu in December, January, and February (DJF) represent the baseline of the atmospheric HFC-23 at the site. Although the observations at Rikubetsu look consistent with the AGAGE measurements as seen in Figure 5.2, the retrievals at Rikubetsu in DJF have a negative bias of 3 to 4 ppt. The FTIR-retrieved $X_{\mathrm{HFC-23}}$ data at Rikubetsu in DJF are shown as green open circles in Figure 5.2. In Section 5.1.4, the trends for the $X_{\mathrm{HFC-23}}$ data in DJF are derived.

These trends are compared with the AGAGE measurements and whether the DJF dataset represents the background level of HFC-23 at Rikubetsu or not. For the trend analysis at Syowa Station, all $X_{\mathrm{HFC-23}}$ data are used due to no significant seasonal cycle. The negative biases occurred at both FTIR sites are described in the following section.

5.1.3 Negative bias on $X_{\mathrm{HFC-23}}$

The negative bias with respect to the AGAGE surface measurements of the FTIR-retrieved $X_{\mathrm{HFC-23}}$ at Syowa Station (about 25% in 2007) is larger than that at Rikubetsu (about 15% in 2007). The difference of 10% between both sites could be explained by (1) the latitudinal concentration difference and (2) the temperature dependency of the derived HFC-23 pseudo-line parameter. With regard to the latitudinal concentration difference, Figure 1 of Simmonds et al. (2018a) shows that the difference between the in-situ measurements at mid-latitude in the Northern and Southern Hemisphere is about 1 ppt (5% in 2007). For the remaining of 5% of our observed difference, by using the PLL we retrieved the HFC-23 mole fraction values from each spectrum of four laboratory measurement datasets, which had been used to create the HFC-23 PLL (see Section 3.4), and then investigated the discrepancies between the retrieved mole fractions and the reported ones in the laboratory datasets. We here represent the discrepancies by the HFC-23 mole fraction scaling factors (MFSFs). Figure 5.4 (a) shows the HFC-23 MFSFs at the spectral region from 1105–1240 cm^{-1} plotted versus temperature. In an ideal spectroscopic parameter, the MFSFs in all temperature region would be 1. The red

plots in regard to the laboratory spectral dataset of Harrison (2013) in Figure 5.4 (a) present the curved temperature dependency like a parabola, taking a minimum value of ~ 0.95 at around 240 K. In other words, it means that a retrieved mole fraction from a spectrum measured at 240 K is about 5% smaller than the actual mole fraction. As the annual mean surface temperature at Syowa Station is about 260 K, it is assumed that this temperature dependency caused the negative bias of 5% at Syowa Station, in addition to the latitudinal concentration contrast. Also, this temperature dependency on the PLL probably has affected the HFC-23 total columns at Rikubetsu. As shown in Figure 5.4 (a), the MFSFs of the Harrison's laboratory measurements at > 260 K rapidly increase with raising temperature. Therefore, the temperature dependency may cause some of the seasonal variation of HFC-23 at Rikubetsu because the surface temperature at the site ranged from 260 K to 300 K. For the unrealistic cycle of $X_{\mathrm{HFC-23}}$, with a maximum in summer caused by the PLL, we estimated an amplitude of about 1 ppt as peak-to-peak value.

Here we assess the large negative bias of 15% on the FTIR-retrieved $X_{\mathrm{HFC-23}}$ at both sites. As mentioned in Section 3.8, our HFC-23 retrieval was mainly affected by the spectroscopic parameter uncertainties of HFC-23, HDO, and CH_4. Therefore, it is reasonable to assume that the negative bias mainly comes from the systematic uncertainty of these spectroscopic parameters. This is consistent with the negative average difference of 5% of the ACE-FTS HFC-23 time series compared to the annual global mean data calculated by the AGAGE 12-box model illustrated in Fernando et al. (2019), which is based on the

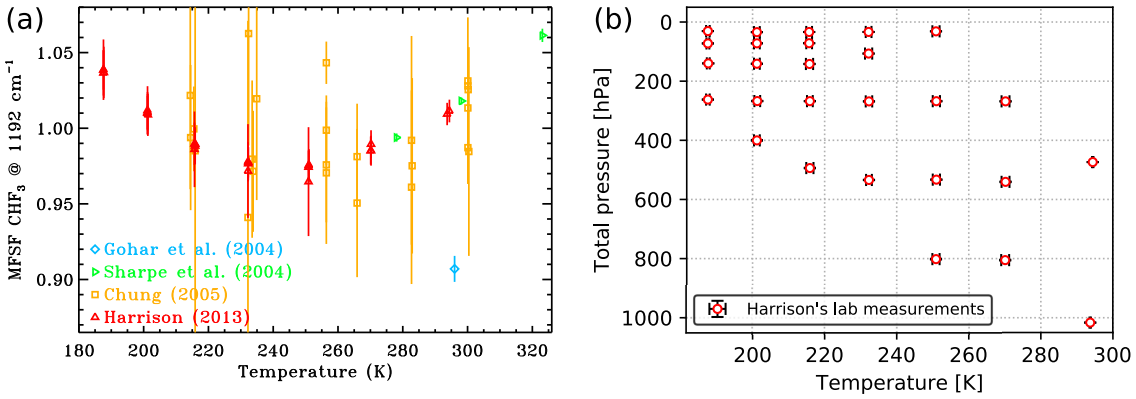

Figure 5.4: (a): Retrieved mole fraction scaling factors from four HFC-23 laboratory spectrum datasets using the 2020 HFC-23 PLL at the spectral region from 1105–1240 cm^{-1} plotted versus temperature. (b): The temperature and pressure conditions of the laboratory measurements of Harrison (2013).

Harrison laboratory spectra. However, it is difficult to quantify the contributions of these parameters to the bias in $X_{\mathrm{HFC-23}}$. In order to resolve the negative bias, we suggest that new laboratory measurements are needed to improve the spectroscopic parameters of the HFC-23 PLL. The negative bias of 15% is consistent with the systematic uncertainty of the HFC-23 line intensity, which is estimated by the error analysis in Section 3.8. We suggest that the systematic uncertainty is affected by the temperature and pressure conditions in measuring the laboratory spectra of HFC-23. Figure 5.4 (b) shows the conditions of the HFC-23 laboratory measurements of Harrison et al. (2013). Harrison's laboratory measurements (total 27 measurements) cover the temperature and pressure region corresponding to the altitude from the surface to the stratosphere, but the number of the

measurements corresponding to the lower troposphere (below 600 hPa level) is only 3. The typical surface temperatures at Rikubetsu and Syowa Station range from 260 K to 300 K and from 240 K to 280 K, respectively. Hence, at a pressure corresponding to the surface, there is no measurement in the temperature region covering the surface temperature at Rikubetsu, except for summer, and Syowa Station. This lack of the measurements could result in a significant error in creating the HFC-23 pseudo-line parameters. Therefore, high-accuracy laboratory spectra of HFC-23 are required at various atmospheric conditions of lower troposphere in order to improve the pseudo-line parameters of HFC-23. In addition, further studies should be undertaken to understand the reason for the negative bias and the apparent seasonal cycle by intercomparison with HFC-23 total columns at other NDACC-IRWG ground-based FTIR sites around the world.

5.1.4 Trend of atmospheric HFC-23

Table 5.1 summarizes the HFC-23 annual changes, in ppt year^{-1}, computed from the monthly $X_{\mathrm{HFC-23}}$ at both FTIR sites and from the AGAGE datasets. The columns of Table 5.1 represent the trend in the time periods of 1997–2009, 2008–2019, and 2007–2016 according to the available data periods of both FTIR and AGAGE datasets. The annual growth rates were calculated by linear regression, and any seasonal cycles were neglected. The uncertainty in each annual growth rate represents the standard error of the slope estimated by linear regression. The trend regression line for the $X_{\mathrm{HFC-23}}$ data at Rikubetsu in DJF over the 1997–2009 and 2008–2019 period, shown in Figure 5.2 as

Table 5.1: HFC-23 annual changes and standard errors derived from monthly mean $X_{\mathrm{HFC-23}}$ at Rikubetsu and Syowa Station, in ppt year^{-1}. The annual growth rates computed from the AGAGE annual global mean dataset, the CGAA air sample dataset, and the AGAGE in-situ measurements at THD and CGO are also listed for the same periods, unless indicated by other time frames lists in brackets.

Observation site, dataset	Annual change [ppt year^{-1}]		
Data period	1997–2009	2008–2019	2007–2016
Rikubetsu DJF (FTIR)	0.810 ± 0.093	0.928 ± 0.108	–
Syowa Station (FTIR)	–	–	0.819 ± 0.071
Annual global mean (12-box model)	0.820 ± 0.013	0.892 ± 0.023 (2008–2016)	0.878 ± 0.020
CGAA	0.805 ± 0.006	–	–
THD (AGAGE in-situ)	–	0.994 ± 0.001	–
CGO (AGAGE in-situ)	–	–	0.874 ± 0.002

green solid and green-dashed line, are consistently lower than the AGAGE datasets by about 3 to 4 ppt (-15% to -20% relative to the AGAGE in-situ measurements in 2007), as mentioned in Section 5.1.2. However, the annual growth rate calculated from $X_{\mathrm{HFC-23}}$ data at Rikubetsu in DJF over 1997–2009 (0.810 ± 0.093 ppt year^{-1}) is in good agreement with the AGAGE annual global mean data (0.820 ± 0.013 ppt year^{-1}) and the CGAA data (0.805 ± 0.006 ppt year^{-1}) within the uncertainties. For the 2008–2019 period, the annual growth rate at Rikubetsu in DJF (0.928 ± 0.108 ppt year^{-1}) is consistent with the one derived from the AGAGE annual global mean dataset during 2008 to 2016 (0.892 ± 0.023 ppt year^{-1}) and that of the AGAGE in situ measurements at THD (0.994 ± 0.001 ppt year^{-1}), even though the differences of the annual growth rates are a bit larger than those

in the period of 1997–2009. Considering the above, we argue that the FTIR-retrieved $X_{\mathrm{HFC-23}}$ data in DJF represent the baseline of the atmospheric HFC-23 at Rikubetsu.

At Syowa Station, the annual growth rate over the 2007–2016 period (0.819 ± 0.071 ppt year^{-1}) is consistent with the annual global mean dataset (0.878 ± 0.020 ppt year^{-1}) and the GAGE CGO in situ measurements (0.874 ± 0.002 ppt year^{-1}) over the same period.

Summarizing the above, the trends of the atmospheric HFC-23 retrieved with our strategy agree within the errors with the trends derived from the AGAGE datasets, while the absolute values of HFC-23 are biased low. These results indicate that ground-based FTIR measurement has the capacity to monitor the long-term trends of HFC-23.

5.2 Trend analysis of HCFC-22

5.2.1 Datasets

Ground-based FTIR data

The fitted RMS residuals for most HCFC-22 retrievals at both sites were less than 1% (Table 4.2 and Figure 5.5). In the following analysis, we basically use the FTIR-retrieved HCFC-22 data filtered with the threshold of the fitted RMS ($< 1\%$) in order to make the FTIR-retrieved data as uniform in quality as possible.

Since the HCFC-22 retrievals have only one piece of vertical information, as already mentioned in Section 4.2, the dry-air column-averaged mole fractions $X_{\mathrm{HFC-23}}$ are con-

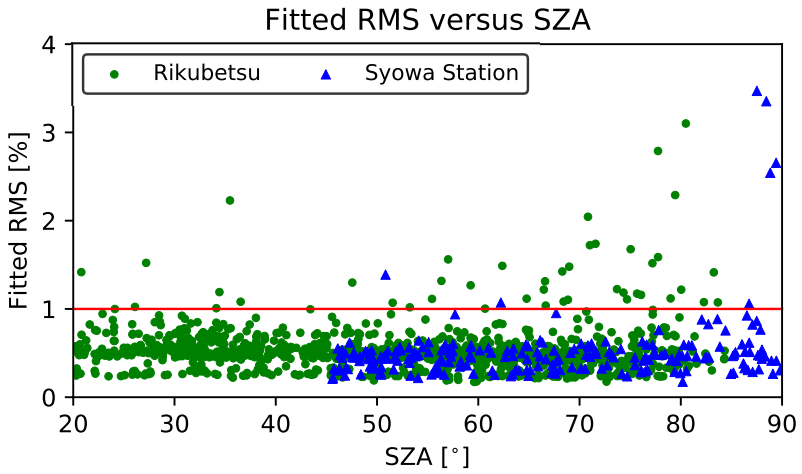

Figure 5.5: The fitted RMS residuals versus the SZA values on individual HCFC-22 retrieval. The observations at Rikubetsu and Syowa Station are shown by green circles and blue triangles, respectively.

sidered:

$$X_{\mathrm{HCFC-22}} = \frac{TC_{\mathrm{HCFC-22}}}{TC_{\mathrm{dry}}} = \frac{TC_{\mathrm{HCFC-22}}}{\frac{p_{\mathrm{s}} N_{\mathrm{A}}}{g m_{\mathrm{dry}}} - TC_{\mathrm{H_2O}} \frac{m_{\mathrm{H_2O}}}{m_{\mathrm{dry}}}} \tag{5.2}$$

where $TC_{\mathrm{HCFC-22}}$, TC_{dry}, and $TC_{\mathrm{H_2O}}$ are the FTIR-retrieved HCFC-22 total column, the dry-air total column, and the a priori (pre-retrieved) H_2O total column, respectively; p_{s} is the surface pressure calculated from the NCEP reanalysis; N_{A} is Avogadro's constant; g is the column-averaged acceleration; m_{dry} and $m_{\mathrm{H_2O}}$ are the mean molecular masses of dry-air and H_2O, respectively. Finally, we calculated the monthly mean column-averaged $X_{\mathrm{HCFC-22}}$ at both sites.

AGAGE in-situ measurements

The AGAGE observation network started HCFC-22 in-situ measurements at Cape Grim, Tasmania, in 1998 using a GC-MS with an adsorption-desorption system (GC-MS-ADS) which can measure a wide range of HCFCs, HFCs, methyl halides, and the halons (Simmonds et al, 1995; Prinn et al., 2000; O'Doherty et al., 2004; Miller et al., 2008). The GC-MS-ADS was already installed at Mace Head, Ireland (55.3°N, 9.9°W), in October 1994, but the HCFC-22 measurements were available after 1999. After 2003, the GC-MS-Medusa (for detail, see Section 5.1) instrument was sequentially placed at all AGAGE stations. These GC-MS-Medusa instruments extend the number of gases measured to 40 species and doubled the frequency of measurements. As a result of these improvements, the GC-MS-ADS instruments at Mace Head and Cape Grim were retired in December 2004.

Here, I use the in-situ measurement datasets of HCFC-22 at Mace Head (MHD) and Cape Grim (CGO) to compare with the FTIR-retrieved HCFC-22 data at Rikubetsu and Syowa Station. Note that these datasets include the GC-MS-ADS data before 2003, taken from `https://agage2.eas.gatech.edu/data_archive/agage/gc-ms/complete/`, and the GC-MS-Medusa data since 2004, taken from `https://agage2.eas.gatech.edu/data_archive/agage/gc-ms-medusa/complete/`. The HCFC-22 abundances at all AGAGE stations are reported relative to SIO-05 primary calibration scales, in dry-air mole fractions, and the absolute accuracies were liberally estimated to be ±1% (Simmonds et

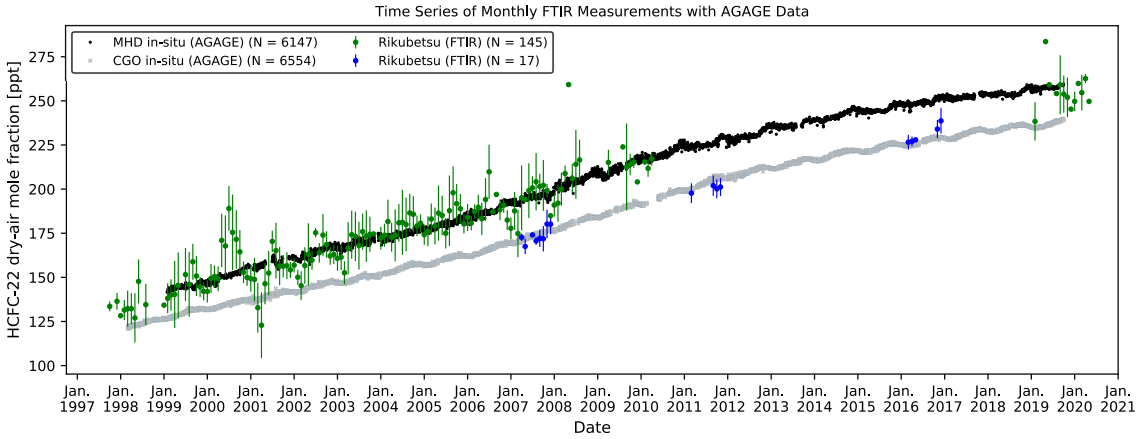

Figure 5.6: Time-series of the monthly mean FTIR-retrieved $X_{\mathrm{HCFC-22}}$ at Rikubetsu and Syowa Station, along with the AGAGE in-situ measurements at MHD and CGO.

al., 2018a). I removed polluted measurements using the pollution flags (P) embedded in the datasets and then calculated daily median mole fractions.

5.2.2 Time-series and seasonal variation

Figure 5.6 shows the time-series of the monthly mean FTIR-retrieved $X_{\mathrm{HCFC-22}}$ at Rikubetsu and Syowa Station, along with the dry-air mole fractions from the AGAGE in-situ measurements at MHD and CGO. The error bar on each monthly mean $X_{\mathrm{HCFC-22}}$ is a 1σ standard deviation around the monthly mean. The FTIR-retrieved $X_{\mathrm{HCFC-22}}$ data at Rikubetsu are in good agreement with the dry-air mole fraction data at MHD. Also, the $X_{\mathrm{HCFC-22}}$ data at Syowa Station are consistent with the dry-air mole fraction data at CGO.

Monthly mean de-trended $X_{\mathrm{HCFC-22}}$ values and 1σ standard deviations at Rikubetsu

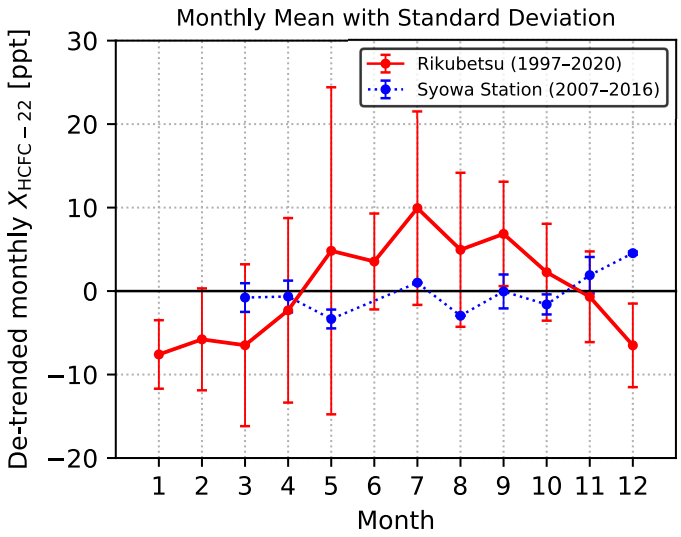

Figure 5.7: Seasonal cycles of the FTIR-retrieved $X_{\mathrm{HCFC-22}}$ at Rikubetsu for the 1997–2020 period and at Syowa Station for the 2007–2016 period.

and Syowa Station are shown in Figure 5.7. The monthly mean de-trended $X_{\mathrm{HCFC-22}}$ at Rikubetsu clearly show the seasonal cycle with a minimum during winter and a maximum during summer (approximately 18 ppt peak-to-peak amplitude). In contrast, the monthly mean de-trended data at Syowa Station have no or slightly seasonal cycle. Several factors could account for the observed seasonal cycles: seasonal variability in the regional emissions, changes in atmospheric oxidation (through the reaction with active OH radicals), and seasonal changes in atmospheric transport.

Xiang et al. (2014) suggests that there are major emission sources in the northern hemisphere, and that refrigerators and air conditioners may leak more in summer than in winter due to higher internal system pressure and more frequent use, both associated with higher ambient temperature in summer. However, we can not see significant seasonal

cycles in the time-series of the in-situ measurements at the AGAGE remote sites. This is explained by a summertime balance between the increasing HCFC-22 emissions and the removal process by OH radicals increasing in summer. Conversely, it is assumed that the effect of the increasing emissions in summer appears at site closed to major emission sources. Therefore, the peak at Rikubetsu during spring–summer may be caused by this. In addition, the de-trended data at Rikubetsu in early summer, especially in May, have a large 1σ standard deviation (spread of about $\pm$20 ppt). As mentioned in Section 5.1.2, the air masses arriving above Rikubetsu during spring–summer maybe affected by the regional pollution from Asia.

Chirkov et al. (2016) compared mean upper tropospheric mixing ratios retrieved from the satellite-borne Michelson Interferometer for Passive Atmospheric Sounding (MIPAS) to the AGAGE in-situ measurements, and indicated that the time series of the MIPAS observations in mid-latitudes have a pronounced seasonal cycle with a minimum in early spring, in contrast with the in-situ data in mid-latitudes. It was assumed that the seasonal cycle was caused by the intrusion of HCFC-22-poor stratospheric air at the upper troposphere and lower stratosphere (UTLS) at the time of the polar vortex breakdown (early spring). Also, they indicated that seasonal cycle is more pronounced in the northern hemispheric mid-latitudes than in the southern hemispheric mid-latitudes. This is well consistent with the annual cycles at Rikubetsu.

Figure 5.6 shows that there is the significant minimum peak at Rikubetsu in early spring in 2001. In order to investigate the effect by the intrusion of stratospheric air, I used

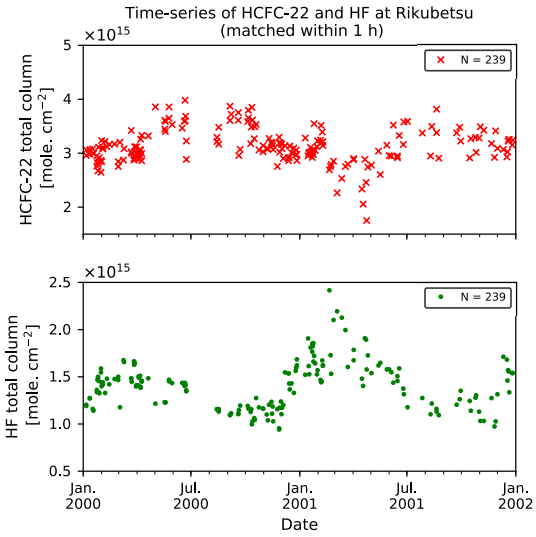

Figure 5.8: Time-series of the HCFC-22 (upper panel) and HF (lower panel) total columns at Rikubetsu in the 2000–2001 period. The individual HF observation is paired with the HCFC-22 retrieved within a hour.

the FTIR-retrieved hydrogen fluoride (HF) dataset at Rikubetsu which was downloaded from the NDACC web site (`http://www.ndaccdemo.org/stations/rikubetsu-japan`). HF is the dominant reservoir of stratospheric fluorine due to extremely stable against chemical loss. According to the zonal mean of HF volume mixing ratios derived from the satellite observations of the HALogen Occultation Experiment (HALOE) reported by Harrison et al. (2016), it is shown that the higher latitude and height, the greater HF volume mixing ratio is observed. On the other hand, the higher latitude and height, the lower HCFC-22 volume mixing ratio is generally, for the air above the upper troposphere (Chirkov et al., 2016). Figure 5.8 shows the time-series of the HF total columns at Rikubetsu for the 2000–2001 period, along with the corresponding HCFC-22 total column

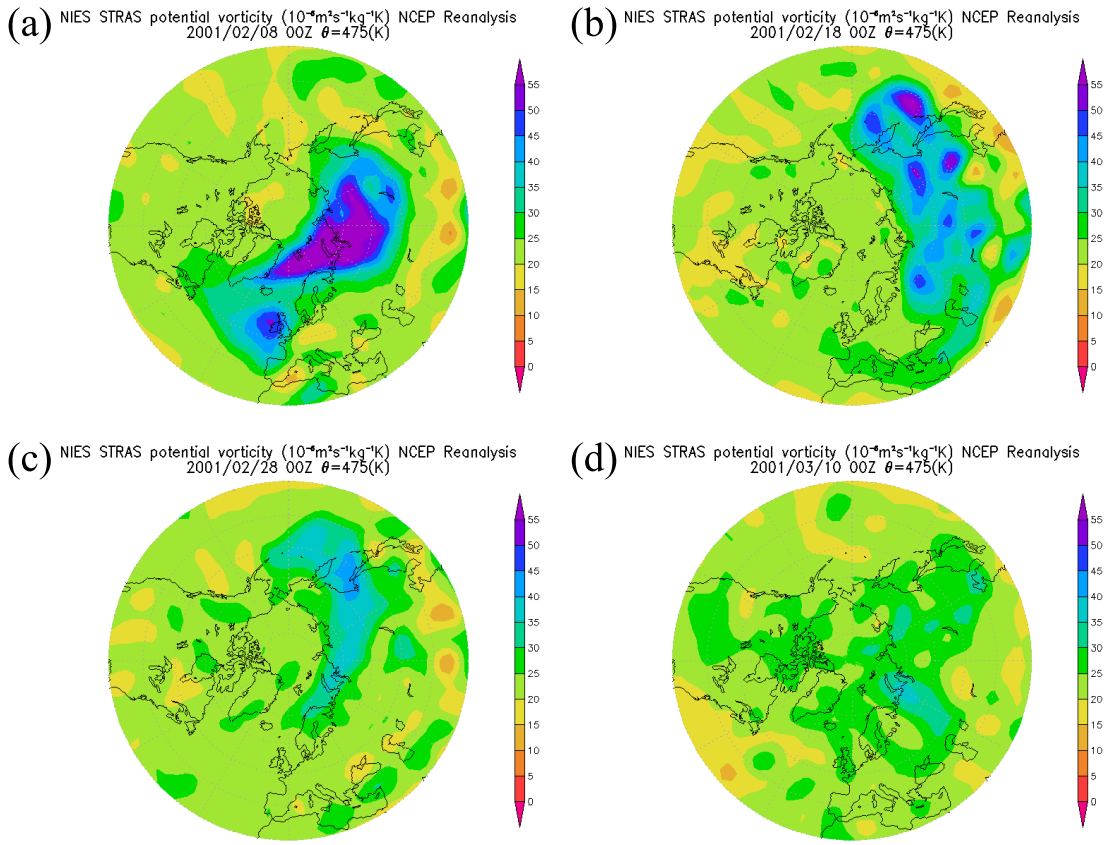

Figure 5.9: Maps of potential vorticity at a potential temperature of 475 K on 8 February (a), on 18 February (b), 28 February (c), and on 10 March 2001 (d) derived from NCEP reanalysis data. These maps were provided by CGER of NIES.

time-series. The HF total columns at Rikubetsu typically show a maximum peak around 1.5×10^{15} molecule cm^{-2} in each early spring, but the HF peak in the 2001 early spring was pronounced, exceeding 2.0×10^{15} molecule cm^{-2}. As shown in Harrison et al. (2016), no large seasonal variation of HF abundances in the stratosphere appeared in the 2001 early spring. Considering the report, it is suggested that the rapid decrease of HCFC-22 abundances were observed through the intrusion of stratospheric air mass into the troposphere above Rikubetsu.

From here, the minimum of HCFC-22 and the enhancement of HF are analyzed from an atmospheric physics perspective. The potential vorticity (PV) is a physical quantity defined as

$$PV = \frac{\zeta_{\mathrm{a}} \nabla \theta}{\rho} \tag{5.3}$$

where ζ_{a} is the absolute vorticity, ρ is the air density, and $\nabla\theta$ is the gradient of potential temperature. Because the stratification is substantially conserved in the absence of diabatic heating (such as latent heat released from condensation of water vapor) or friction, PV is generally conserved. Moreover, it is well-known that the absolute value of PV inside the region surrounded by the Polar night jet stream of the stratosphere is relatively high compared to the outside. Therefore, PV is very useful as the tracer of polar air mass. Figure 5.9 shows the maps of PV at a potential temperature of 475 K (altitude of approximately 19 km) on 8 February (a), on 18 February (b), 28 February (c), and on 10 March 2001 (d). These maps were provided by the STRAS (Stratosphere-Troposphere

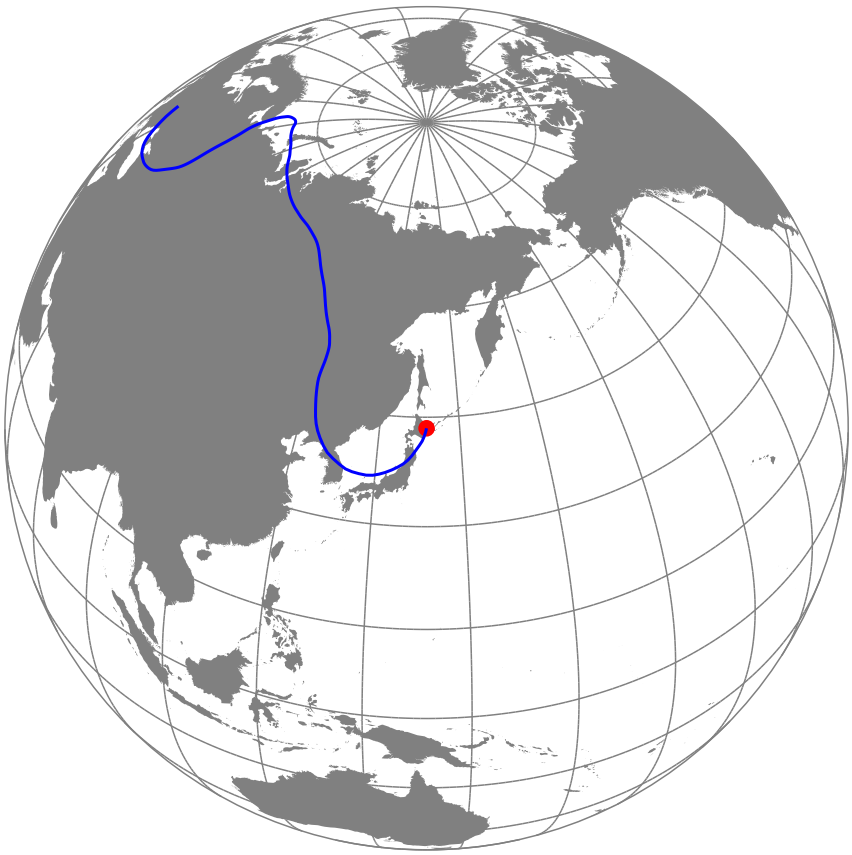

Figure 5.10: 10-day backward trajectory of the air mass arrived at 8000 m above Rikubetsu at 1:00 UTC on 5 March 2001.

Research Assisting System, `https://db.cger.nies.go.jp/gem/stras/en/index.html`) of the Center for Global Environmental Research (CGER) of NIES. The air mass having relatively high value of PV had intermittently reached at Rikubetsu for the period from the late February to the early March. Figure 5.10 depicts the isentropic 10-day backward trajectory calculated for the air mass arrived at 8000 m above Rikubetsu on 5 March 2001, using the Meteorological Data Explorer (METEX) developed at the CGER of NIES (Zeng et al., 2003). Calculation of the backward trajectory uses the meteorological data from the NCEP Climate Forecast System with a 3-hour time resolution, a horizontal resolution of $0.5^\circ \times 0.5^\circ$, and 37 vertical levels. The trajectory indicates that the air mass on the day came from the higher latitude and altitude in Arctic region. Therefore, it is implied that the FTIR-retrieved HCFC-22 amounts during the minimum event were affected by the polar stratospheric air.

In case of the HFC-23 retrievals as mentioned in Section 5.1.2, the air masses arrived at Rikubetsu over the period between spring and summer were affected by pollution emitting from East Asia, whereas the observations at Rikubetsu in the period from December to February (DJF) represent the background air at the site. In Section 5.2.3, the trends for the $X_{\mathrm{HCFC-22}}$ data are calculated and are compared with the AGAGE datasets. For trend calculation from the FTIR-retrieved data at Rikubetsu, hence, the $X_{\mathrm{HCFC-22}}$ data in DJF are used.

Table 5.2: HCFC-22 annual change rates and standard errors computed from monthly mean $X_{\mathrm{HCFC-22}}$ at Rikubetsu and Syowa Station and the AGAGE in-situ measurements at MHD and CGO, in ppt year^{-1}.

Annual change [ppt year^{-1}]	1999–2003	2004–2010	2007–2016	2010–2019
Rikubetsu (FTIR)	5.33 ± 1.02	7.10 ± 0.70	–	4.32 ± 0.86
Syowa Station (FTIR)	–	–	6.46 ± 0.19	–
MHD (AGAGE in-situ)	6.32 ± 0.03	7.77 ± 0.02	5.88 ± 0.02	4.30 ± 0.01
CGO (AGAGE in-situ)	4.93 ± 0.02	6.94 ± 0.01	6.06 ± 0.02	4.42 ± 0.01

5.2.3 Trend of atmospheric HCFC-22

Table 5.2 lists the HCFC-22 annual change rates computed from the monthly FTIR-retrieved $X_{\mathrm{HCFC-22}}$ datasets at Rikubetsu and Syowa Station and the AGAGE in-situ measurement datasets at MHD and CGO. The columns of Table 5.2 represent the annual change rate in the periods of 1999–2003, 2004–2010, 2007–2016, and 2010–2019. The individual annual change rate was simply calculated by linear regression in disregard of any seasonal cycles. The uncertainty represents the standard error of the slope estimation. The annual change rate for the 1999–2003 period at Rikubetsu (5.33 ± 1.02 ppt year^{-1}) is lower than that at MHD (6.32 ± 0.03 ppt year^{-1}). This is caused by the high peak of the $X_{\mathrm{HCFC-22}}$ at Rikubetsu in the 2000 summer. For the 2004–2010 period, the annual change rate at Rikubetsu (7.10 ± 0.70 ppt year^{-1}) is lower than that at MHD (7.77 ± 0.02 ppt year^{-1}), but there is a consistency between both change rates considering the uncertainty of the change rate at Rikubetsu. The annual change rates at all sites increase

dramatically after 2004. The increasing trends accelerated globally since 2004 are well consistent with the report of Montzka et al. (2009).

For the 2007–2016 period, the annual change rate at Syowa Station (6.46 ± 0.19 ppt year^{-1}) is higher than the ones at MHD (5.88 ± 0.02 ppt year^{-1}) and CGO (6.06 ± 0.02 ppt year^{-1}). Although before 2010 the change rate at MHD is consistently higher than that at CGO, the situation is reversed over the considering period. This indicates that the HCFC-22 emissions in the northern hemisphere decrease during the period of 2007–2016 and that the effect by decreasing the emissions does not yet propagate to the Antarctica. For the 2010–2019 period, the annual change rate at Rikubetsu (4.32 ± 0.86 ppt year^{-1}) is in good agreement with that at MHD (4.30 ± 0.01 ppt year^{-1}). The differences between the trends in the northern hemisphere and southern hemisphere are very small. This implies that the HCFC-22 emissions in the northern hemisphere have been continuously decreasing.

Based on the above, the trends of the FTIR-retrieved HCFC-22 in this study agree with those derived from the AGAGE datasets, considering the errors. This indicates that it is possible to well monitor the long-term trends of HCFC-22 together with other FTIR observation sites such as Jungfraujoch (Prignon et al., 2019).

5.3 Correlation between HFC-23 and HCFC-22

In Section 5.1.2 and Section 5.2.2, the time-series of the atmospheric HFC-23 and HCFC-22 retrieved from the FTIR measurements at Rikubetsu show the seasonal cycles with a maximum peak in early summer. A part of the reasons for the high abundances of HFC-23 and HCFC-22 may be atmospheric transport of Asian pollution. To examine the origins and transport pathways of air masses arriving at Rikubetsu, here, I carry out backward trajectory analysis. An isentropic 10-day backward trajectory is calculated for each air mass at the time of the FTIR observation of HCFC-22 using the METEX developed at the CGER of NIES (Zeng et al., 2003), as mentioned in Section 5.2.2. Calculation of the backward trajectory uses the meteorological data from the NCEP Climate Forecast System with a 3-hour time resolution, a horizontal resolution of $0.5^{\circ} \times 0.5^{\circ}$, and 37 vertical levels. For each FTIR observation, I calculate backward trajectories at four altitudinal levels (i.e. 2000, 4000, 6000, and 8000 m).

As mentioned in Section 1.5, HCFC-22 has been widely used (e.g. refrigerants, foaming agents). In contrast, atmospheric HFC-23 is mainly caused by ventilations from production plants of HCFC-22. As a potential source region for the enhancement cases, it is possible to assume the East Asia. Especially, the recent HFC-23 emissions since 2000 in the East Asia region are dominantly caused by the HCFC-22 manufactories in China because HCFC-22 manufactories in Japan, South Korea, and Taiwan equip an incineration system of un-wanted HFC-23. Li et al. (2011) investigated the originations of air masses

arrived at Gosan, South Korea, for the period from November 2007 to December 2008, with backward trajectory analysis with a tracer method based on the relative ratio of the enhancements of HFC-23 (ΔHFC-23) to those of HCFC-22 (ΔHCFC-22). Their study founds statistically significant correlations with ΔHCFC-22 for ΔHFC-23. The ΔHFC-23/ΔHCFC-22 ratio of air mass originating from China shows higher value than 0.08. In contrast, the ΔHFC-23/ΔHCFC-22 ratios of air masses originating from South Korea, Taiwan, and Japan are significantly lower value than 0.08.

The 10-day backward trajectories of the air masses arriving at 2000, 4000, 6000, and 8000 m above ground level at Rikubetsu were calculated for the times of the FTIR observations between 1998 and 2020. Figure 5.11, 5.12, 5.13, and 5.14 show the trajectories calculated from level of 2000, 4000, 6000, and 8000 m, respectively, but not shown the trajectories in 2010, 2019, and 2020 due to small number of trajectories. The majority of the air masses arriving at any altitude for each year came mainly from the northwest direction (Siberia), but sometimes from the southwest direction (East Asia). In order to classify the air mass of Chinese origin, I selected the trajectories that passed through the following spatial region, CN (area surrounded by red dashed-line in Figure 5.11): latitudinal range of 20°N–45°N, longitudinal range of 110°E–125°E, and altitudinal range of 0–1500 m (boundary layer defined in this study). Table 5.3 lists the number of the air masses passed through CN region and the percentage relative to the total number of trajectories calculated in the period between March and November for each year. Also, the number of the air masses passed through CN region and the relative ratio in winter (between

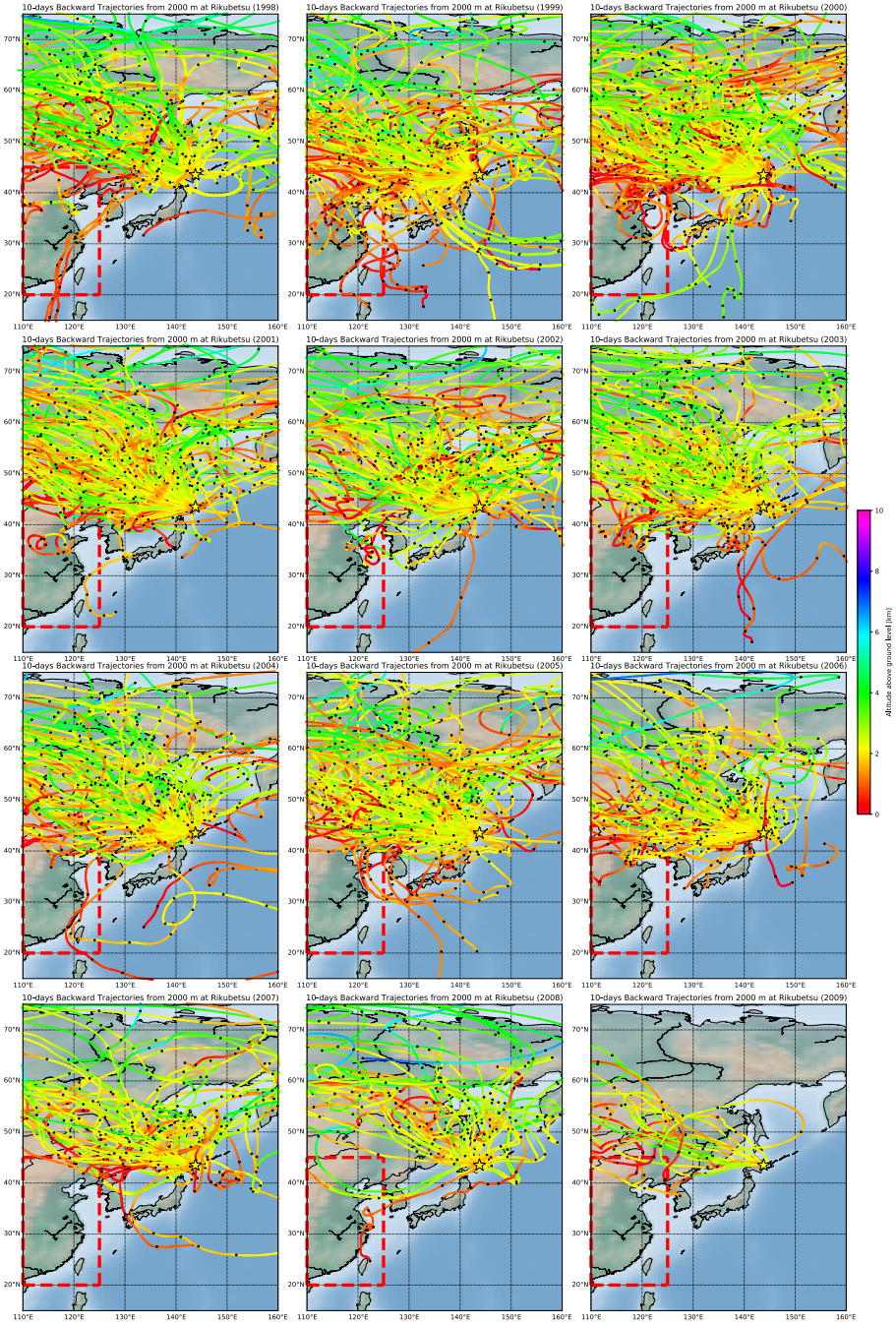

Figure 5.11: 10-day backward trajectories of the air masses arriving at 2000 m above ground level at Rikubetsu at the times of the FTIR observations between 1998 and 2009. Each point on the trajectories is color-coded by altitude above ground level.

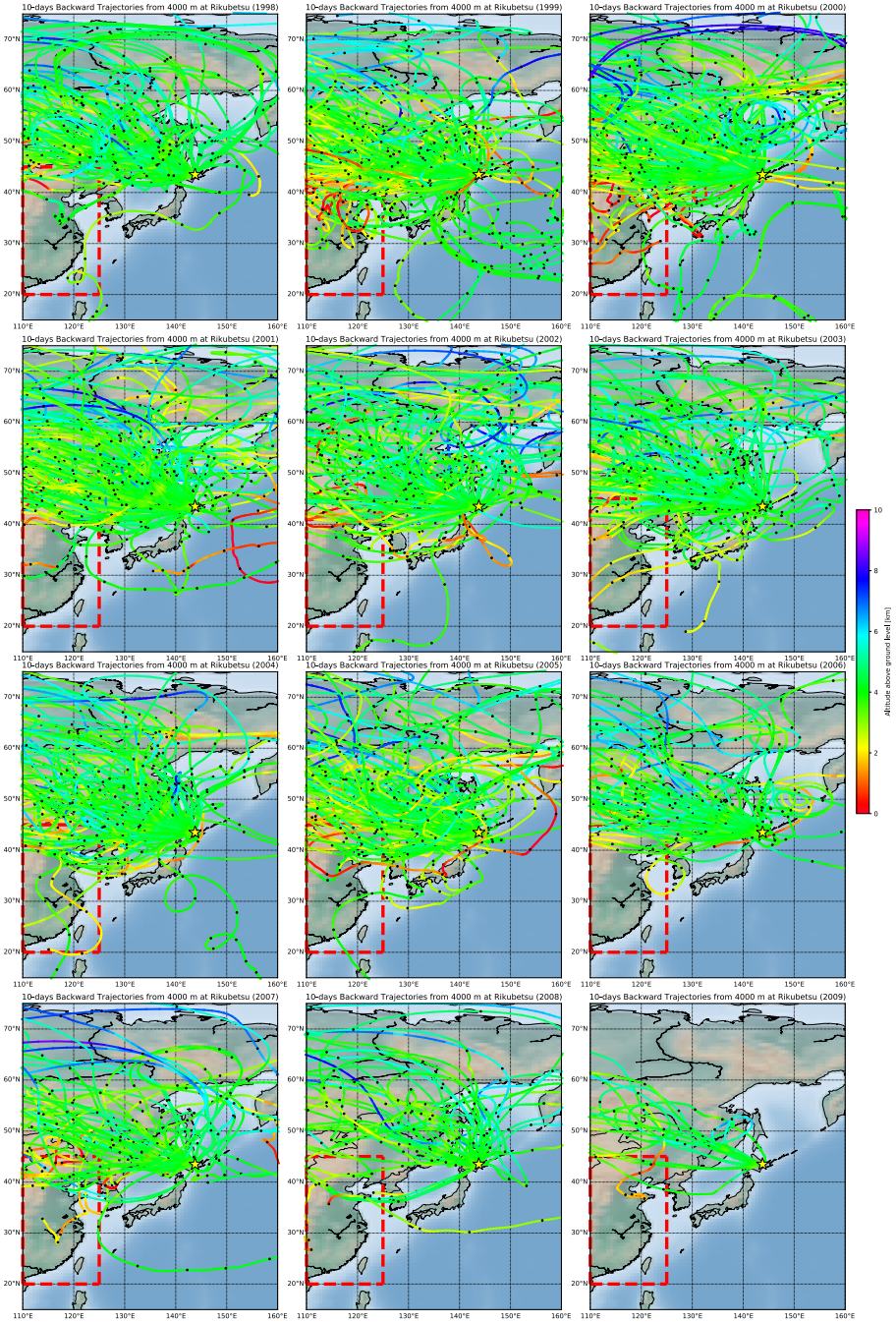

Figure 5.12: Same as Figure 5.11, but for the air masses arriving at 4000 m above ground level at Rikubetsu.

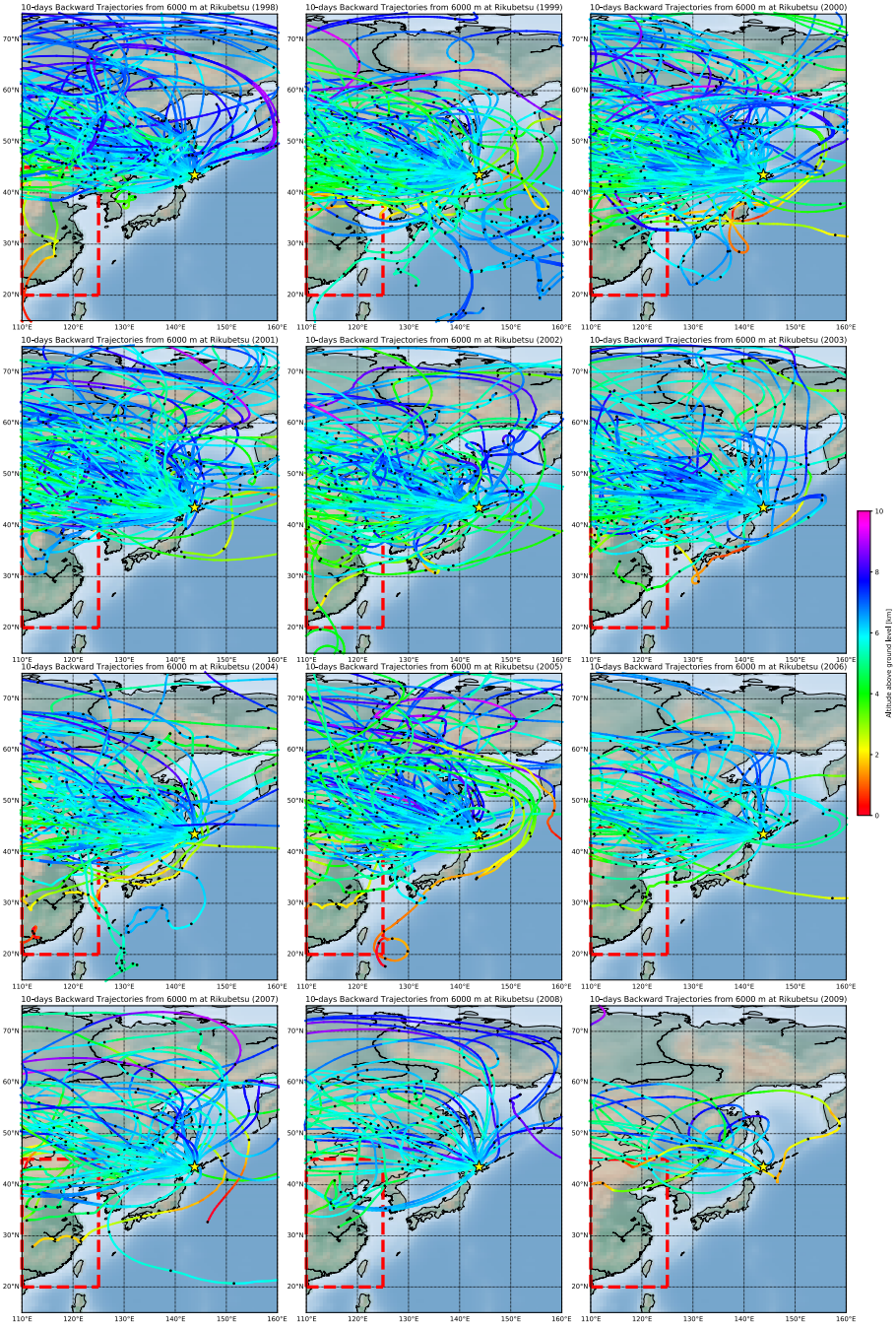

Figure 5.13: Same as Figure 5.11, but for the air masses arriving at 6000 m above ground level at Rikubetsu.

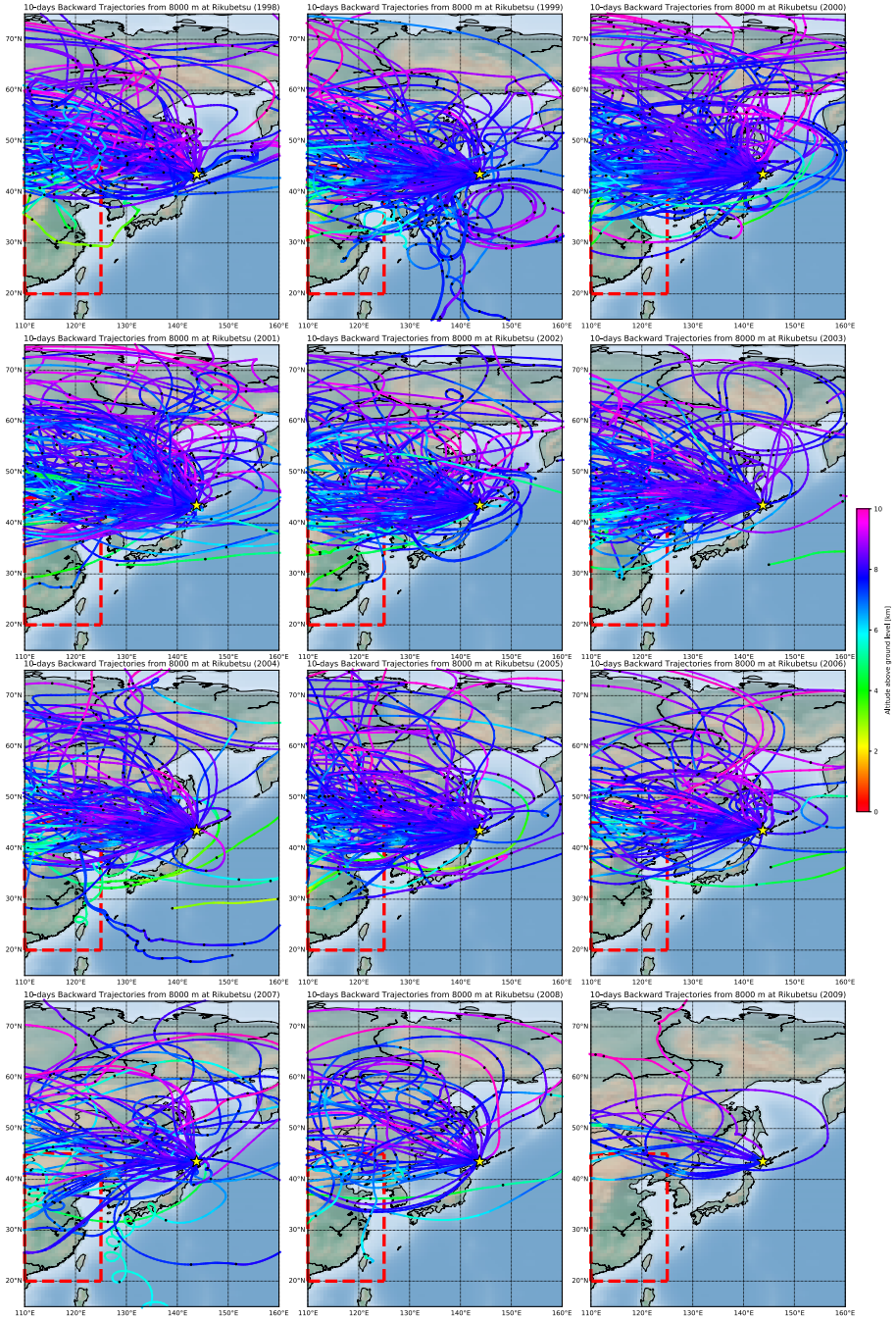

Figure 5.14: Same as Figure 5.11, but for the air masses arriving at 8000 m above ground level at Rikubetsu.

December and February) are listed in Table 5.4. Note that the number of trajectories for the initial altitude of 8000 m is not listed in Table 5.3 and Table 5.4 because the air masses arrived at 8000 m have no trajectory which passed through CN region. Basically, the number of the air masses passed through CN region between March and November is obviously larger than in winter at any initial altitude. The relative percentages of the air masses passed through CN region arrived at 2000 m above Rikubetsu are higher in the period from March to November than in winter, except for ones in 2002, 2005, 2006, 2009. The relative percentages of the air masses originated from CN region arrived at 4000 m above Rikubetsu are higher in the period from March to November than in winter, except for ones in 2002, 2004, 2005, 2006, 2008. Consequently, it is implied that the seasonal cycles of $X_{\mathrm{HFC-23}}$ and $X_{\mathrm{HCFC-22}}$ as shown in Figure 5.3 and 5.7 were induced from effect by Chinese emissions of HFC-23 and HCFC-22.

Table 5.3: Number of air masses passed through CN region and percentage relative to total number of trajectories for the period between March and November for each year. The first column represents the initial altitudes set for calculating backward trajectories.

Initial altitude	Year 1998	1999	2000	2001	2002	2003	2004	2005	2006	2007	2008	2009	2010	2019	2020
2000 m	10	27	24	6	5	10	11	11	8	7	2	3	0	1	1
	12.5%	26.5%	23.5%	7.9%	7.9%	13.3%	17.2%	14.3%	23.5%	15.2%	7.1%	21.4%	0%	7.1%	16.7%
4000 m	2	13	12	3	3	1	1	2	0	6	1	1	0	1	0
	2.5%	12.8%	12.6%	4.0%	4.8%	1.3%	1.6%	2.6%	0%	13.0%	3.6%	7.1%	0.0%	7.1%	0.0%
6000 m	0	2	1	0	0	1	0	2	0	1	0	1	0	0	0
	0.0%	2.0%	1.1%	0.0%	0.0%	1.3%	0.0%	2.6%	0.0%	2.2%	0.0%	7.1%	0.0%	0.0%	0.0%
Number of total trajectories for each altitude	80	102	95	76	63	75	64	77	34	46	28	14	6	14	6

Table 5.4: Same as Table 5.3, but for the period between December and February for each year.

Initial									Year									
altitude	1998	1999	2000	2001	2002	2003	2004	2005	2006	2007	2008	2009	2010	2019	2020
2000 m	3	3	5	4	5	1	2	4	10	1	0	1	0	0	0
	12.0%	12.5%	9.1%	7.4%	16.1%	3.9%	9.1%	16.7%	34.5%	11.1%	0.0%	100.0%	0.0%	0.0%	0.0%
4000 m	0	3	0	2	4	0	2	1	1	0	1	0	0	0	0
	0.0%	12.5%	0.0%	3.7%	12.9%	0.0%	9.1%	4.2%	3.5%	0.0%	9.1%	0.0%	0.0%	0.0%	0.0%
6000 m	3	1	0	0	0	0	2	0	0	0	0	1	0	0	0
	12.0%	4.2%	0.0%	0.0%	0.0%	0.0%	9.1%	0.0%	0.0%	0.0%	0.0%	100.0%	0.0%	0.0%	0.0%
Number of total trajectories for each altitude	25	24	55	54	31	26	22	24	29	9	11	1	1	7	3

Following the study of Li et al. (2011), I investigated the correlation between ΔHCFC-22 and ΔHFC-23 retrieved from the FTIR observations at Rikubetsu for the period from 1998 to 2009. In this study, ΔHCFC-22 and ΔHFC-23 at Rikubetsu are defined as the enhancements from the linear trend lines of the FTIR-retrieved $X_{\mathrm{HCFC-22}}$ and $X_{\mathrm{HFC-23}}$ in the period from December to February between 1998 and 2010. Figure 5.15 shows the correlations between the ΔHCFC-22 and ΔHFC-23 at Rikubetsu for each year from 1998 to 2009. The correlations for all years except 2000 are not significant due to the greater p-value than 5%. This is probably due to the small number of observation data, the large HFC-23 retrieval error relative to HCFC-22 retrieval error, and the trajectory passing only through the edge of CN region (e.g. the case in 2007 as shown in the lower left panel of Figure 5.11). On the other hand, a significant correlation ($p < 0.05$) is found only in 2000. Therefore, a part of the seasonal cycles of the $X_{\mathrm{HCFC-22}}$ and $X_{\mathrm{HFC-23}}$ at Rikubetsu in 2000 maybe caused by HCFC-22 and HFC-23 emissions from China.

The linear regression slope of the correlation between the ΔHCFC-22 and ΔHFC-23 (ΔHFC-23/ΔHCFC-22 ratio) is expected to reflect the emission ratios of these gases in source region if these gases are neither produced in nor removed from the air mass during transport. Following the studies of Palmer et al. (2003) and Yokouchi et al. (2006), I estimate the HFC-23 emission in CN region in 2000 based on the slope of the correlation. The emission rate of HFC-23 ($E_{\text{HFC-23}}$) is estimated by using the following equation:

$$E_{\text{HFC-23}} = E_{\text{ref}} \frac{\Delta\text{HFC-23}}{\Delta\text{HCFC-22}} \frac{m_{\text{HFC-23}}}{m_{\text{ref}}} \quad [\text{Gg year}^{-1}] \tag{5.4}$$

where E_{ref} is the reference HCFC-22 emission rate in source region and $m_{\mathrm{HFC\text{-}23}}$ and m_{ref} are the molecular masses of HFC-23 (70.0) and HCFC-22 (86.5), respectively. I selected the Chinese HCFC-22 emission rate of 12.1 Gg year^{-1} from Fang et al. (2018) as a reference emission rate in CN region in 2000. Considering the ΔHFC-23/ΔHCFC-22 ratio of 0.12 $\pm$ 0.04 at Rikubetsu in 2000, the estimated HFC-23 emission rate is 1.18 $\pm$ 0.39 Gg year^{-1}, which is 41.7% of the Chinese HFC-23 emission rate (2.83 Gg year^{-1}) in 2000 reported by Simmonds et al. (2018a). However, the HFC-23 emission estimated in this study does not cover the whole emissions in China because few air masses arriving at Rikubetsu passed through southern China. In other words, this result means that HFC-23 emission rate per unit area from the northern China in 2000 was about 40% relative to the emission rate for the whole China. This means that there are some emission sources of HFC-23 with higher emission rates in the southern than in the northern China. Based on the above, if there are many FTIR observations of air masses passing over the region considered for emission estimation, it would be possible to estimate more accurate HFC-23 emissions from the region.

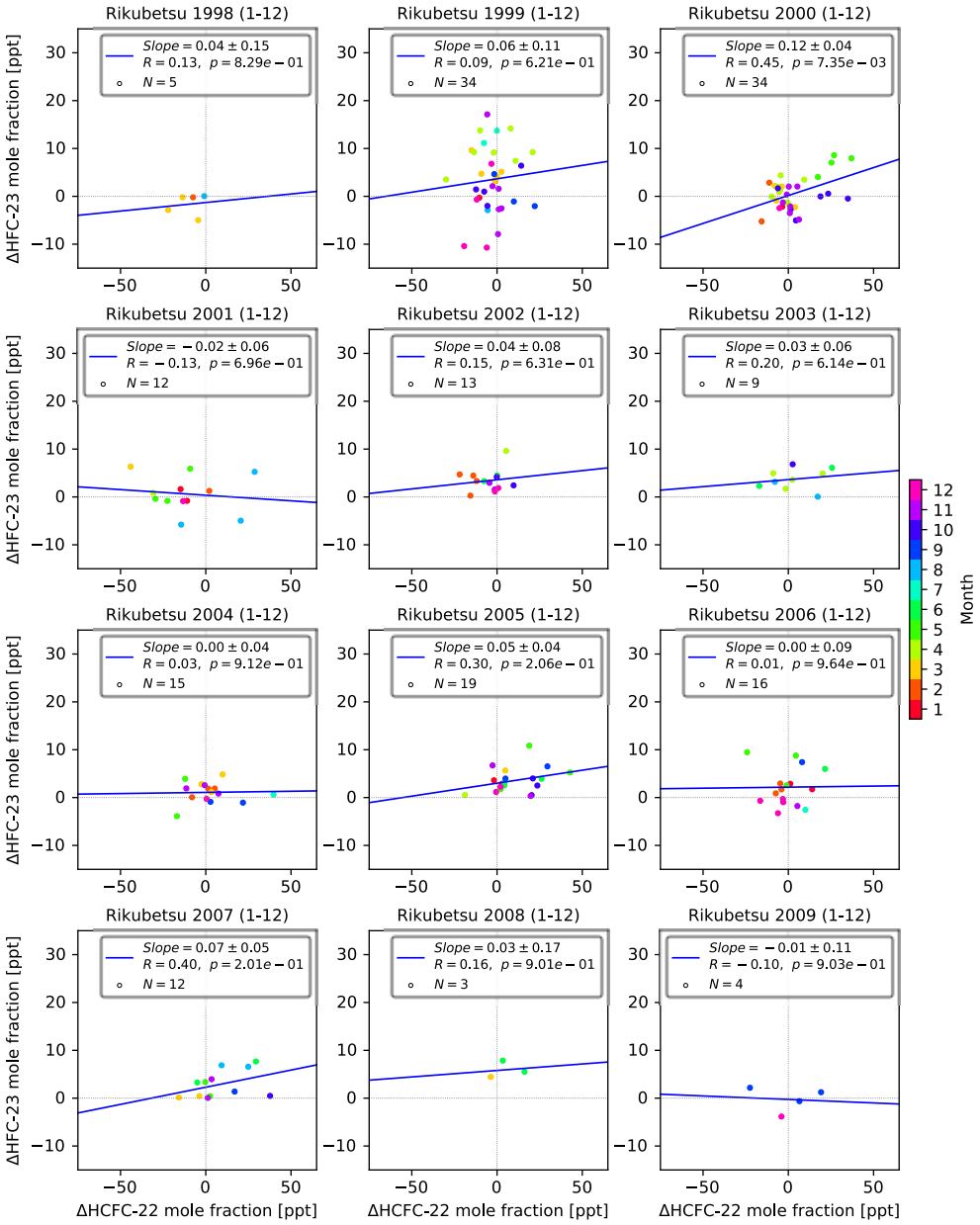

Figure 5.15: The correlations between ΔHCFC-22 and ΔHFC-23 at Rikubetsu for each year from 1998 to 2009. The color of each point represents the month of observation. The blue line is the linear regression slope. The slope value with standard error, correlation coefficient (R), p-value (p), and number of observations (N) are also shown in each panel.

Chapter 6

Conclusions

The first scientific goal of this study is to investigate the retrieval method of atmospheric HFC-23 which is very small amount in whole atmosphere. Moreover, this study includes retrieving atmospheric column abundance of HCFC-22 whose production activity is closely related with global emission of HFC-23 in order to evaluate the developed method of atmospheric HFC-23.

In Chapter 3, a procedure for retrieving atmospheric column abundances of HFC-23 with ground-based FTIR was developed, and the first HFC-23 retrievals were carried out using the solar MIR spectra taken from ground-based FTIRs at Rikubetsu (1997–2020) and Antarctic Syowa Station (2007–2016) with the SFIT4 retrieval software. The two retrieval micro-windows (1138.5–1148.0 cm^{-1} and 1154.0–1160.0 cm^{-1}), encompassing the ν_2 and ν_5 vibrational-rotational bands of HFC-23, were selected to avoid strong H_2O ab-

sorption lines at 1149.47 cm^{-1}, 1151.54 cm^{-1} and 1152.44 cm^{-1}. Significant interfering species in the micro-windows are O_3, N_2O, CH_4, H_2O, HDO, CFC-12, HCFC-22 and PAN. In particular, H_2O, HDO and CH_4 affect the HFC-23 retrievals. Due to large daily variabilities of H_2O and HDO in the atmosphere, those a priori profiles were pre-retrieved with the individual dedicated MWs (H_2O: 824.40–825.90 cm^{-1}, HDO: 1208.40–1209.10 cm^{-1}) for each observed spectrum and were then simply scaled in the subsequent HFC-23 retrievals. For a priori profiles of CH_4, a pre-retrieval with the dedicated MW of 1201.820–1202.605 cm^{-1} was carried out for each spectrum and then these CH_4 profiles were fixed in the subsequent HFC-23 retrievals in order to reduce the retrieval error resulting from competition between several weak absorptions of CH4 and the weak HFC-23 absorption. The HFC-23 retrieval in this study was typically sensitive to the atmospheric layer from the surface to the lower stratosphere. However, its DOFS was only 1, and only total column amount can be retrieved. The mean HFC-23 total columns retrieved from the observed spectra at Rikubetsu over the periods of 1997–2010 and 2019–20 were estimated as $(3.23 \pm 1.10) \times 10^{14}$ and $(5.64 \pm 0.59) \times 10^{14}$ molecules cm^{-2}, respectively. The mean HFC-23 total column at Syowa Station over the 2007–2016 period was $(3.69 \pm 1.35) \times 10^{14}$ molecules cm^{-2}.

The random and systematic retrieval errors for the FTIR-retrieved HFC-23 total columns were also estimated assuming four error components – the smoothing error, other retrieved parameter error, non-retrieved model parameter error, and measurement noise error. The retrieval random and systematic errors are 15% and 24% at Rikubetsu and

8.6% and 19% at Syowa Station, respectively. The random errors at both sites mainly come from measurement noise and CH_4 pre-retrieved profile uncertainty. The systematic errors at both sites are dominated by the uncertainty of the spectroscopic parameters, in particular the spectroscopic uncertainties of HFC-23, H_2O, HDO, and CH_4. The total error for the retrieved HFC-23 total columns at Rikubetsu and Syowa Station are 28% and 21%, respectively.

In Chapter 4, the retrievals of HCFC-22 from the solar MIR spectra measured at Rikubetsu and Syowa Station were performed following the retrieval strategy of Prignon et al. (2019). The retrieval MW covers the range of 828.75–829.40 cm^{-1} including the $2\nu_6$ band of HCFC-22. Major interfering gases in the MW are H_2O, CO_2, and O_3. In this study, the profiles of HCFC-22 and O_3 were retrieved, but those of H_2O and CO_2 were simply scaled. The HCFC-22 retrieval in this study was basically sensitive to troposphere and lower stratosphere, and its DOFS was only 1. The mean HCFC-22 total columns retrieved from the observations at Rikubetsu for the periods of 1997–2010 and 2019–2020 were $(3.35 \pm 0.51) \times 10^{15}$ and $(5.20 \pm 0.29) \times 10^{15}$ molecules cm^{-2}, respectively. The mean total column at Syowa Station for the 2007–2016 period was $(4.07 \pm 0.57) \times 10^{15}$ molecules cm^{-2}. The random and systematic retrieval errors are 5.6% and 5.0% at Rikubetsu and 3.2% and 5.0% at Syowa Station, respectively. The random and systematic retrieval errors at both sites are dominated by measurement noise and the uncertainty of the HCFC-22 line intensity parameter. These percentage are similar to the result of the error analysis reported by Prignon et al. (2019) which demonstrated the random error of

2.7% and the systematic error of 5.5% for the Bruker instrument at Jungfraujoch.

In discussion of this thesis, the column-averaged dry-air mole fraction data were derived from the FTIR-retrieved HFC-23 and HCFC-22 total columns at Rikubetsu and Syowa Station, and these data were used for comparison with the AGAGE datasets.

The time-series of the FTIR-retrieved HFC-23 columns at Rikubetsu and Syowa Station show obviously increasing trends. The FTIR-retrieved $X_{\mathrm{HFC-23}}$ at both sites were compared to AGAGE in-situ measurements at THD and CGO, CGAA samples filled at CGO, and results from the AGAGE 12-box model based on AGAGE measurements. The trends of $X_{\mathrm{HFC-23}}$ at Rikubetsu in DJF and Syowa Station are consistent with the trends derived from AGAGE data, but at Syowa Station there is a negative bias of 5 ppt (-25%) compared to the AGAGE in-situ measurements at CGO. The time-series of the FTIR-retrieved $X_{\mathrm{HFC-23}}$ at Rikubetsu has a seasonal cycle with a peak during spring to summer, but the $X_{\mathrm{HFC-23}}$ at Syowa Station did not show a significant cycle. We suggest that the seasonal cycle of HFC-23 at Rikubetsu is caused by the transport of HFC-23 emitted from East Asia and Eurasia. We found that the minimum of the seasonal cycle occurred from December to February and represented the background concentration of HFC-23 at Rikubetsu at that time. The negative bias at Rikubetsu in DJF was 3 to 4 ppt (-15% to -20%) compared to the AGAGE datasets. We showed that the bias occurred at both sites and were caused mostly by the spectroscopic parameter uncertainties of HFC-23, H_2O, HDO, and CH_4. Therefore, these molecules mostly affect the HFC-23 retrieval. ACE-FTS HFC-23 measurements also showed a negative average difference of

5% compared with the AGAGE 12-box model. A solution for this bias problem may be found in new high-resolution laboratory spectra of HFC-23 measured under the atmospheric conditions of the lower troposphere, leading to an expected improvement of the HFC-23 spectroscopic parameters and HFC-23 retrievals.

The annual growth rate of the $X_{\mathrm{HFC-23}}$ at Rikubetsu in DJF over the periods of 1997–2009 and 2008–2019 were 0.810 ± 0.093 and 0.928 ± 0.108 ppt year^{-1}, respectively, which are in good agreement with the trend derived from the AGAGE datasets over the same periods. The annual growth rate at Syowa Station is 0.819 ± 0.071 ppt year^{-1} over the 2007–2016 period, which is also consistent with the trend from the AGAGE datasets over the same period. The trend derived from the $X_{\mathrm{HFC-23}}$ data retrieved with our retrieval strategy agreed with other ground-based in situ measurements.

The time-series of the FTIR-retrieved HCFC-22 columns at Rikubetsu and Syowa Station clearly show that there are the increasing trends of the retrieved total columns at both sites. To compare with the FTIR-retrieved HCFC-22 data at Rikubetsu and Syowa Station, the AGAGE in-situ measurement datasets of HCFC-22 at CGO and MHD were used in this study. The FTIR-retrieved $X_{\mathrm{HCFC-22}}$ data at Rikubetsu are in good agreement with the dry-air mole fraction data at MHD, and the $X_{\mathrm{HCFC-22}}$ data at Syowa Station are consistent with the data at CGO. The $X_{\mathrm{HCFC-22}}$ data at Rikubetsu, however, have a large seasonal variability with a minimum during winter and a maximum during summer, which is approximately 18 ppt peak-to-peak amplitude. In contrast, the $X_{\mathrm{HCFC-22}}$ data at Syowa Station have no significant variability. The seasonal cycle at Rikubetsu is probably

affected by seasonal variability of regional emissions and of atmospheric transport. The seasonal cycle probably comes from that HCFC-22 emission in the northern hemisphere may raise in summer due to leak from refrigerators and air conditioners, and that the air masses arriving above Rikubetsu during spring–summer maybe affected by the regional pollution from Asia. In the trend analysis of Section 5.2.3, therefore, the $X_{\mathrm{HCFC-22}}$ data in the period of DJF were used for calculating annual changes at Rikubetsu. On the other hand, all the retrieval data at Syowa Station were used to estimate the annual changes. The annual change rate at Rikubetsu over the period of 1999–2003, 2004–2010, and 2010–2019 are 5.33 ± 1.02, 7.10 ± 0.70, and 4.32 ± 0.86 ppt year^{-1}, respectively. Considering the uncertainty of each annual change rate, these are in agreement with the change for the AGAGE in-situ data at MHD. The annual change rate at Syowa Station over the 2007–2016 period is 6.46 ± 0.19 ppt year^{-1}, which is higher than that for the AGAGE in-situ data at CGO. This indicates that the HCFC-22 emissions in the northern hemisphere decrease during the period of 2007–2016 and that the effect by decreasing the emissions does not yet propagate to the Antarctica.

In this study, it has been demonstrated that the $X_{\mathrm{HFC-23}}$ and $X_{\mathrm{HCFC-22}}$ retrieved from the FTIR measurements at Rikubetsu have a seasonal pattern with a maximum peak in summer. Considering the previous study in regard with atmospheric tracer gases coming from anthropogenic uses of fossil fuel, it is suggested that these seasonal cycles maybe affected by some atmospheric transport from some major anthropogenic sources in East Asia. Therefore, in Section 5.3, backward trajectory analysis was executed for

all the dates of the FTIR observations at Rikubetsu using the METEX program, and the origins and transport passways of air masses arriving at Rikubetsu were investigated. According to previous study, the recent HFC-23 emissions in the East Asia region are dominantly caused by the HCFC-22 productions in China. In this study, the trajectories passed through altitude level of 0–1500 m above China were selected for the analysis, the percentage of air masses transported from China against all the trajectories was calculated for each year. As the result, it is indicated that the percentage during March–November is basically higher than that in winter. Also, the percentage of air masses from China is relatively high for the year when the observation frequency was high. This suggests that if the frequency of FTIR observation at Rikubetsu is increased, we could measure the air masses from the large emission sources.

Following the analysis method of Li et al. (2011), a correlation between the enhancements of HFC-23 and HCFC-22 was investigated for each year. In this study, it is verified that only the enhancements of HFC-23 and HCFC-22 at Rikubetsu in 2000 have a significant relationship at the 95% confidence level. Furthermore, it is possible to estimate annual HFC-23 emission rate along the trajectories in 2000 from the correlation coefficient, using the estimation method of Palmer et al. (2003) and Yokouchi et al. (2006). When the Chinese HCFC-22 emission rate of 12.1 Gg year^{-1} in 2000 reported by Fang et al. (2018) and the enhancement ratio of 0.12 at Rikubetsu in 2000 are used, the HFC-23 emission rate in China is estimated at 1.18 ± 0.39 Gg year^{-1}. This value is about 40% of the Chinese HFC-23 emission rate in 2000 reported by Simmonds et al. (2018a). Be-

cause there are only a few air masses passed through the southern China in 2000, this result suggests that HFC-23 emission rate per unit area from the northern China was approximately 40% relative to the emission rate for the whole China. Combined the FTIR observations of HFC-23 with those of HCFC-22, it is possible to estimate the origination of the FTIR-retrieved HFC-23.

This thesis demonstrates that ground-based FTIR measurements are capable of monitoring the long-term trends of HFC-23 and HCFC-22. Furthermore, it is shown that there is a possibility we can estimate regional emission of HFC-23 combining the ground-based FTIR measurement data of HFC-23 and HCFC-22. If the FTIR measurement techniques of atmospheric HFC-23 developed in this study was extended to other NDACC ground-based FTIR sites around world, the measurements reported from these sites would complement the global AGAGE observations by filling spatial and temporal gaps and may lead to improved insights about changes in regional and global emissions of HFC-23 and its role in global warming.

References

[1] Arnold, T., Mühle, J., Salameh, P. K., Harth, C. M., Ivy, D. J., and Weiss, R. F.: Automated measurement of nitrogen trifluoride in ambient air, Anal. Chem., 84, 4798–4804, 2012.

[2] Bell, R.: Introductory Fourie Transform Spectroscopy, Academic Press, 1972.

[3] Brown, A. T., Chipperfield, M. P., Boone, C., Wilson, C., Walker, K. A., and Bernath, P. F.: Trends in atmospheric halogen containing gases since 2004, J. Quant. Spectrosc. Ra., 112, 2552–2566, doi:10.1016/j.jqsrt.2011.07.005, 2011.

[4] Ceausu-Velcescu, A., Bürger, H., and Graner, G.: High-resolution infrared spectra of HCF_3 in the ν_6 (500 cm^{-1}) and $2\nu_6$ (1000 cm^{-1}) regions: rovibrational analysis and accurate determination of the ground state constants C_0 and D_K^0, J. Mol. Spectrosc., 220, 298–305, 2003.

[5] Chang, L., Palo, S., Hagan, M, Richter, J., Garcia, R., Riggin, D., and Fritts, D.: Structure of the migrating diurnal tide in the Whole Atmosphere Community Climate Model (WACCM), Adv. Space Res., 41, 1398–1407, doi:10.1016/j.asr.2007.03.035, 2008.

[6] Chapman, S.: A theory of upper atmosphere ozone, Mem. R. Metrol. Soc., 3, 103–125, 1930.

[7] Chirkov, M., Stiller, G. P., Laeng, A., Kellmann, S., von Clarmann, T., Boone, C. D., Elkins, J. W., Engel, A., Glatthor, N., Grabowski, U., Harth, C. M., Kiefer, M., Kolonjari, F., Krummel, P. B., Linden, A., Lunder, C. R., Miller, B. R., Montzka,

S. A., Mühle, J., O'Doherty, S., Orphal, J., Prinn, R. G., Toon, G., Vollmer, M. K., Walker, K. A., Weiss, R. F., Wiegele, A., and Young, D.: Global HCFC-22 measurements with MIPAS: retrieval, validation, global distribution and its evolution over 2005 – 2012, Atmos. Chem. Phys., 16, 3345–3368, doi:10.5194/acp-16-3345-2016, 2016.

[8] Chubachi, S.: Preliminary results of ozone observations at Syowa Station from February 1982 to January 1983, in: Proc. Sixth Symposium on Polar Meteorology and Glaciology, edited by: Kusunoki, K., vol. 34 of Mem. National Institute of Polar Research Special Issue, 13–19, 1984.

[9] Chung, Y. K.: Absorption cross-sections off HFC-23 at atmospheric conditions, J. Quant. Spectrosc. Radiat. Transfer, 96, 281–287, doi:10.1016/j.jqsrt.2005.04.004, 2005.

[10] Coffey, M. T., Goldman, A., Hannigan, J. W., Mankin, W. G., Schoenfeld, W. G., Rinsland, C. P., Bernardo, C., and Griffith, D. W. T.: Improved vibration-rotation (0-1) HBr line parameters for validating high resolution infrared atmospheric spectra measurements, J. Quant. Spec. Rad. Trans., 60, 863–867, doi:10.1016/S0022-4073(98)00088-0, 1998.

[11] Connes, J. and Connes, P.: Near-Infrared Planetary Spectra by Fourier Spectroscopy. I. Instruments and Results, J. Opt. Soc. Am., 56, 896–910, 1966.

[12] Crutzen, P. J.: The influence of nitrogen oxides on the atmospheric ozone content, Q. J. Roy. Meteor. Soc., 96, 320–325, doi:10.1002/qj.49709640815, 1970.

[13] Crutzen, P. J.: Ozone production rates in oxygen-hydrogen-nitrogen oxide atmosphere. J. Geophys. Res., 76, 7311–7327, doi:10.1029/JC076i030p07311, 1971.

[14] De Mazière, M., Thompson, A. M., Kurylo, M. J., Wild, J. D., Bernhard, G., Blumenstock, T., Braathen, G. O., Hannigan, J. W., Lambert, J.-C., Leblanc, T., McGee, T. J., Nedoluha, G., Petropavlovskikh, I., Seckmeyer, G., Simon, P. C., Steinbrecht, W., and Strahan, S. E.: The Network for the Detection of Atmospheric Composition Change (NDACC): history, status and perspectives, Atmos. Chem. Phys., 18, 4935–4964, doi:10.5194/acp-18-4935-2018, 2018.

[15] Dobson, G. M. B.: Origin and distribution of polyatomic molecules in the atmosphere, Proc. R. Soc., A236, 187–193, 1956.

[16] Fang, X., Stohl, A., Yokouchi, Y., Kim, J., Li, S., Saito, T., Park, S., and Hu, J.: Multiannual top-down estimate of HFC-23 emissions in east Asia, Environ. Sci. Technol., 49, 4345–4353, doi:10.1021/es505669j, 2015.

[17] Fang, X., Ravishankara, A. R., Velders, G. J. M., Molina, M. J., Su, S., Zhang, J., Hu, J., and Prinn, R. G.: Changes in emissions of ozone-depleting substances from China due to implementation of the Montreal Protocol, Environ. Sci. Technol, 52, 11359–11366, doi:10.1021/acs.est.8b01280, 2018.

[18] Farman, J. C., Gardiner, B. G., and Shanklin, J. D.: Large losses of total ozone in Antarctica reveal seasonal ClOx/NOx interaction, Nature, 315, 207–210, doi:10.1038/315207a0, 1985.

[19] Fellgett, P.: Equivalent Quantum-Efficiencies of Photographic Emulsions, Monthly Notices of the Royal Astronomical Society, 118, 3, 224–233, doi:10.1093/mnras/118.3.224, 1958.

[20] Fernando, A. M., Bernath, P. F., and Boone, C. D.: Trends in atmospheric HFC-23 (CHF_3) and HFC-134a abundances, J. Quant. Spectrosc. Radiat. Transfer, 238, doi:10.1016/j.jqsrt.2019.06.019, 2019.

[21] Fleming, J. R.: Historical Perspectives on Climate Change, Oxford University Press, 1998.

[22] Gardiner, T., Forbes, A., de Mazière, M., Vigouroux, C., Mahieu, E., Demoulin, P., Velazco, V., Notholt, J., Blumenstock, T., Hase, F., Kramer, I., Sussmann, R., Stremme, W., Mellqvist, J., Strandberg, A., Ellingsen, K., and Gauss, M.: Trend analysis of greenhouse gases over Europe measured by a network of ground-based remote FTIR instruments, Atmos. Chem. Phys., 8, 6719–6727, doi:10.5194/acp-8-6719-2008, 2008.

[23] Gohar, L. K., Myhre, G., and Shine, K. P.: Updated radiative forcing estimates of four halocarbons, J. Geophys. Res., 109, D01107, doi:10.1029/2003JD004320, 2004.

[24] Goldman, A., Murcray, F. J., Blatherwick, R. D., Bonomo, F. S., Murcray, F. H., and Murcray, D. G.: Spectroscopic identification of $CHClF_2$ (F-22) in the lower stratosphere, Geophys. Res. Lett., 8, 1012–1014, doi:10.1029/GL008i009p01012, 1981.

[25] Gordon, I. E., Rothman, L. S., Hill, C., Kochanov, R. V., Tan, Y., Bernath, P. F., Birk, M., Boudon, V., Campargue, A., Chance, K. V., Drouin, B. J., Flaud, J. M., Gamache, R. R., Hodges, J. T., Jacquemart, D., Perevalov, V. I., Perrin, A., Shine, K. P., Smith, M. A. H., Tennyson, J., Toon, G. C., Tran, H., Tyuterev, V. G., Barbe, A., Császár, A. G., Devi, V. M., Furtenbacher, T., Harrison, J. J., Hartmann, J. M., Jolly, A., Johnson, T. J., Karman, T., Kleiner, I., Kyuberis, A. A., Loos, J., Lyulin, O. M., Massie, S. T., Mikhailenko, S. N., Moazzen-Ahmadi, N., Müller, H. S. P., Naumenko, O. V., Nikitin, A. V., Polyansky, O. L., Rey, M., Rotger, M., Sharpe, S. W., Sung, K., Starikova, E., Tashkun, S. A., Vander Auwera, J., Wagner, G., Wilzewski, J., Wcisło, P., Yu, S., Zak, E. J.: The HITRAN2016 Molecular Spectroscopic Database, J. Quant. Spectrosc. Radiat. Transf., 203, 3–69, 2017.

[26] Griffiths, P. R. and de Haseth, J. A. D.: Fourier Transform Infrared Spectroscopy, 2nd edn., John Wiley & Sons, New Jersey, 2007.

[27] Hansen, P. C.: Analysis of discrete ill-posed problems by means of the L-curve, SIAM Review, 34, 561–580, 1992.

[28] Harris, N. R. P., Wuebbles, D. J. (Lead Authors), Daniel, J. S., Hu, J., Kuijpers, L. J. M., Law, K. S., Prather, M. J., and Schofield, R.: Scenarios and information for policymakers, Chapter 5 in Scientific Assessment of Ozone Depletion: 2014, Global Ozone Research and Monitoring Project – Report No. 55, World Meteorological Organization, Geneva, Switzerland, 2014.

[29] Harrison, J. J., Boone, C. D., Brown, A. T., Allen, N. D. C., Toon, G. C., and Bernath, P. F.: First remote sensing observations of trifluoromethane (HFC-23) in the upper troposphere and lower stratosphere, J. Geophys. Res., 117, D05308, doi:10.1029/2011JD016423, 2012.

[30] Harrison, J. J.: Infrared absorption cross sections for trifluoromethane, J. Quant. Spectrosc. Radiat. Transfer, 130, 359–364, doi:10.1016/j.jqsrt.2013.05.026, 2013.

[31] Harrison, J. J., Chipperfield, M. P., Boone, C. D., Dhomse, S. S., Bernath, P. F., Froidevaux, L., Anderson, J., and Russell III, J.: Satellite observations of stratospheric hydrogen fluoride and comparisons with SLIMCAT calculations, Atmos. Chem. Phys., 16, 10501–10519, doi:10.5194/acp-16-10501-2016, 2016.

[32] Hase, F., Blumenstock, T. and Paton-Walsh, C.: Analysis of the instrumental line shape of high-resolution Fourier transform IR spectrometers with gas cell measurements and new retrieval software, Appl. Opt., 38, 3417–3422, doi:10.1364/AO.38.003417, 1999.

[33] Hase, F., Demoulin, P., Sauval, A. J., Toon, G. C., Bernath, P. F., Goldman, A., Hannigan, J. W., and Rinsland, C. P.: An empirical line-by-line model for the infrared solar transmittance spectrum from 700 to 5000 cm^{-1}, J. Quant. Spectros. Radiat. Transfer, 102, 450–463, 2006.

[34] Herzberg, G.: Molecular Spectra and Molecular Strucutre. I. Spectra of the Diatomic Molecule, D. Van Nostrand Company, Inc., New York, 1950.

[35] Hunt, B.G.: Photochemistry of ozone in a moist atmosphere, J. Geophys. Res., 71, 1385–1398, 1966.

[36] Jacob, D. J.: Introduction to atmospheric chemistry, Princeton University Press, 199–231, 1999.

[37] Jacquinot, P.: New developments in interference spectroscopy, Rep. Prog. Phys., 23, 267–312, 1960.

[38] Keeling, C. D., Bacastow, R. B., Bainbridge, A., Ekdahl Jr., C. A., Guenther, P. R., Waterman, L. S., and Chin, J. F.: Atmospheric carbon dioxide variations at Mauna Loa Observatory, Hawaii, Tellus, 28, 538–551, 1976.

[39] Kim, J., Li, S., Kim, K. R., Stohl, A., Mühle, J., Kim, S. K., Park, M. K., Kang, D. J., Lee, G., Harth, C. M., Salameh, P. K., and Weiss, R. F.: Regional atmospheric emissions determined from measurements at Jeju Island, South Korea: halogenated compounds from China, Geophys. Res. Lett, 37, L12801, doi:10.1029/2010GL043263, 2010.

[40] Koike, M., Jones, N. B., Palmer, P. I., Matsui, H., Zhao, Y., Kondo, Y., Matsumi, Y., and Tanimoto, H.: Seasonal variation of carbon monoxide in northern Japan: Fourier transform IR measurements and source-labeled model calculations, J. Geophys. Res., 111, D15306, doi:10.1029/2005JD006643, 2006.

[41] Kurylo, M. J. and Solomon, S.: Network for the Detection of Stratospheric Change: a status and implementation report, NASA Upper Atmosphere Research Program and NOAA Climate and Global Change Program (NASA), Washington DC, 1990.

[42] Langematz, U., Tully, M. B., Calvo, N., Dameris, M., de Laat, A. T. J., Klekociuk, A., Müller, R., and Young, P.: Update on Polar Stratospheric Ozone: Past, Present, and Future, in: Scientific Assessment of Ozone Depletion: 2018, World Meteorological Organization, Global Ozone Research and Monitoring Project – Report No. 58, chap. 4, World Meteorological Organization/UNEP, https://public.wmo.int/en/resources/library/scientific-assessment-of-ozone-depletion-2018, 2018.

[43] Le Treut, H., R. Somerville, U. Cubasch, Y. Ding, C. Mauritzen, A. Mokssit, T. Peterson and M. Prather: Historical Overview of Climate Change. In: Climate Change 2007: The Physical Science Basis. Contribution of Working Group I to the Fourth Assessment Report of the Intergovernmental Panel on Climate Change [Solomon, S., D. Qin, M. Manning, Z. Chen, M. Marquis, K.B. Averyt, M. Tignor and H.L. Miller (eds.)], Cambridge University Press, Cambridge, United Kingdom and New York, NY, USA, 2007.

[44] Li, S., Kim, J., Kim, K.-R., Mühle, J., Kim, S.-K., Park, M.-K., Stohl, A., Kang, D.-J., Arnold, T., Harth, C. M., Salameh, P. K., and Weiss, R. F.: Emissions of Halogenated Compounds in East Asia Determined from Measurements at Jeju Island, Korea, Environ. Sci. Technol, 45, 5668–5675, doi:10.1021/es104124k, 2011.

[45] Liou, K.: An Introduction to Atmospheric Radiation, International Geophysics Series, Academic Press, 2002.

[46] McCulloch, A. and Lindley, A. A.: Global emissions of HFC-23 estimated to year 2015, Atmos. Environ., 41, 1560–1566, doi:10.1016/j.atmosenv.2006.02.021, 2007.

[47] McDaniel, A. H., Cantrell, C. A., Davidson, J. A., Shetter, R. E., and Calvert, J. G.: The temperature dependent, infrared absorption cross-sections for the chlorofluorocarbons: CFC-11, CFC-12, CFC-13, CFC-14, CFC-22, CFC113, CFC-114, and CFC-115, J. Atmos. Chem., 12, 211–227, doi:10.1007/BF00048074, 1991.

[48] Meier, A., Toon, G. C., Rinsland, C. P., Goldman, A., and Hase, F.: Spectroscopic Atlas of Atmospheric Microwindows in the Middle Infrared, 2nd Edition, IRF Technical Report 048, ISSN 0284-1738, Kiruna, Sweden, 2004.

[49] Miller, B. R., Weiss, R. F., Salameh, P. K., Tanhua, T., Greally, B. R., Mühle, J., and Simmonds, P. G.: Medusa: A sample preconcentration and GC/MS detector system for in situ measurements of atmospheric trace halocarbons, hydrocarbons and sulfur compounds, Anal. Chem., 80, 1536–1545, doi:10.1021/ac/702084k, 2008.

[50] Miller, B. R., Rigby, M., Kuijpers, L. J. M., Krummel, P. B., Steele, L. P., Leist, M., Fraser, P. J., McCulloch, A., Harth, C., Salameh, P., Mühle, J., Weiss, R. F., Prinn, R. G., Wang, R. H. J., O' Doherty, S., Greally, B. R., and Simmonds, P. G.: HFC-23 (CHF_3) emission trend response to HCFC-22 ($CHClF_2$) production and recent HFC-23 emission abatement measures, Atmos. Chem. Phys., 10, 7875–7890, doi:10.5194/acp-10-7875-2010, 2010.

[51] Miller, B. R. and Kuijpers, L. J. M.: Projecting future HFC-23 emissions, Atmos. Chem. Phys., 11, 13259–13267, doi:10.5194/acp-11-13259-2011, 2011.

[52] Molina, M. J. and Rowland, F. S.: Stratospheric sink for chlorofluoromethanes: chlorine atom-catalysed destruction of ozone, Nature, 249, 810–812, 1974.

[53] Molina, M. J., Tso, T.-L., Molina, L. T., and Wang, F. C.-Y.: Antarctic Stratospheric Chemistry of Chlorine Nitrate, Hydrogen Chloride, and Ice: Release of Active Chlorine, Science, 238, 1253–1257, doi:10.1126/science.238.4831.1253, 1987.

[54] Montzka, S. A., Myers, R. C., Butler, J. H., Elkins, J. W., and Cummings, S. O.: Global tropospheric distribution and calibration scale of HCFC-22, Geophys. Res. Lett., 20, 703–706, 1993.

[55] Montzka, S. A., Hall, B. D. and Elkins, J. W.: Accelerated increases observed for Hydrochlorofluorocarbons since 2004 in the global atmosphere, Geophys. Res. Lett., 36, L03804, doi:10.1029/2008GL036475, 2009.

[56] Montzka, S. A., Velders, G. J. M. (Lead Authors), Krummel, P. B., Mühle, J., Orkin, V. L., Park, S., Shah, N., and Walter-Terrinoni, H.: Hydrofluorocarbons (HFCs), Chapter 2 in Scientific Assessment of Ozone Depletion: 2018, Global Ozone Research and Monitoring Project – Report No. 58, World Meteorological Organization, Geneva, Switzerland, 2018.

[57] Moore, D. P. and Remedios, J. J.: Growth rates of stratospheric HCFC-22, Atmos. Chem. Phys., 8, 73–82, doi:10.5194/acp-8-73-2008, 2008.

[58] Morse, P. M.: Diatomic Molecules According to the Wave Mechanics. II. Vibrational Levels, Phys. Rev., 34, 57–64, 1929.

[59] Nagahama, Y., and Suzuki, K.: The influence of forest fires on CO, HCN, C_2H_6, and C_2H_2 over northern Japan measured by infrared solar spectroscopy, Atmos. Env., 41, 9570–9579, 2007.

[60] Naik, V., Jain, A. K., Patten, K. O. and Wuebbles, D. J.: Consistent sets of atmospheric lifetimes and radiative forcings on climate for CFC replacements: HCFCs and HFCs, J. Geophys. Res., 105, 6903–6914, 2000.

[61] Nakajima, H., Liu, X., Murata, I., Kondo, Y., Murcray, F. J., Koike, M., Zhao, Y., and Nakane, H.: Retrieval of vertical profiles of ozone from high-resolution infrared solar spectra at Rikubetsu, Japan, J. Geophys. Res., 102, 29981–29990, 1997.

[62] Nakajima, H., Murata, I., Nagahama, Y., Akiyoshi, H., Saeki, K., Kinase, T., Takeda, M., Tomikawa, Y., Dupuy, E., and Jones, N. B.: Chlorine partitioning near the polar vortex edge observed with ground-based FTIR and satellites at Syowa Station, Antarctica, in 2007 and 2011, Atmos. Chem. Phys., 20, 1043–1074, doi:10.5194/acp-20-1043-2020, 2020.

[63] Nassar, R., Bernath, P. F., Boone, C. D., McLeod, S. D., Skelton, R., Walker, K. A., Rinsland, C. P., and Duchatelet, P.: A global inventory of stratospheric fluorine in 2004 based on Atmospheric Chemistry Experiment Fourier trans-

form spectrometer (ACE-FTS) measurements, J. Geophys. Res., 111, D22313, doi:10.1029/2006JD007395, 2006.

[64] O'Doherty, S., Cunnold, D. M., Manning, A., Miller, B. R., Wang, R. H. J., Krummel, P. B., Fraser, P. J., Simmonds, P. G., McCulloch, A., Weiss, R. F., Salameh, P., Porter, L. W., Prinn, R. G., Huang, J., Sturrock, G., Ryall, D., Derwent, R. G., and Montzka, S. A.: Rapid growth of hydrofluorocarbon 134a and hydrochlorofluorocarbons 141b, 142b, and 22 from Advanced Global Atmospheric Gases Experiment (AGAGE) observations at Cape Grim, Tasmania, and Mace Head, Ireland, J. Geophys. Res., 109, D06310, doi:10.1029/2003JD004277, 2004.

[65] Oram, D. E., Sturges, W. T., Penkett, S. A., McCulloch, A., and Fraser, P. J.: Growth of fluoroform (CHF_3, HFC-23) in the background atmosphere, Geophys. Res. Lett., 25, 35–38, 1998.

[66] Ortega, I., Buchholz, R. R., Hall, E. G., Hurst, D. F., Jordan, A. F., and Hannigan, J. W.: Tropospheric water vapor profiles obtained with FTIR: comparison with balloon-borne frost point hygrometers and influence on trace gas retrievals, Atmos. Meas. Tech., 12, 873–890, doi:10.5194/amt-12-873-2019, 2019.

[67] Palmer, P. I., Jacob, D. J., Mickley, L. J., Blake, D. R., Sachse, G. W., Fuelberg, H. E., and Kiley, C. M.: Eastern Asian emissions of anthropogenic halocarbons deduced from aircraft concentration data, J. Geophys. Res.-Atmos., 108, 4753, doi:10.1029/2003JD003591, 2003.

[68] Pougatchev, N. S., Connor, B. J., and Rinsland, C. P.: Infrared measurements of the ozone vertical distribution above Kitt Peak, J. Geophys. Res., 100, 16689–16697, doi:10.1029/95JD01296, 1995.

[69] Prinn, R. G., Weiss, R. F., Fraser, P. J., Simmonds, P. G., Cunnold, D. M., Alyea, F. N., O'Doherty, S., Salameh, P., Miller, B. R., Huang, J., Wang, R. H. J., Hartley, D. E., Harth, C., Steele, L. P., Sturrock, G., Midgley, P. M., and McCulloch, A.: A history of chemically and radiatively important gases in air deduced from ALE/GAGE/AGAGE, J. Geophys. Res., 105, 17751–17792, 2000.

[70] Ramanathan V.: Greenhouse Effect Due to Chlorofluorocarbons: Climatic Implications, Science, 190, 50–52, 1975.

[71] Rasmussen, R. A., Khalil, M. A. K., Penkett, S. A. and Prosser, N. J. D.: $CHClF_2$ (F-22) in the Earth's atmosphere, Geophys. Res. Lett., 7, 809–812, 1980.

[72] Rees, D., Barnett, J. J., and Labitzke, K.: COSPAR International Reference Atmosphere: 1986, Part II, Middle Atmosphere Models, Adv. Space Res., 10, 1–525, 1990.

[73] Rinsland, C. P., Johnson, D. W., Goldman, A., and Levine, J. S.: Evidence for a decline in the atmospheric accumulation rate of $CHCIF_2$ (CFC-22). Nature 337, 535–537, doi:10.1038/337535a0, 1989.

[74] Rinsland, C. P., Boone, C., Nassar, R., Walker, K., Bernath, P., Mahieu, E., Zander, R., McConnell, J. C., and Chiou, L.: Trends of HF, HCl, CCl_2F_2, CCl_3F, $CHClF_2$ (HCFC-22), and SF_6 in the lower stratosphere from Atmospheric Chemistry Experiment (ACE) and Atmospheric Trace Molecule Spectroscopy (ATMOS) measurements near 30°N latitude, Geophys. Res. Lett., 32, L16S03, doi:10.1029/2005GL022415, 2005.

[75] Rodgers, C. D.: Retrieval of atmospheric temperature and composition from remote measurements of thermal radiation, Rev. Geophys., 14, 609–624, 1976.

[76] Rodgers, C. D.: Characterization and error analysis of profiles retrieved from remote sounding measurements, J. Geophys. Res., 95, 5587–5595, 1990.

[77] Rodgers, C. D.: Inverse methods for atmospheric sounding: Theory and practice, World Scientific, 238 pp., ISBN 981-02-2740-X, 2000.

[78] Rothman, L. S. Gordon, I. E., Barbe, A., Chris Benner, D., Bernath, P. F., Birk, M., Boudon, V., Brown, L. R., Campargue, A, Champion, J. -P., Chance, K., Coudert, L. H., Dana, V., Devi, V. M., Fally, S., Flaud, J. -M., Gamache, R. R., Goldman, A., Jacquemart, D., Kleiner, I., Lacome, N., Lafferty, W. J., Mandin, J. -Y., Massie, S. T., Mikhailenko, S. N., Miller, C. E., Moazzen-Ahmadi, N., Naumenko, O. V., Nikitin, A. V., Orphal, J., Perevalov, V. I., Perrin, A., Predoi-Cross, A., Rinsland, C. P., Rotger, M., Šimečtová, M., Smith, M. A. H., Sung, K., Tashkun, S. A., Tennyson, J., Toth, R. A., Vandaele, A. C., and Vander Auwera, J.: The HITRAN 2008 molecular spectroscopic database, J. Quant. Spectrosc. Radiat. Transfer, 110, 533–572, doi:10.1016/j.jqsrt.2009.02.013, 2009.

[79] Salawitch, R.J., Fahey, D.W., Hegglin, M.I., McBride, L.A.,Tribbet,W.R., and Doherty, S.J.: Twenty questions and answers about the ozone layer: 2018 Update, Scientific Assessment of Ozone Depletion: 2018, World Meteorological Organization, 2019.

[80] Sharpe, S. W., Johnson, T. J., Sams, R. L., Chu, P. M., Rhoderick, G. C., and Johnson, P. A.: Gas-phase databases for quantitative infrared spectroscopy, Appl. Spectrosc., 58, 1452–1461, doi:10.1366/0003702042641281, 2004.

[81] Sherlock, V. J., Jones, N. B., Matthews, W. A., Murcray, F. J., Blatherwick, R. D., Murcray, D. G., Goldman, A., Rinsland, C. P., Bernardo, C., and Griffith, D. W. T.: Increase in the vertical column abundance of HCFC-22 ($CHClF_2$) above Lauder, New Zealand, between 1985 and 1994, J. Geophys. Res. Atmos., 102, 8861–8865, doi:10.1029/96JD01012, 1997.

[82] Simmonds, P. G., O'Doherty, S., Nickless, G., Sturrock, G. A., Swaby, R., Knight, P., Ricketts, J., Woffendin, G., and Smith, R.: Automated gas chromatograph/mass spectrometer for routine atmospheric field measurements of the CFC replacement compounds, the hydrofluorocarbons and hydrochlorofluorocarbons, Anal. Chem., 67, 717–723, 1995.

[83] Simmonds, P. G., Rigby, M., McCulloch, A., Vollmer, M. K., Henne, S., Mühle, J., O'Doherty, S., Manning, A. J., Krummel, P. B., Fraser, P. J., Young, D., Weiss, R. F., Salameh, P. K., Harth, C. M., Reimann, S., Trudinger, C. M., Steele, L. P., Wang, R. H. J., Ivy, D. J., Prinn, R. G., Mitrevski, B., and Etheridge, D. M.: Recent increases in the atmospheric growth rate and emissions of HFC-23 (CHF_3) and the link to HCFC-22 ($CHClF_2$) production, Atmos. Chem. Phys., 18, 4153–4169, doi:10.5194/acp-18-4153-2018, 2018a.

[84] Simmonds, P. G., Rigby, M., McCulloch, A., Vollmer, M. K., Henne, S., Mühle, J., O'Doherty, S., Manning, A. J., Krummel, P. B., Fraser, P. J., Young, D., Weiss, R. F., Salameh, P. K., Harth, C. M., Reimann, S., Trudinger, C. M., Steele, L. P., Wang, R. H. J., Ivy, D. J., Prinn, R. G., Mitrevski, B., and Etheridge, D. M.: Supplement of Recent increases in the atmospheric growth rate and emissions of HFC-23 (CHF_3)

and the link to HCFC-22 ($CHClF_2$) production, Supplement of Atmos. Chem. Phys., 18, 4153–4169, doi:10.5194/acp-18-4153-2018-supplement, 2018b.

[85] Solomon, S.: Stratospheric ozone depletion: A review of concepts and history, Rev. Geophys., 37, 275–316, doi:10.1029/1999RG900008, 1999.

[86] Solomon, S., Garcia, R. R., Rowland, F. S., and Wuebbles, D. J.: On the depletion of Antarctic ozone, Nature, 321, 755–758, 1986.

[87] Solomon, S., Ivy, D. J., Kinnison, D., Mills, M. J., Neely, R. R., and Schmidt, A.: Emergence of healing in the Antarctic ozone layer, Science, 353, 269–274, doi:10.1126/science.aae0061, 2016.

[88] Stanley, K. M., Say, D., Mühle, J., Harth, C. M., Krummel, P. B., Young, D., O'Doherty, S. J., Salameh, P. K., Simmonds, P. G., Weiss, R. F., Prinn, R. G., Fraser, P. J., and Rigby, M.: Increase in global emissions of HFC-23 despite near-total expected reductions, Nat. Commun., 11, 397, doi:10.1038/s41467-019-13899-4, 2020.

[89] Steck, T.: Methods for determining regularization for atmospheric retrieval problems, Appl. Optics, 41, 1788–1797, 2002.

[90] Stolarski, R. S., Krueger, A. J., Schoeberl, M. R., McPeters, R. D., Newman, P. A., and Alpert, J. C.: Nimbus-7 Satellite Measurements of the Springtime Antarctic Ozone Decrease, Nature, 322, 808–811, 1986.

[91] Sussmann, R., Borsdorff, T., Rettinger, M., Camy-Peyret, C., Demoulin, P., Duchatelet, P., Mahieu, E., and Servais, C.: Technical Note: Harmonized retrieval of column-integrated atmospheric water vapor from the FTIR network – first examples for long-term records and station trends, Atmos. Chem. Phys., 9, 8987–8999, doi:10.5194/acp-9-8987-2009, 2009.

[92] Tikhonov, A.: On the solution of incorrectly stated problems and a method of regularization, Dokl. Acad. Nauk SSSR, 151, 501–504, 1963.

[93] Tyndall, J.: The Bakerian lecture: On the absorption and radiation of heat by gases and vapours, and on the physical connexion of radiation, absorption, and conduction, Philos. Trans. R. Soc. London, Ser. I 151, 1–36, 1861.

[94] UNEP: Montreal Protocol on substances that deplete the ozone layer, United Nations Environment Programme: UNEP, 2000.

[95] UNEP: Adjustments agreed by the Nineteenth Meeting of the Parties relating to the controlled substances in group I of Annex C of the Montreal Protocol (hydrochlorofluorocarbons), in Report of the Nineteenth Meeting of the Parties to the Montreal Protocol on Substances that Deplete the Ozone Layer, UNEP/OzL.Pro.19/7, United Nations Environment Program Ozone Secretariat, Nairobi, Kenya, 2007. UNEP: The Path from Kigali: HFC Phase-Down Timeline, https://wedocs.unep.org/20.500.11822/26592, 2018.

[96] Varanasi, P., Li, Z., Nemtchinov, V., and Cherukuri, A.: Spectral absorption-coefficient data on HCFC-22 and SF_6 for remotesensing applications, J. Quant. Spectrosc. Ra., 52, 323–332, doi:10.1016/0022-4073(94)90162-7, 1994.

[97] Vigouroux, C., Hendrick, F., Stavrakou, T., Dils, B., De Smedt, I., Hermans, C., Merlaud, A., Scolas, F., Senten, C., Vanhaelewyn, G., Fally, S., Carleer, M., Metzger, J.-M., Müller, J.-F., Van Roozendael, M., and De Mazière, M.: Ground-based FTIR and MAX-DOAS observations of formaldehyde at Réunion Island and comparisons with satellite and model data, Atmos. Chem. Phys., 9, 9523–9544, doi:10.5194/acp-9-9523-2009, 2009.

[98] Vigouroux, C., Stavrakou, T., Whaley, C., Dils, B., Duflot, V., Hermans, C., Kumps, N., Metzger, J.-M., Scolas, F., Vanhaelewyn, G., Müller, J.-F., Jones, D. B. A., Li, Q., and De Mazière, M.: FTIR time-series of biomass burning products (HCN, C_2H_6, C_2H_2, CH_3OH, and HCOOH) at Reunion Island (21°S, 55°E) and comparisons with model data, Atmos. Chem. Phys., 12, 10367–10385, https://doi.org/10.5194/acp-12-10367-2012, 2012.

[99] Vömel, H., David, D. E., and Smith, K.: Accuracy of tropospheric and stratospheric water vapor measurements by the cryogenic frost point hygrometer: Instrumental details and observations, J. Geophys. Res., 112, 8305, doi:10.1029/2006JD007224, 2007.

[100] Wallace, J. M. and Hobbs, P. V.: Atmospheric Science: An Introductory Survey, 2nd edition, Academic Press, 2006.

[101] Wang, W. C., Yung, Y. L., Lacis, A. A., Mo, T., and Hansen, J. E.: Greenhouse effect due to manmade perturbations of trace gases, Science, 194, 685–690, 1976.

[102] Weart, S. R.: The Discovery of Global Warming: Revised and Expanded Edition, Harvard University Press, 2008.

[103] Xiang, B., Patra, P. K., Montzka, S. A., Miller, S. M., Elkins, J. W., Moore, F. L., Atlas, E. L., Miller, B. R., Weiss, R. F., Prinn, R. G., and Wofsy, S. C.: Global emissions of refrigerants HCFC-22 and HFC-134a: Unforeseen seasonal contributions, P. Natl. Acad. Sci. USA, 111, 17379–17384, doi:10.1073/pnas.1417372111, 2014.

[104] Yokouchi, Y., Taguchi, S., Saito, T., Tohjima, Y., Tanimoto, H., and Mukai, H.: High frequency measurements of HFCs at a remote site in east Asia and their implications for Chinese emissions, Geophys. Res. Lett., 33, L21814, doi:10.1029/2006GL026403, 2006.

[105] Zander, R., Rinsland, C. P., Farmer, C. B., and Norton, R. H.: Infrared spectroscopic measurements of halogenated source gases in the stratosphere with the ATMOS instrument, J. Geophys. Res., 92, 9836–9850, 1987.

[106] Zander, R., Mahieu, E., Demoulin, P., Rinsland, C. P., Weisenstein,D. K., Ko, M. K. W., Sze, N. D., and Gunson, M. R.: Secular evolution of the vertical column abundances of $CHClF_2$ (HCFC-22) in the Earth's atmosphere inferred from ground-based IR solar observations at the Jungfraujoch and at Kitt Peak, and comparison with model calculations, J. Atmos. Chem., 18, 129–148, doi:10.1007/BF00696811, 1994.

[107] Zander, R., Mahieu, E., Demoulin, P., Duchatelet, P., Servais, C., Roland, G., DelBouille, L., Mazière, M. D., and Rinsland, C. P.: Evolution of a dozen non-CO_2 greenhouse gases above central Europe since the mid-1980s, Environ. Sci., 2, 295–303, doi:10.1080/15693430500397152, 2005.

[108] Zeng, J., Tohjima, Y., Fujinuma, Y., Mukai, H., and Katsumoto, M.: A study of trajectory quality using methane measurements from Hateruma Island, Atmos. Environ., 37, 1911–1919, 2003.

[109] Zhao, Y., Kondo, Y., Murcray, F. J., Liu, X., Koike, M., Kita, K., Nakajima, H., Murata, I., and Suzuki, K.: Carbon monoxide column abundances and tropospheric concentrations retrieved from high resolution ground-based infrared solar spectra at 43.5°N over Japan, J. Geophys. Res., 102, 23403–23411, 1997.

[110] Zhao, Y., Strong, K., Kondo, Y., Koike, M., Matsumi, Y., Irie, H., Rinsland, C. P., Jones, N. B., Suzuki, K., Nakajima, H., Nakane, H., and Murata, I.: Spectroscopic measurements of tropospheric CO, C_2H_6, C_2H_2, and HCN in northern Japan, J. Geophys. Res., 107, 4343, doi:10.1029/2001JD000748, 2002.

[111] Zhou, M., Vigouroux, C., Langerock, B., Wang, P., Dutton, G., Hermans, C., Kumps, N., Metzger, J.-M., Toon, G., and De Mazière, M.: CFC-11, CFC-12 and HCFC-22 ground-based remote sensing FTIR measurements at Réunion Island and comparisons with MIPAS/ENVISAT data, Atmos. Meas. Tech., 9, 5621–5636, doi:10.5194/amt-9-5621-2016, 2016.